

INVESTIGATION OF FLOWFIELD CHARACTERISTICS DUE TO SHOCK
WAVE-BOUNDARY LAYER INTERACTION ON COMPRESSION
DECOMPRESSION CORNERS USING LES

A THESIS SUBMITTED TO
THE GRADUATE SCHOOL OF NATURAL AND APPLIED SCIENCES
OF
MIDDLE EAST TECHNICAL UNIVERSITY

BY

IRMAK TAYLAN KARPUZCU

IN PARTIAL FULFILLMENT OF THE REQUIREMENTS
FOR
THE DEGREE OF MASTER OF SCIENCE
IN
MECHANICAL ENGINEERING

JULY 2019

Approval of the thesis:

**INVESTIGATION OF FLOWFIELD CHARACTERISTICS DUE TO SHOCK
WAVE-BOUNDARY LAYER INTERACTION ON COMPRESSION
DECOMPRESSION CORNERS USING LES**

submitted by **IRMAK TAYLAN KARPUZCU** in partial fulfillment of the requirements for the degree of **Master of Science in Mechanical Engineering Department, Middle East Technical University** by,

Prof. Dr. Halil Kalıpçılar
Dean, Graduate School of **Natural and Applied Sciences**

Prof. Dr. Sahir Arıkan
Head of Department, **Mechanical Engineering**

Assoc. Prof. Dr. Cüneyt Sert
Supervisor, **Mechanical Engineering, METU**

Examining Committee Members:

Prof. Dr. Hakan Tarman
Mechanical Engineering, METU

Assoc. Prof. Dr. Cüneyt Sert
Mechanical Engineering, METU

Assoc. Prof. Dr. M. Metin Yavuz
Mechanical Engineering, METU

Dr. Ö. Uğraş Baran
Mechanical Engineering, METU

Dr. Sıtkı Uslu
Mechanical Engineering, TOBB ETÜ

Date: 18.07.2019

I hereby declare that all information in this document has been obtained and presented in accordance with academic rules and ethical conduct. I also declare that, as required by these rules and conduct, I have fully cited and referenced all material and results that are not original to this work.

Name, Surname: Irmak Taylan Karpuzcu

Signature:

ABSTRACT

INVESTIGATION OF FLOWFIELD CHARACTERISTICS DUE TO SHOCK WAVE-BOUNDARY LAYER INTERACTION ON COMPRESSION DECOMPRESSION CORNERS USING LES

Karpuzcu, Irmak Taylan
Master of Science, Mechanical Engineering
Supervisor: Assoc. Prof. Dr. Cüneyt Sert

July 2019, 104 pages

Shock wave boundary layer interactions occur in industrial flows where the flow is transonic, supersonic or hypersonic and there is an incoming boundary layer present. Many of the air crafts such as planes, rockets, missiles, re-entry vehicles, and supersonic wind tunnels experience shock wave boundary layer interactions. These interactions can take place on an air craft at several different places such as the air intakes, ramps, forebody and fins, and also the diffuser section of a supersonic wind tunnel. In this thesis study, three cases of shock wave boundary layer interactions are investigated, which are compression-expansion ramp, shock impinging on a wall and shock impinging on a compression-expansion ramp. The first case is at Mach 2.88 and with a Reynolds number of 135000 based on the incoming boundary layer thickness, while others are at Mach 2.05 and a Reynolds number of 188000 based on the incoming boundary layer thickness. OpenFOAM is used as the CFD software and solutions are performed using wall modeled large eddy simulations using wall functions. For the first two cases, the results are compared with the available experimental and numerical data. The results of the third case are novel since it has not yet been studied in the literature numerically or experimentally. The results for the first two cases were comparable to experimental results in terms of pressure

distribution, flow field structures and unsteadiness whereas velocity profiles and skin friction distributions showed discrepancies especially in the separation zones.

Keywords: Shock Wave Boundary Layer Interaction (SWBLI), Supersonic flows, Wall modeled Large Eddy Simulation (LES), Wall functions

ÖZ

SIKIŞTIRMA – GENİŞLETME RAMPALARINDA OLUŞAN ŞOK DALGASI SINIR TABAKA ETKİLEŞİMLERİNİN BÜYÜK GİRDAP BENZETİMLERİ İLE İNCELENMESİ

Karpuzcu, Irmak Taylan
Yüksek Lisans, Makina Mühendisliği
Tez Danışmanı: Doç. Dr. Cüneyt Sert

Temmuz 2019, 104 sayfa

Şok dalgası sınır tabaka etkileşimleri bir şok dalgasının gelen sınır tabaka üzerine çarpmasıyla oluşan etkileşimlerdir. Bu etkileşimler uçaklar, roketler ve uzay mekikleri gibi sesüstü hızlarda hareket eden hava taşıtlarının performanslarını önemli bir ölçüde etkilemektedir. Bu etkileşimler bahsi geçen araçların hava alıkları, kanatları ve burunları gibi çeşitli parçalarında gözlemlenebilmektedir. Bu çalışmada üç farklı konfigürasyonda şok dalgası sınır tabaka etkileşimleri incelenmiştir. Bu geometriler sıkıştırma – genişletme rampası, duvara çarpan şok dalgası ve sıkıştırma – genişletme rampasına çarpan şok dalgasıdır. İlk konfigürasyonda Mach sayısı 2.88 ve sınır tabaka kalınlığına bağlı Reynolds sayısı 135000 iken diğer konfigürasyonlarda Mach sayısı 2.05 ve sınır tabaka kalınlığına bağlı Reynolds sayısı 188000'dir. Hesaplamalı akışkanlar dinamiği programı olarak OpenFOAM kullanılmış ve akışlar duvar fonksiyonları kullanarak duvara yakın bölgenin modellendiği büyük girdap benzetimi yöntemiyle çözülmüştür. İlk iki konfigürasyon için sonuçlar literatürde mevcut olan deneysel ve nümerik sonuçlar ile karşılaştırılmıştır. Üçüncü konfigürasyon henüz literatürde deneysel veya nümerik olarak çalışılmamıştır. İlk iki konfigürasyon için basınç dağılımları, akış içindeki şok yapıları ve akış kararsızlığının önceki sonuçlar ile

uyumlu olduđu görülürken, sürüklenme kuvveti ve hız profillerinde özellikle ayrılma bölgelerinde farklılıklar gözlenmiştir.

Anahtar Kelimeler: Şok dalgası sınır tabaka etkileşimleri, Sesüstü akışlar, Duvar Modellemeli Büyük Girdap Benzetimi, Duvar Fonksiyonları

To my family...

ACKNOWLEDGEMENTS

Firstly, I want to thank my advisor Assoc. Prof. Dr. Cüneyt Sert for his guidance, patience and continuous support throughout this thesis work. I want to thank Dr. Kamil Özden who provided help for the use of OpenFOAM on a remote cluster. I also would like to thank my coworkers Berk Bozkır, Muhiddin T. Akpolat and Ezgi Arısoy for their moral support and encouragement. My sincere gratitude goes to my roommates Mesut Balcı and Barış Çavuş for their guidance on the coding work where necessary and their continuous efforts for motivating me to finish this M.Sc. study.

Special thanks to TÜBİTAK ULAKBİM High Performance and Grid Computing Center and their technical support team for making it possible to use TRUBA HPC system efficiently in this thesis study

I would also like to acknowledge and thank Middle East Technical University for the financial support under GAP-302-2018-2706 scientific research project during this study.

Lastly, I want to thank my parents and my brother for their continuous love and support. Without them it would be hard to carry out this study.

TABLE OF CONTENTS

ABSTRACT.....	v
ÖZ.....	vii
ACKNOWLEDGEMENTS.....	x
TABLE OF CONTENTS.....	xi
LIST OF TABLES.....	xiii
LIST OF FIGURES.....	xiv
CHAPTER 1.....	1
1. INTRODUCTION.....	1
1.1. Flow Physics of Shock wave Boundary Layer Interactions.....	4
1.1.1. Flow Unsteadiness.....	5
1.1.2. Heat transfer.....	7
1.1.3. Incoming Boundary Layer.....	8
1.1.4. Flow Control.....	9
1.1.5. Three-Dimensional (3D) Effects.....	10
1.2. SWBLI Modelling with Large Eddy Simulation (LES).....	10
1.3. Current Work.....	16
CHAPTER 2.....	19
2. LITERATURE REVIEW.....	19
2.1. Literature Review of the SWBLI for the Geometries to be Investigated.....	26
2.2. Literature Review on Wall Modeled LES (WMLES).....	34
2.3. Literature Review on the use of OpenFOAM for Supersonic Flows and Compressible LES/DES simulations.....	36

CHAPTER 3	39
3. SIMULATIONS OF CASE I: THE COMPRESSION-EXPANSION RAMP ..	39
3.1. Computational Model	41
3.2. Results and Discussion.....	47
CHAPTER 4	59
4. SIMULATIONS OF CASE II: SHOCK IMPINGING ON A WALL.....	59
4.1. Computational Model	61
4.2. Results and Discussion.....	63
CHAPTER 5	77
5. SIMULATIONS ON CASE III: SHOCK IMPINGING ON A COMPRESSION- EXPANSION RAMP	77
5.1. Computational Model	79
5.2. Results and Discussion.....	79
CHAPTER 6	89
6. CONCLUSIONS	89
REFERENCES	95

LIST OF TABLES

TABLES

Table 2.1. Summary of the SWBLI Literature.....	20
Table 2.2. Measurement locations of Zheltovodov (taken from Grilli et al.[8]). All locations are given in x/δ_0	27
Table 3.1. Reference values for the compression decompression ramp [49].....	40
Table 3.2. Additional data points, in x/δ_0	41
Table 3.3. Mesh details	43
Table 4.1. Reference values for Case II [9]	60
Table 4.2. Locations of stations where data were taken.	61
Table 4.3. Mesh details for case II (before adaptation).....	63
Table 5.2. Locations of stations where data are gathered for Case III.....	79

LIST OF FIGURES

FIGURES

Figure 1.1. Schematic of SWBLI on a compression ramp [5].....	2
Figure 1.2. Schematic of a shock impinging on a wall [5].....	2
Figure 1.3. Schematic of a corner flow [6].....	3
Figure 1.4. Schematic of flow at an expansion corner [7].....	3
Figure 1.5. Structure of SWBLI on a compression-expansion ramp [8].....	4
Figure 1.6. . Structure of SWBLI for an impinging shock on a wall (IS – Impinging Shock, RS – Reflected Shock, MS – Mach Stem, SS – Separation Shock, TS – Transmitted Shock) [9].....	5
Figure 1.7. Locations of pressure measurements (taken from ref. [5])	6
Figure 1.8. Power spectral densities of pressure signals for flow over a compression ramp (taken from ref. [5][11] (1) undisturbed boundary layer, (2,3) shock foot, (4,5) downstream shock foot.....	7
Figure 1.9. Comparison of studies calculating heat transfer rate [3].....	8
Figure 1.10. Flow control using micro-jets [13].....	9
Figure 1.11. Typical near wall mesh resolutions for RANS (a) and LES (b).....	12
Figure 1.12. Computational costs for inner and outer layers of a flat plate simulation [18].....	14
Figure 1.13. Compression-expansion ramp geometry.....	16
Figure 1.14. Shock impinging on a wall geometry.....	17
Figure 1.15. Shock impinging on a compression-expansion ramp geometry.....	18
Figure 2.1. Measurement locations from experimental work of Zheltovodov (taken from Grilli et al.[8])	27
Figure 2.2. Schlieren image from the work of Zheltovodov [49].....	28
Figure 2.3. Geometry of Campo and Eaton [9]	28

Figure 2.4. PIV work of Campo and Eaton showing the contours of the streamwise velocity component [9]	29
Figure 2.5. Geometry and grid (not every line was shown) for the DNS simulation of Adams [34].....	30
Figure 2.6. Computational domain of Loginov et al. (not every grid line was shown) [48]	31
Figure 2.7. Grid used in the DNS work of Tong et al. [75]	32
Figure 2.8. a) LES simulations of Grilli et al. [8] b) Experiments of Zheltovodov [49]	33
Figure 2.9. Grid used in the WMLES study of Marco [83]	36
Figure 2.10. Numerical Schlieren images from the study of Makowka et al. [87].....	37
Figure 3.1. Problem geometry and boundary conditions for Case I: Compression-expansion ramp	39
Figure 3.2. Time history of wall pressure at station E2	43
Figure 3.3. Close-up view of the Medium mesh around the ramp.....	44
Figure 3.4. Wall pressure distributions obtained with four different grids.....	45
Figure 3.5. Velocity profiles obtained with four different grids at four stations.	46
Figure 3.6. Zoomed-in view of the Medium grid after the AMR process	47
Figure 3.7. y^+ contours obtained with the Medium with AMR grid	48
Figure 3.8. LES IQ and M index contours.....	49
Figure 3.9. Pressure distribution along the wall (averaged in time and spanwise direction)	50
Figure 3.10. Velocity profiles at the different locations (averaged in time and in spanwise direction)	51
Figure 3.11. The spanwise averaged instantaneous Mach contours (S – separation, R - reattachment)	52
Figure 3.12. The spanwise averaged instantaneous Mach number distribution along the $y/\delta_0=5$ horizontal plane	53
Figure 3.13. Schlieren photograph of Zheltovodov [49] (a) and numerical Schlieren (b) of the current simulation.....	54

Figure 3.14. Contours of instantaneous wall shear stress in the x direction.....	55
Figure 3.15. Instantaneous contours of streamwise vorticity (a) and wall shear stress in the z direction (b).....	56
Figure 3.16. Average skin friction coefficient along the wall	57
Figure 3.17. Pressure signals and their FFTs for stations E1 (top) and E2 (bottom)	58
Figure 4.1. Problem geometry and boundary conditions for Case II: Shock impinging on a wall.....	59
Figure 4.2. Velocity profile specified at the inlet boundary of Case II	62
Figure 4.3. Zoomed in view of the grid after the AMR process for Case II.....	63
Figure 4.4. Instantaneous contours of the Mach number taken from the mid-plane for Case II.....	64
Figure 4.5. Instantaneous Mach number distribution at the mid-plane along lines $y/\delta_0=1.5$ (red), and $y/\delta_0=7.5$ (blue)	65
Figure 4.6. The two zones of Campo and Eaton's [9] PIV measurements that will be used for comparison with the current study. This figure shows a plane near the mid-plane in the spanwise direction.....	66
Figure 4.7. Comparison of the streamwise velocity contours near the ramp on the mid-plane of the domain (above Campo and Eaton [9] and below the current study)	67
Figure 4.8. Comparison of the flow fields for the impinging shock for mean streamwise velocity at the mid-plane (above Campo and Eaton [9] and below current study)	68
Figure 4.9. Comparison of time-averaged y velocity contours near the upper wall at the mid-plane (above Campo and Eaton [9] and below the current study)	69
Figure 4.10. Comparison of time-averaged y velocity contours near the lower wall at the mid-plane (above Campo and Eaton [9] and below the current study)	70
Figure 4.11. Streamwise turbulence intensity contours for both upper and lower walls at the middle plane. (Above the experiment [9], below current simulation).....	71
Figure 4.12. Pressure distributions on the upper and lower walls of Case II	72
Figure 4.13. Mean skin friction coefficient distribution for upper and lower walls of Case II.....	73

Figure 4.14. Wall shear stress contours in the x direction for Case II (S-Separation line, R-Reattachment line, SS-Separation shock)	74
Figure 4.15. Vorticity contours in x direction for the lower wall. (SS – Separation Shock)	75
Figure 4.16. Time history of the pressure data and corresponding FFT’s for station L1 (above) and L10 (below) of Case II	76
Figure 5.1. Problem geometry and boundary conditions for Case III: Impinging shock on a compression-expansion ramp	78
Figure 5.2. Mesh after the AMR process for Case III.....	80
Figure 5.3. Instantaneous contours of the Mach number at the mid-plane of Case III	81
Figure 5.4. Instantaneous Mach number distribution at the mid-plane along $y/\delta_0=2$ (red), and $y/\delta_0=5.5$ (blue) lines.....	82
Figure 5.5. Mean pressure distributions for lower and upper walls of Case III.....	83
Figure 5.6. Mean skin friction coefficient distribution on the walls of Case III.....	84
Figure 5.7. Streamwise wall shear stress contours on the upper and lower walls. (S – separation, R – reattachment, SS – Separation shock).....	85
Figure 5.8. Spanwise wall shear stress contours on the lower wall of Case III. (SS – Separation Shock, S – Separation, R – Reattachment)	85
Figure 5.9. Streamwise vorticity contours on the lower wall of Case III. Blue color represents negative rotation, Red color represents positive rotation.(SS – Separation Shock, S – Separation, R – Reattachment)	86
Figure 5.10. Time history of the pressure data and the corresponding FFT’s for station L1 (above) and L10 (below) of the lower wall of Case III	87

CHAPTER 1

INTRODUCTION

Shock wave boundary layer interactions (SWBLI) occur when a shock wave interacts with an incoming boundary layer. These interactions affect the performance of air crafts that are moving with transonic, supersonic or hypersonic speeds such as planes, rockets, missiles and space shuttles. This phenomenon also affects the performance of supersonic wind tunnels. SWBLI causes flow separation, rise in the drag and flow unsteadiness [1], [2], [3]. They are one of the most important examples of the viscous-inviscid flow interaction. SWBLI occurs with a shock wave (inviscid) and a boundary layer (viscous) so the numerical models should have the ability to capture flow physics of both parts of the flow. Also, for most of the cases Reynolds number is considerably high since the flow has high speed and air has low viscosity, making it even more difficult to model the smallest turbulent scales. Thus, numerical simulation of SWBLI is a challenging problem.

SWBLI can occur in several geometries, such as the following [4]

- Compression ramps: These type of flows are generic representations of supersonic air intakes and diffusers of supersonic wind tunnels. In this thesis, this configuration will be studied as Case I. The physics of compression ramp flows is shown in Figure 1.1.

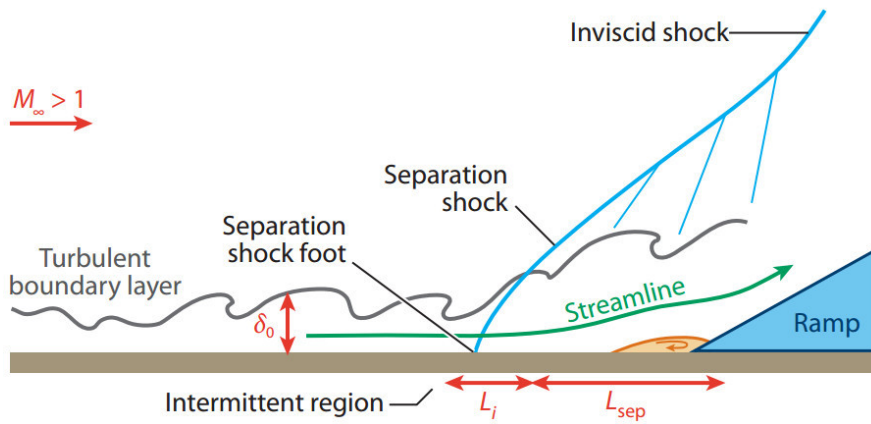


Figure 1.1. Schematic of SWBLI on a compression ramp [5]

- Impinging shocks due to forebody effects: SWBLI due to impinging shocks have slightly different flow physics than the compression ramp flows as can be seen in Figure 1.2. In this case, separation of the flow is caused by the pressure gradient created by the impinging shock. When the impinging shock hits the boundary layer, a reflected shock takes place. Impinging shock on to a boundary layer will be studied in this thesis as Case II.

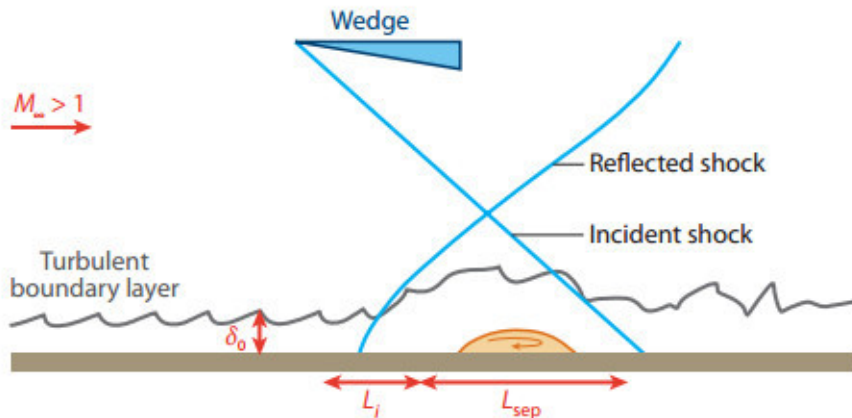


Figure 1.2. Schematic of a shock impinging on a wall [5]

- Corner-flow: Corner flow occurs near the fins and wings of missiles or aircrafts where these parts are joined with other parts such as the body of the aircraft. An example of such flows can be seen in Figure 1.3.

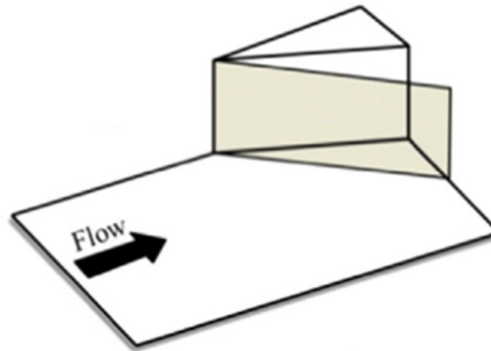


Figure 1.3. Schematic of a corner flow [6]

- Expansion corner: Expansion corners, an example of which can be seen in Figure 1.4, are the geometries that mostly come after compression corners for supersonic air intakes and wind tunnel diffusers.

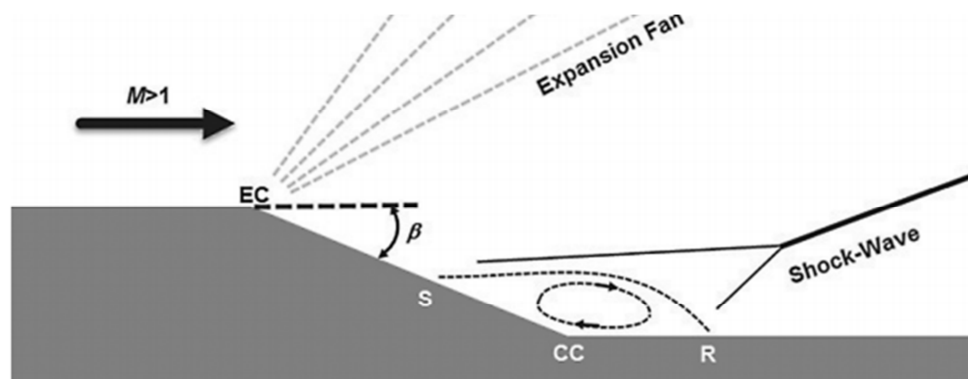


Figure 1.4. Schematic of flow at an expansion corner [7]

1.1. Flow Physics of Shock wave Boundary Layer Interactions

The general structure of SWBLI on a compression-expansion ramp can be seen in Figure 1.5 [8]. The section numbered as 1 is where the shock first interacts with the incoming boundary layer. Locations S and R show the separation and reattachment points. On the ramp, at section 3 in the figure, structures that resemble Görtler vortices can be seen, which are the array of vortices that form when a flow hits a concave surface and the instabilities in the flow grow. At section 5, reattachment shock and its interaction with the separation shock can be seen. After the ramp, expansion waves are formed at section 4.

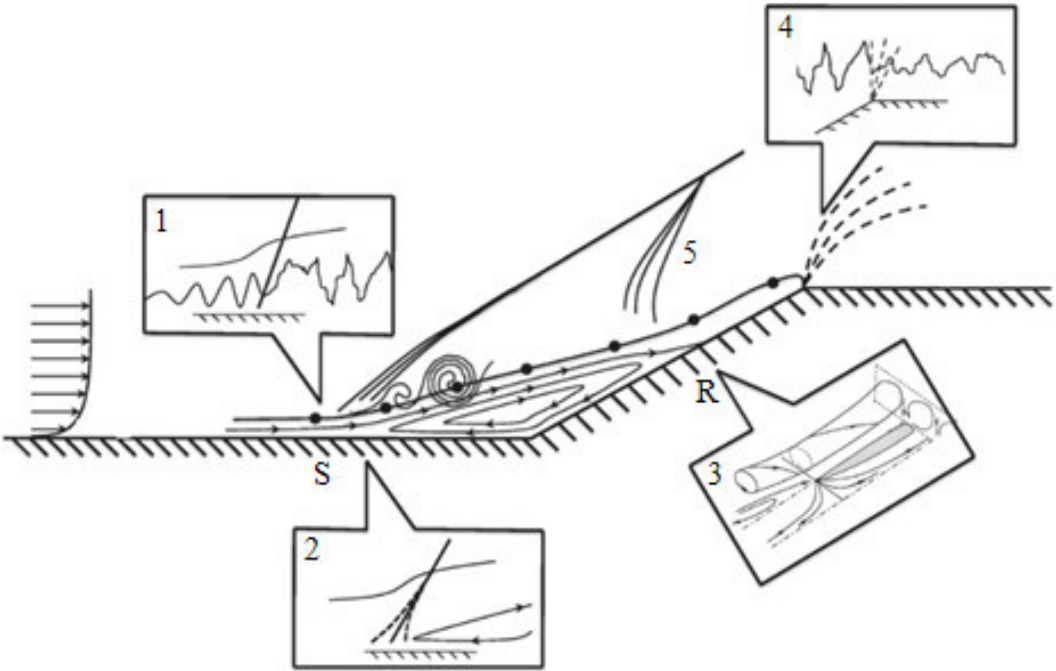


Figure 1.5. Structure of SWBLI on a compression-expansion ramp [8]

Main flow features of an impinging shock can be seen in Figure 1.6 which differs from the flow physics of a compression ramp. The flow is separated by the effect of the ramp at the upper wall and by the impinging shock at the lower wall. When the impinging shock (IS) and the separation shock (SS) interacts, a shear layer and a wake happens. A reflected shock (RS) and a transmitted shock (IS) is created by the interaction of the IS and SS with this shear layer.

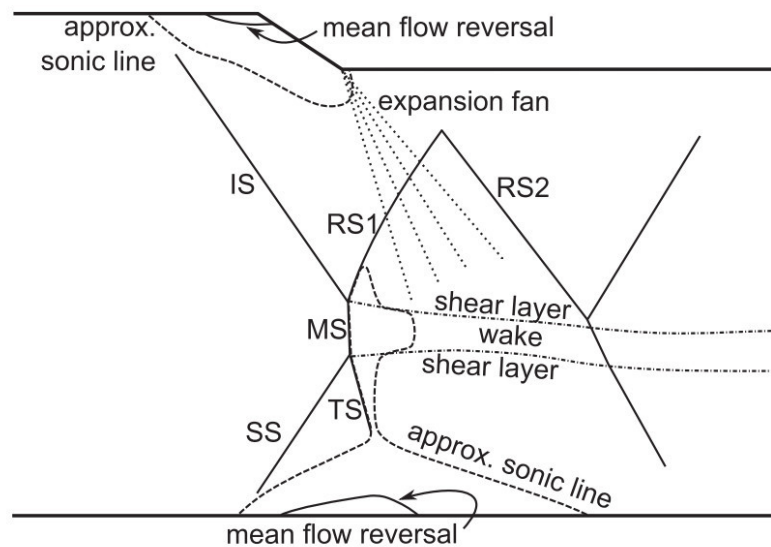


Figure 1.6. . Structure of SWBLI for an impinging shock on a wall (IS – Impinging Shock, RS – Reflected Shock, MS – Mach Stem, SS – Separation Shock, TS – Transmitted Shock) [9]

SWBLIs are studied since the 1960s. There are several experimental and numerical studies present in the literature. These studies were focused mainly on flow unsteadiness, heat transfer effects, characteristics of the incoming boundary layer, flow control and three-dimensional effects, as detailed below [6].

1.1.1. Flow Unsteadiness

Flow unsteadiness can cause fluctuations on the pressure forces and the location of flow separation, and these can harm the structural integrity of an air craft. Pozefsky et al. [10] studied an experimental hypersonic aircraft and concluded that the aircraft

cannot withstand such effects more than one minute. One of the most interesting outcomes of this flow unsteadiness phenomenon is that it has a low frequency component, which has been observed in Schlieren videos and pressure signals of experimental studies. It is observed regardless of the flow configuration or geometry [3], [6]. Its source, whether being a characteristic of the wind tunnel or a fundamental feature of SWBLI flows, is the center of many studies in the literature.

Figure 1.7 is taken from ref. [5] but its origin is Dolling and Erenkil's [11] experimental work. They took unsteady wall pressure measurements from 5 stations of SWBLI flow over a compression ramp. Figure 1.8 shows power spectral densities of these measurements. They are normalized with the standard deviation for station 2, whereas no such normalization is used for other stations. As seen, stations 2 and 3, which are near the separation zone, have lower dominant frequencies by an order of 50 than the undisturbed station 1 and downstream of the shock 4 and 5.

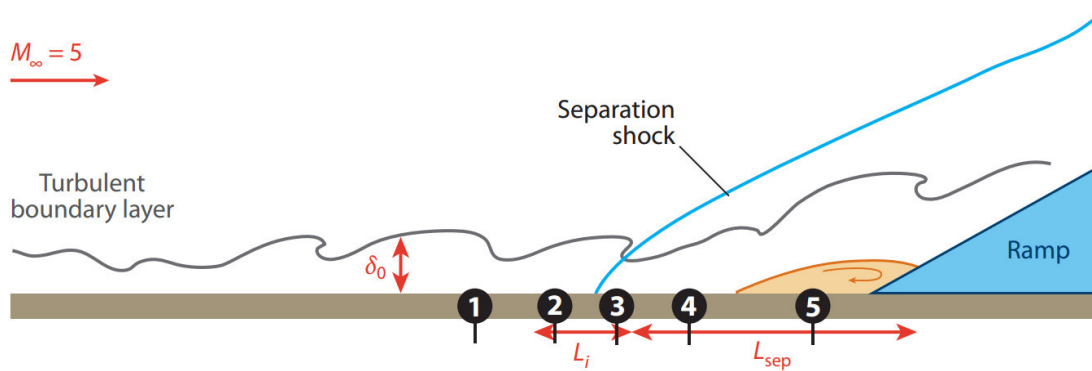


Figure 1.7. Locations of pressure measurements (taken from ref. [5])

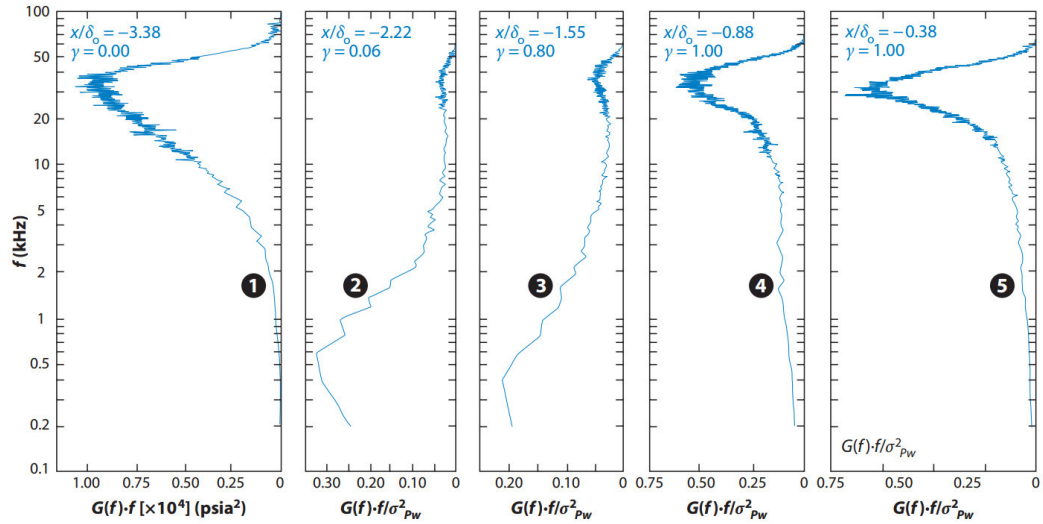


Figure 1.8. Power spectral densities of pressure signals for flow over a compression ramp (taken from ref. [5][11] (1) undisturbed boundary layer, (2,3) shock foot, (4,5) downstream shock foot

1.1.2. Heat transfer

The location and the magnitude of the peak heat transfer on a flow with SWBLI is one of the most important criteria when designing a supersonic or hypersonic air craft. Heat transfer rate becomes an important criterion especially for the re-entry vehicles. There are several experimental studies that focus on the heat transfer effects. Numerical studies based on Reynolds Averaged Navier-Stokes (RANS) methods showed that predictions perform well when the SWBLI is weak, but they totally fail when the interaction becomes stronger [3]. In Figure 1.9 the normalized heat transfer rate with respect to the normalized spanwise distance is given on a fin for a crossing shock interaction at a Mach number of 8.3 and angle of attack of 15° . It can be seen that even the best of the RANS results is far away from the experimental values. It was advised that for better results either large eddy simulation or direct numerical simulation methods should be used [3].

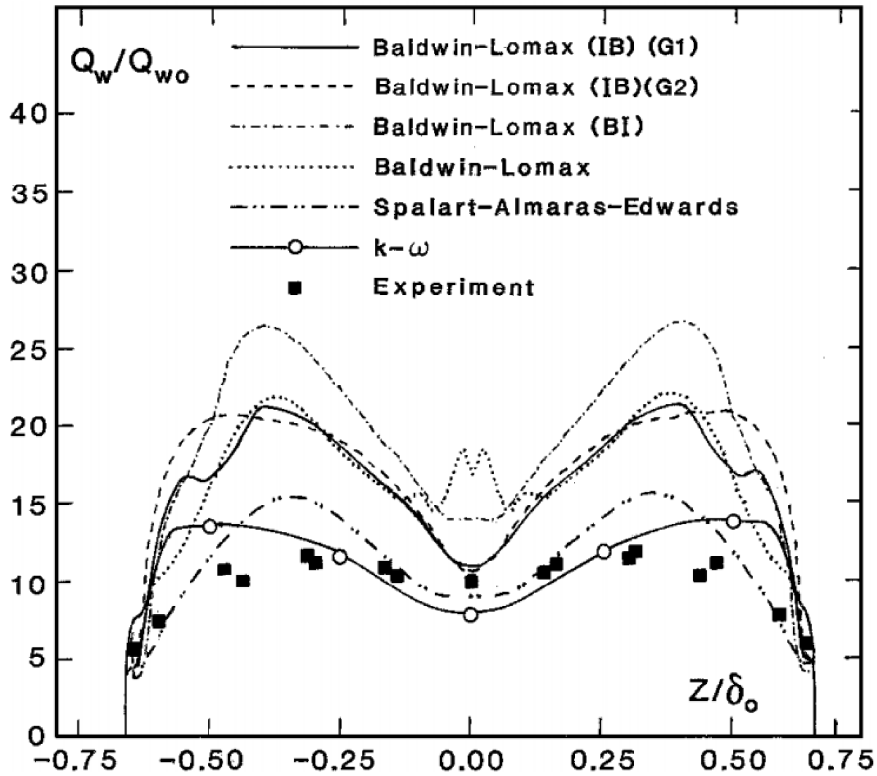


Figure 1.9. Comparison of studies calculating heat transfer rate [3]

1.1.3. Incoming Boundary Layer

Incoming boundary layer is one of the most important parameters that affects the flow structure of SWBLI. It can be laminar, transitional or turbulent and each of these characteristics has different effects on the interaction. Also, incoming boundary layer thickness and velocity profile are significant in the resulting flow features such as separation length, pressure distribution and skin friction coefficient on the wall. There are few experimental studies that investigate the effects of the incoming boundary layer to the SWBLIs. For the numerical work, both laminar and turbulent incoming boundary layers have been considered, but there is not much work on transitional boundary layers.

1.1.4. Flow Control

Control of flows with SWBLI is crucial in terms of air craft component's performance and structural stability. Flow control has been done in order to prevent flow separation or reduce the pressure loss due to the interaction. To prevent flow separation, it is recommended that boundary layer should be controlled, and to reduce the pressure loss it is recommended that shock wave should be controlled [6].

There are active and passive methods for flow control. Of these, active methods are the ones that can change their parameters as the flow conditions change. One example of such methods is the suction of the boundary layer through bleed holes [12]. This method is widely used in designing supersonic aircraft inlets. Figure 1.10 is an example of active flow control using micro-jets [13]. Passive control methods are optimized for certain flow conditions and may not necessarily work properly for others. One such method is the use of vortex generators [3].

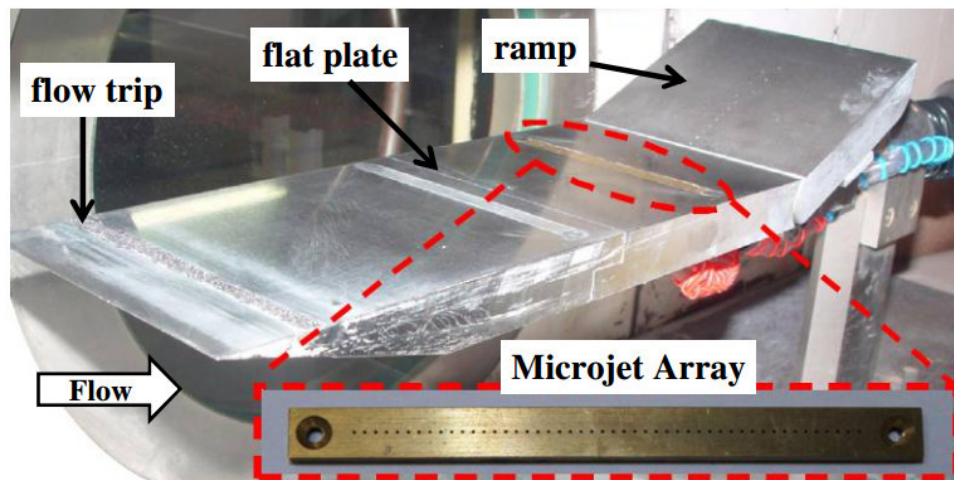


Figure 1.10. Flow control using micro-jets [13]

1.1.5. Three-Dimensional (3D) Effects

Despite the fact that the work done in the context of the SWBLI is mostly for two-dimensional (2D) geometries, one should pay close attention to 3D effects. For the purpose of investigating SWBLI effects on air crafts, three-dimensionality should be considered due to the following reasons;

- 2D modelling of SWBLIs are mostly valid for axisymmetric geometries.
- Incoming boundary layers are not necessarily perfectly 2D, so there might be cross flow in the boundary layer.
- The shocks that are interacting with the boundary layer might be skewed.

1.2. SWBLI Modelling with Large Eddy Simulation (LES)

In the literature it is stated that the aforementioned effects cannot be simulated accurately by using RANS methods [3, [5], [6]. Compared to experiments, researchers using RANS models observed severe differences on parameters such as the peak value and location of the heat transfer rate and structural load fluctuations due to flow unsteadiness [6]. These deviations are attributed to the fact that RANS simulations are based on a single scale to solve all turbulent activity, whereas flows with separation have multiple such scales [14]. Thus, it is proposed that instead of RANS methods, LES or Direct Numerical Simulation (DNS) should be used to simulate flows with SWBLI [15].

LES will be used in this thesis to simulate the flow fields with SWBLI. In LES, large scales of the turbulence are directly solved whereas the small scales are modeled. Large eddies have most of the turbulent kinetic energy so they are responsible for the larger part of turbulent mixing and momentum transfer. By using LES, these scales can be solved precisely which makes the solution more accurate. The small scales of the flow are modeled by using Sub-Grid Scale (SGS) models

There are several SGS models available in the literature, most of which use an eddy viscosity formulation. The most common model is the one proposed by Smagorinsky

and it will be used for the modelling of SGS in this thesis. Smagorinsky proposed a definition for the eddy viscosity as a function of rate of strain tensor, the dimensions of the control volume and the so-called Smagorinsky constant. Although it is a very simple SGS model, Smagorinsky model has been used successfully for many different kinds of flows. It also has pitfalls, such as the necessity of adjusting the Smagorinsky constant according to the flow type. In this study the most commonly used default value of 0.1 is used. It is also known that transitional flows are challenging for the Smagorinsky SGS model.

For large eddy simulations it is recommended that a second order non-dissipative scheme in space should be used. For most of the cases a second order central difference scheme is suggested [16]. However, for our case (flow with SWBLI) most of the researchers use Total Variation Diminishing (TVD) or Normalized Variable Diminishing (NVD) schemes [17]. Explicit time discretization is recommended [16], [17] based on the fact that the time step is already very small due to accuracy concerns making an implicit scheme unnecessary. For our case, since OpenFOAM does not contain any second order explicit time integration scheme or any Runge-Kutta solver, either Euler or Crank-Nicolson scheme shall be used. It is also stated that the Courant number should be less than 0.5 so that the information about the vortices can be transmitted to the next time step [17].

The numerical grid is one of the most important considerations for LES simulations because the grid itself is the filter to distinguish the sub-grid scales. LES grids require certain resolutions in the streamwise and spanwise directions as well as in the wall normal direction. Near wall field becomes an issue with high Reynolds numbers due to the necessity of using very small sized cells. The typical difference in RANS and LES grids can be seen in Figure 1.11, which is for a channel flow with the bottom boundary being a wall or a flat plate. As seen in the RANS grid, the cells are stretched in the streamwise direction because the main consideration is the distance from the wall in the wall normal direction. But the LES grid should be a lot finer in the

streamwise and spanwise directions than the RANS grid, in order for the spatial filtering to work properly.

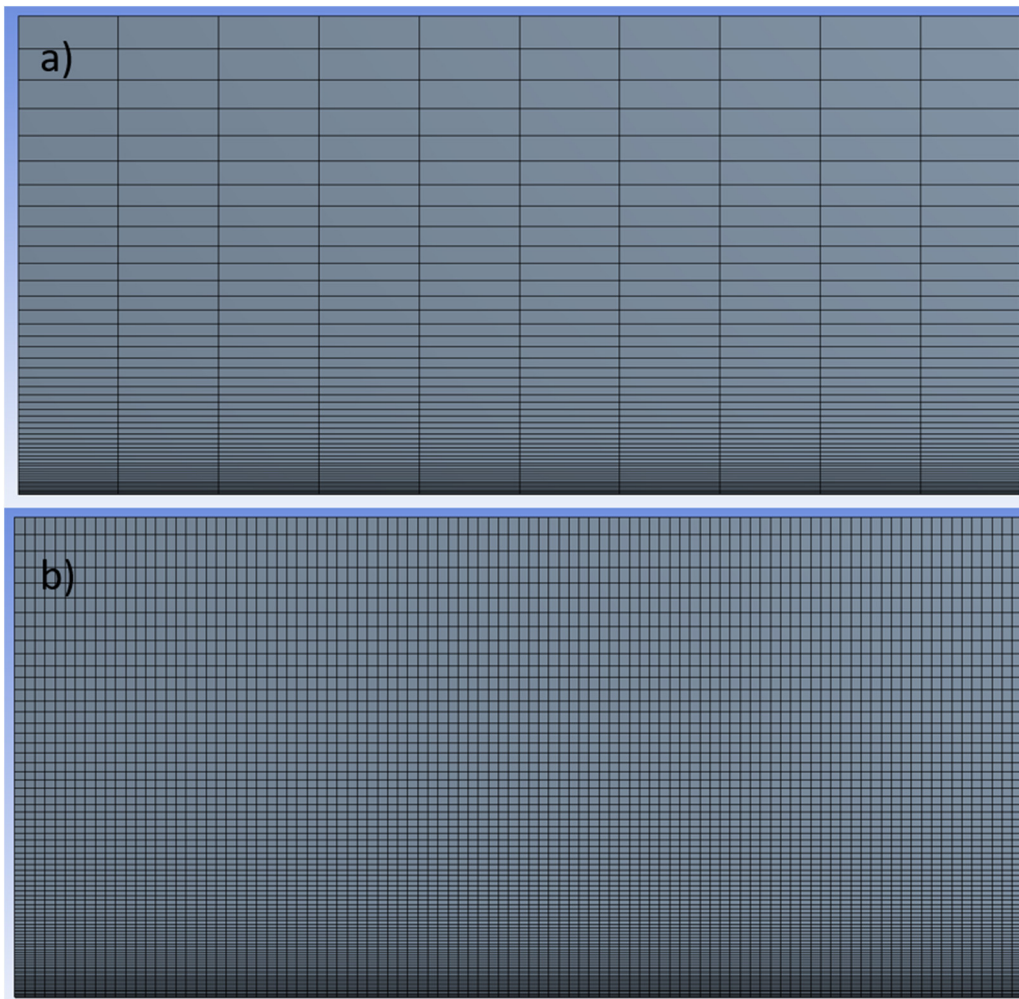


Figure 1.11. Typical near wall mesh resolutions for RANS (a) and LES (b)

The most important parameters to determine the suitability of a grid for a LES or DNS solution is the resolution of the unit spacings in the near wall region. Wall resolution in unit spacing is defined in terms of Δx^+ , y^+ and Δz^+ . Δx^+ and Δz^+ are the non-dimensional cell sizes in the x and z directions, respectively, and y^+ it is the non-dimensional distance of the first cell center from the wall. They are defined as follows:

$$y^+ = \frac{u_\tau y}{\nu}, \quad \Delta x^+ = \frac{u_\tau \Delta x}{\nu}, \quad \Delta z^+ = \frac{u_\tau \Delta z}{\nu} \quad (1)$$

where u_τ is the friction velocity, ν is the kinematic viscosity, y is the distance of the first cell center from the wall and Δx and Δz are the cell dimensions in x and z directions. The friction velocity is calculated by using wall shear stress in this formulation.

The requirements for the grid in near wall regions become a challenging problem for high Reynolds number flows and need special attention. In the literature, near wall region is either resolved, which is named as wall resolved LES (WRLES) or modeled, which is named as wall modeled LES (WMLES). These approaches are explained below:

- Wall Resolved LES (WRLES): For this approach the grid should be fine enough to resolve the inner part of the boundary layer. This is a more accurate way to solve the boundary layer than the wall modeled approach; however the computational cost is much higher.
- Wall Modeled LES (WMLES): The inner part of the boundary layer is modeled in this approach. The grid requirements for this approach are lighter than the wall resolved case since the aim is to lower the cost of computation. This approach can be implemented using different methods such as using wall functions, hybrid RANS/LES methods and Detached Eddy Simulation (DES) methods.

The difference of the computational power spent for the solution of inner and outer parts of the boundary layer is given in Figure 1.12 [18]. As the Reynolds number grows larger than 10^5 , the computational cost of the calculation of a resolved inner layer becomes higher than that of the outer layer by an order of 100.

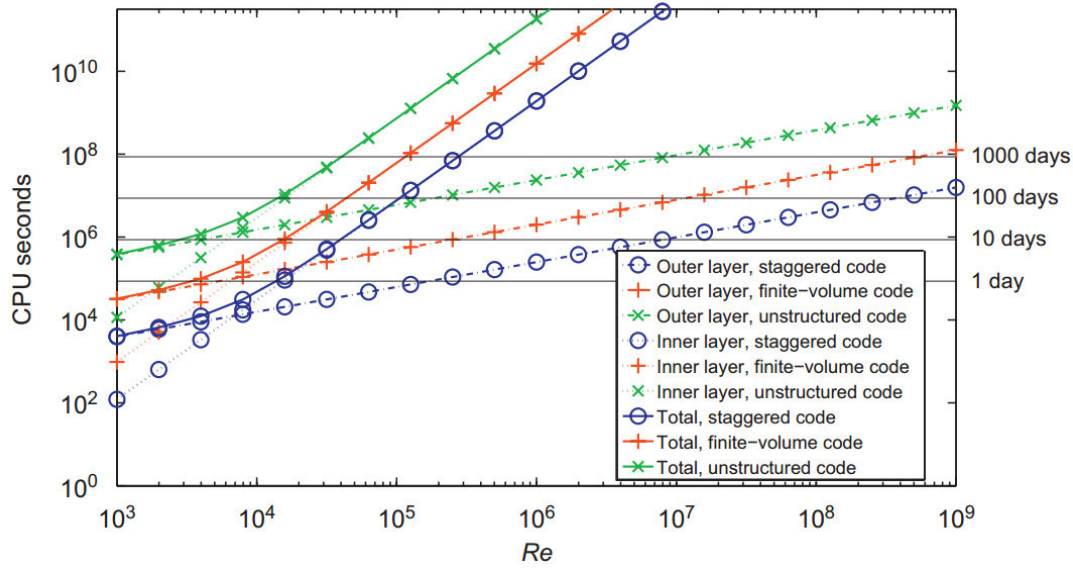


Figure 1.12. Computational costs for inner and outer layers of a flat plate simulation [18]

Considering the computational cost and time limits, wall modeled LES approach is used in this thesis. It is shown that WMLES has given fair results compared to WRLES in a variety of flows including turbulent channel flows and flows with separation [19]. However WMLES has drawbacks for the flows that have high pressure gradients, high curvatures and flows driven by outer-layers.

As it is stated before, there are several ways to model the near wall region. One of the wall modeling approaches is to use wall functions. This method uses the logarithmic law of the wall i.e. velocity at the first point in the outer layer satisfies a logarithmic law. The grid does not have to be as fine as the wall resolved solutions near the wall in every direction. The recommended grid should have 10 to 30 cells in the boundary layer in the wall normal direction [20]. When the wall function approach is used, non-dimensional distance of the first cell from the wall, y^+ , should be regulated to be in acceptable intervals [21], [22]. It is recommended that y^+ value should be from 30 to 320 [23]. This method is the cheapest in terms of computational cost. Another approach for near wall modelling is to use hybrid methods. By using them it is aimed to utilize the strengths of LES and RANS methods in a combined way. For these methods, the innermost part of the boundary layer is simulated with RANS and outer

layers are simulated with LES. Detached Eddy Simulation (DES) has a similar approach. For DES a length scale is used to switch between RANS and LES which allows that some parts of the near wall region are solved with LES - especially for separated flows - whereas hybrid methods solve all of the innermost part of the boundary layer with RANS. The grid requirements are similar for both hybrid and DES methods because both utilize a RANS grid to resolve near wall regions, which requires a maximum y^+ value of 1. This makes the computational cost of these methods higher than using wall functions. It is stated that there is no apparent superiority between the WMLES methods stated above known to date [18]. Considering this fact and computational costs, an equilibrium wall model, which is a wall function is used in this thesis work.

It is known that wall functions give poor results in separation zones. One of the reasons for this is that y^+ values might get smaller than the recommended limit of 30 in the separation or reattachment zones. This situation causes problems for the logarithmic law to work properly. To get the results in a better way a new definition for the unit wall spacing in y normal direction is proposed which is given as y^* :

$$y^* = \frac{\rho C_{\mu}^{0.25} k_p^{0.5} y}{\mu} \quad (2)$$

where ρ is the density, k_p is the kinetic energy, y is the distance from the wall in y normal direction and μ is the dynamic viscosity. The values for y^* and y^+ are the same for an equilibrium boundary layer. Since y^* formulation depends on the turbulent kinetic energy instead of wall shear stress, it gives more reasonable results in the separation and reattachment zones. This is due to the fact that in those zones wall shear stress can have zero or negative values and this can lead to singularities in the calculation of y^+ . In this thesis work, the chosen wall function will utilize y^* formulation. Further details will be given in Section 3.1.

1.3. Current Work

In this thesis work, the following 3 SWBLI cases are considered.

- Compression-expansion ramp: For this configuration a ramp with an angle of 25° is used as shown in Figure 1.13. This is the case representing an air inlet ramp or a wind tunnel diffuser. The experimental and numerical studies available in the literature for this case will be used to validate the numerical approach.

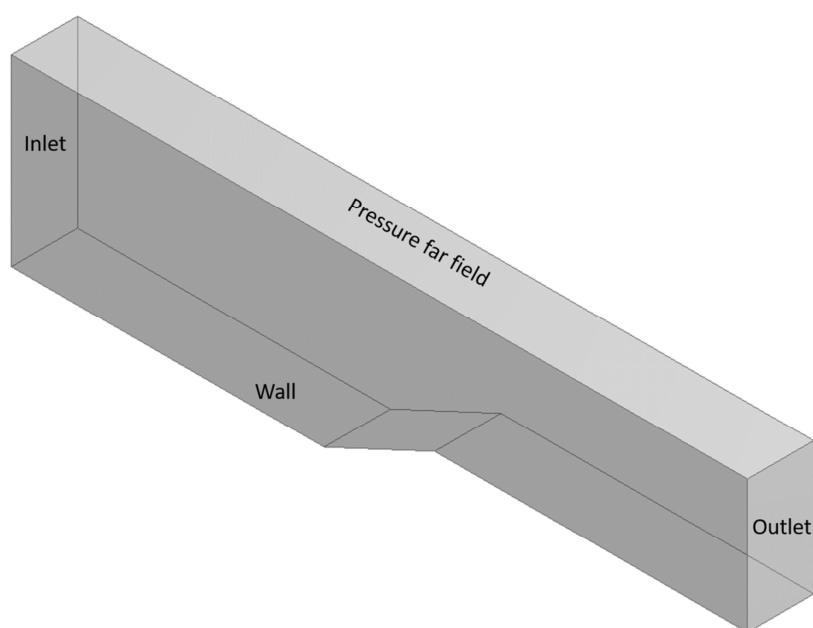


Figure 1.13. Compression-expansion ramp geometry

- Shock impinging on a wall: For this case a duct flow with a compression corner will be considered as shown in Figure 1.14. The difference between the first case and this one is that now both the bottom and the top boundaries are walls so both SWBLI on a ramp and due to an impinging shock can be investigated. There are also experimental studies available in the literature for this one, which will be used for further validation of our approach.

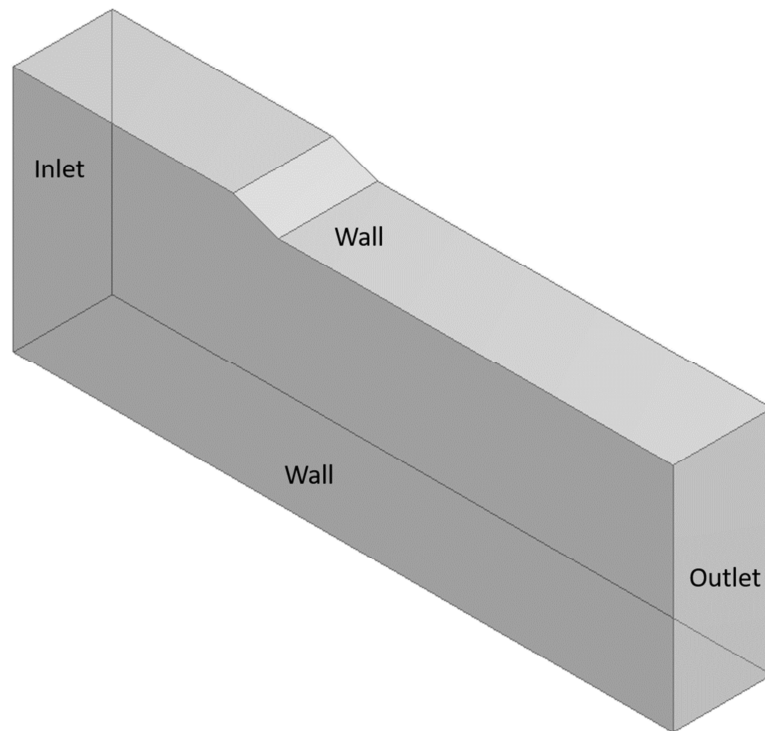


Figure 1.14. Shock impinging on a wall geometry

- Shock impinging on a compression-expansion ramp: For this case a duct flow with two ramps, one of which is creating a shock that hits the other one is investigated. This geometry represents the flow condition where forebody effects such as a nose shock interacting with an air intake's compression ramps. Also it is representative of a wind tunnel diffuser where the shock waves created by test model interacts with the compression ramp of the wind tunnel diffuser.

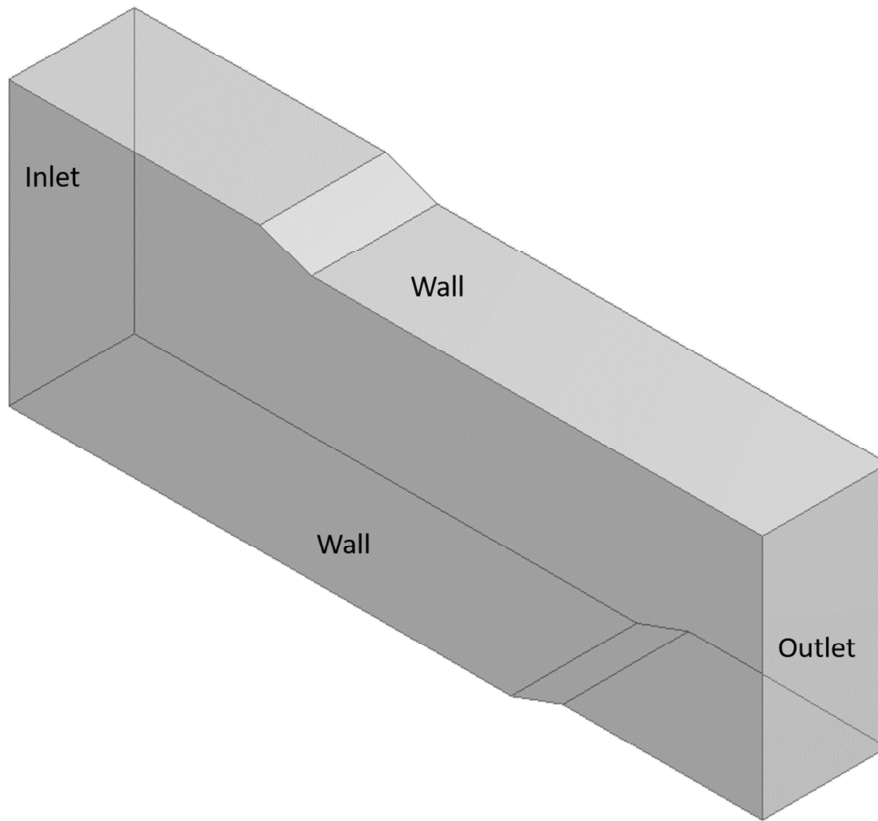


Figure 1.15. Shock impinging on a compression-expansion ramp geometry

The main parameters defining all the cases are the freestream Mach number, Reynolds number based on incoming boundary layer thickness and the ramp angle, details of which will be shared in the upcoming chapters. Wall pressure distributions, velocity profiles inside the boundary layers, wall shear stresses and frequency content of wall pressure fluctuations will be studied in detail. WMLES simulations with wall functions will be done using the freely available, open source CFD software OpenFOAM.

In chapter 2, literature review on SWBLI will be given, mainly by focusing on the geometries of the aforementioned cases. In Chapters 3, 4 and 5, simulation details and results for the three cases mentioned above will be presented. The thesis will end with the conclusions in Chapter 6.

CHAPTER 2

LITERATURE REVIEW

Shock wave boundary layer interaction has been studied both numerically and experimentally since 1960s. Some of the work done on this subject are summarized in Table 2.1. Researchers have investigated the flow field characteristics, unsteadiness and effect of geometry on SWBLI for both control and performance considerations. Experimental work included oil-flow visualizations, Schlieren photography, Particle Image Velocimetry (PIV), pressure measurements and temperature measurements. Transonic, supersonic and hypersonic flow regimes with mostly turbulent boundary layers have been studied. Numerical work has been done to simulate SWBLI with the help of both in-house developed and commercially available software. These studies included both laminar and turbulent boundary layers. To simulate turbulent boundary layers, researchers have used several methods such as RANS, LES, DES and DNS.

In Table 2.1 and in the paragraphs that follow it, Re_δ and Re_θ mean the Reynolds number based on the incoming boundary layer and momentum thicknesses measured at specific locations. In this table Reynolds number values with units of m^{-1} are calculated without using a reference length.

In the following sections, first the numerical and experimental studies found in the literature for the first two cases mentioned in Chapter 1, namely compression expansion ramp flows and impinging shock on a wall, are detailed. To this date there is no work either numerical or experimental for the 3rd case that will be investigated in this thesis. After that, a literature review on WMLES, and the use of OpenFOAM for SWBLI will be given.

Table 2.1. Summary of the SWBLI Literature

Ref. No.	Year	Problem Domain	Important Parameters	Comments
[24]	1962	Flat plate with impinging normal shock	Experimental. Ma: 1.1, 1.2, 1.3	A new theory to calculate adverse pressure gradient effects on turbulent boundary layers
[25]	1970	Air intakes	Experimental. Ma: 0.78 - 1.83	Performance of air intakes with different shapes and sizes
[4]	1971	Review	-	
[26]	1985	Compression ramp	Experimental Ma: 3.0 Re: 7.8×10^5 and 1.4×10^6	Wall pressure signals are taken. Large amplitude pressure fluctuations are seen.
[27]	1986	Unswept semi-infinite circular cylinder	Experimental Ma: 5.0	Power Spectral Density (PSD) of the pressure signal is mostly Gaussian in the incoming region, but not for the separation region.
[28]	1992	Fin induced SWBLI	Experimental Ma: 2.95, 3.95 Re: $58 \times 10^6 \text{ m}^{-1}$ to $72 \times 10^6 \text{ m}^{-1}$	Flow field features are investigated using imaging.
[29]	1995	Cylinder with a 20° half angle conical flare	Experimental Ma: 3 Re: $15 \times 10^6 \text{ m}^{-1}$	Skin friction and wall pressure measurements. Flow field structures are observed via oil flow visualizations
[21]	1996	Review	-	
[30]	1996	Wing-flap and wing-fuselage junction configurations	Numerical. RANS Ma: 11.19 - 17.76 Re: $\sim 10^6$.	2D and 3D configurations. Dependence of the Separation length and the performance of the wing-flap and wing fuselage on ramp parameters, sweep angles and nose shape.
[31]	1996	Review	-	
[32]	1997	Cylinder/Offset flare	Numerical. RANS Ma: 2.89 Re: 15×10^6 .	Different RANS models are used. Flow field structures and topological features are examined. Flow features are similar to experimental observations except for the secondary features.

[33]	1997	Convex corners	Experimental. Ma: 7.2 Re: $85 \times 10^6 \text{ m}^{-1}$	Schlieren photography. Flow field structures are examined by paying special attention to the separation zones.
[34]	1998	Compression ramp	Numerical DNS Ma: 3.0 Re: 1685	Details will be given in Section 2.1.
[35]	1998	Air inlet	Experimental Ma: 6.0 Re: $4 \times 10^6 \text{ m}^{-1}$	Different inlet geometries and bleed parameters that affect the inlet performance are examined.
[36]	1998	Bump flow. Flat plate. Compression corner	Numerical RANS Ma: Transonic, 2.89, 2.85 Re: $57 \times 10^6 \text{ m}^{-1}$, $63 \times 10^6 \text{ m}^{-1}$	Different configurations with different RANS turbulence models. Results compared with the experiments.
[37]	1999	Compression corner and the three-dimensional asymmetric double fin configuration	Numerical RANS Ma: 2.84, 3.95, 7.39 Re: $63 \times 10^6 \text{ m}^{-1}$, $17 \times 10^6 \text{ m}^{-1}$, $86 \times 10^6 \text{ m}^{-1}$	Results compared with experiments of two different configurations. Skin friction and surface pressure in good agreement for the 2D case but not for the 3D case. Heat transfer rates never in good agreement.
[38]	1999	Asymmetric double fin geometries with angles of 7° , 11° and 15°	Numerical RANS Ma: 3.95 Re: $87.5 \times 10^6 \text{ m}^{-1}$	Results are compared with experiments Flow features such as separation lines, vortex structures, and separation and reattachment shocks are investigated
[39]	2000	Review	-	
[40]	2001	Compression ramp	Numerical Ma: 3.0 Re: 1685	Details will be given in Section 2.1.
[41]	2002	Compression ramp	Numerical LES Ma: 3.0 Re: 1685	Details will be given in Section 2.1.

[42]	2002	Two sharp fins mounted on a flat plate	Both experimental and numerical with RANS. Ma: 4 Re: $88 \times 10^6 \text{ m}^{-1}$.	Results found to be in good agreement for the weak interaction case but discrepancies get higher with the stronger interactions.
[43]	2003	Review	-	
[44]	2004	Review	-	
[45]	2005	Compression corner	Numerical LES Ma: 2.0 Re: 4×10^5 .	Good qualitative agreement with the experiments. More effort should be put to get quantitative results.
[46]	2005	Oblique shock wave impinging on flat plate	Experimental. Ma: 2.3 Stag. pres. and temp.: 500 kPa and 300 K	Examines the structure of the SWBLI. Unsteadiness is investigated.
[47]	2005	Review	-	
[48]	2006	Compression corner	Numerical, LES Ma: 2.95 Re: 63560.	Details will be given in Section 2.1.
[49]	2006	Review	-	
[50]	2006	Compression corner	Numerical, DNS Ma: 3.0 Re: 2100	The flow field features such as shocks and length scales of turbulence are presented.
[51]	2006	Incident shock wave on a flat plate	Experimental. Ma: 2.1 Re: 53000	PIV visualizations. Good agreement with the theoretical results of their previous work in terms of skin friction coefficient and velocity profiles.
[52]	2007	Compression Ramp	Numerical, LES Ma: 2.9 Re: 2300.	Details will be given in Section 2.1.
[53]	2007	Flat plate	Numerical, RANS Ma: 2.7 Re: $20 \times 10^6 \text{ m}^{-1}$	Influence of surface roughness. Performance of different RANS turbulence models.

[54]	2007	Compression ramp and axisymmetric cone flare	Numerical, RANS Ma: 2.9, 11 Re: $20 \times 10^6 \text{ m}^{-1}$	Spalart-Allmaras model, Menter's SST model, and Olsen & Coakley's lag model RANS cannot predict size of the separation, wall pressure distribution and skin friction coefficient.
[55]	2007	Scramjet inlet and combustor	Both experimental and numerical with RANS Ma: 8.65 Stag. pres. and temp.: 30.7 MPa and 1310 K.	Prediction of flow through a new turbulence model which is specially designed to predict separation.
[56]	2008	Review	-	-
[57]	2008	Review	-	-
[58]	2009	Review	-	-
[59]	2009	Compression Ramp	Experimental Ma: 2.0 Stag. pres. and temp.: 261 kPa and 292 K.	High speed PIV. Unsteady characteristics of the flow are measured for all scales.
[60]	2009	Compression corner	Numerical, DES Ma: 2.3 Re: 4600	DES simulation results are compared with the available experimental data. Agreement with the experimental data observed.
[61]	2009	Flat Plate with impinging shock	Numerical, RANS Ma: 2.5 Re: 1200	For low Re numbers, newly developed WENO scheme is found to be 3 times faster than standard WENO scheme.
[62]	2011	Oblique shock, single-fin and axisymmetric cone-flare	Numerical, RANS Ma: 5 to 13.	A shock unsteadiness model was developed. It improved prediction capabilities for separation length, pressure distributions and skin friction coefficient.
[63]	2012	Flat plate with impinging shock	Numerical, LES Ma: 2.3 Re: 5000	The computations are compared with experiments, with a special emphasis on the unsteadiness of the interaction region.

[64]	2012	Flat plate with impinging shock	Numerical. LES Ma: 2.3 Res: 5350	LES and experimental data are compared, and found to be in agreement. Unsteady effects are the main concern.
[65]	2012	Compression-expansion ramp	Numerical. LES Ma: 2.88 Res: 132000	Unlike previous studies, LES simulations are done at the same Reynolds number as Zeltodorov's [49] experiments and observed to be in good agreement.
[66]	2013	Compression ramp	Numerical. RANS Ma: 5 to 11.63 Res: 165000 to 800000	Flow field characteristics are investigated and found to be in good agreement with the experimental results.
[67]	2013	Compression-expansion ramp	Numerical. LES Ma: 2.88 Res: 132000	First LES study for the compression expansion ramp. Results agree with the experiment in terms of mean surface pressure distribution, skin friction, mean velocity profiles, velocity and density fluctuations.
[51]	2013	Review	-	
[68]	2013	Compression ramp	Numerical. LES Ma: 2.0 Re: 100000	The agreement between time averaged LES results and the experimental results is reasonable.
[61]	2014	Review	-	
[69]	2014	Compression ramp	Numerical. RANS Ma: 2.85 and 2.94.	Increasing discrepancies with the experimental values with the increasing ramp angle.
[70]	2015	Compression ramp	Numerical. WMLES Ma: 2.88 Res: 132000	Details will be given in Section 2.1.
[71]	2015	Compression ramp	Numerical. DNS Ma: 2.88.	Details will be given in Section 2.1.
[9]	2015	Compression ramp and impinging shock on flat plate	Experimental Ma: 2.05 Res: 188000	Details will be given in Section 2.1.
[72]	2015	Overexpanded Nozzles	Numerical. RANS Nozzle Pressure ratios: 30, 40 and 60	Turbulent boundary layer separation inside overexpanded nozzles are investigated.

[73]	2015	Compression ramp	Numerical. RANS Ma: 3.0 Re: $63 \times 10^6 \text{ m}^{-1}$.	Performed to gain preliminary insight into the experimental observations of Settles et al.
[74]	2016	Incident shock wave on a flat plate	Numerical. LES Ma: 2.3 Re: 20000	Spark jet control method investigated with LES and validated with PIV images.
[75]	2017	Compression corner	Numerical. Ma: 2.9.	Details will be given in Section 2.1.

2.1. Literature Review of the SWBLI for the Geometries to be Investigated

Several experimental work was done for SWBLI on a compression corner. They included different geometrical features such as ramp angle and ramp height, and different flow conditions such as Reynolds number, Mach number and incoming boundary layer thickness. In the earliest of these studies, Gadd [24] performed experiments on a flat plate with an impinging normal shock. The experiments were done with transonic speeds with Mach numbers such as 1.1, 1.2 and 1.3. The incoming boundary layer was turbulent and Gadd investigated the accuracy of a newly developed theory. Seddon [25] conducted experiments on air intakes for design purposes. His work included both subsonic and supersonic flow regimes as to design an intake that can perform in dual mode. Dolling and Murphy [26] worked on a 24° compression ramp at Mach number 3.0 with a turbulent incoming boundary layer. They focused on the unsteadiness of the shock system and the large scale fluctuations. For this thesis work, experiments of Zheltovodov [49] and Campo and Eaton [9] are especially important because they will serve as the main references to compare the results against for the first two cases to be investigated.

Zheltovodov [49] studied a compression ramp geometry with an angle of 25° , Mach number 2.90 and Reynolds number based on incoming boundary layer thickness 132000. The incoming boundary layer was turbulent and the incoming boundary layer thickness δ_0 was measured to be 4.1 mm at station 1 shown in Figure 2.1, which corresponds to $x/\delta_0 = -8.05$ with the origin being located at the start of the ramp. Ramp has a height of $z/\delta_0 = 3.44$ and length of $x/\delta_0 = 7.3$. Wall pressure measurements were taken from 13 locations shown in the figure and their locations are also given in Table 2.2 as normalized coordinates x/δ_0 . These locations are important because they are used in several following studies as well as the current one.

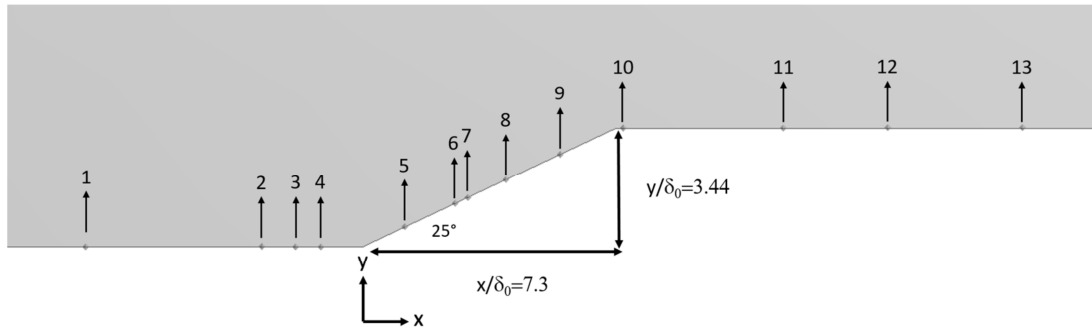


Figure 2.1. Measurement locations from experimental work of Zheltovodov (taken from Grilli et al.[8])

Table 2.2. Measurement locations of Zheltovodov (taken from Grilli et al.[8]). All locations are given in x/δ_0 .

E1	E2	E3	E4	E5	E6	E7	E8	E9	E10	E11	E12	E13
-8.05	-2.93	-1.95	-1.22	1.22	2.68	3.05	4.15	5.73	7.56	12.20	15.24	19.15

A Schlieren image from the work of Zheltovodov [49] can be seen in Figure 2.2. They observed the main flow features of the SWBLI for a compression corner. Due to the pressure gradient caused by the separation shock the flow is separated and a shear layer appeared just above the recirculation zone. Flow then reattached over the ramp and reattachment shock (and shocklets) is visible. After the flow reached the end of the ramp expansion waves formed and flow accelerated again. This case has been studied experimentally only by the Zheltovodov to the author's knowledge. Zheltovodov studied not only the 25° ramp angle at 2.9 Mach number case mentioned above, but also several other variants.

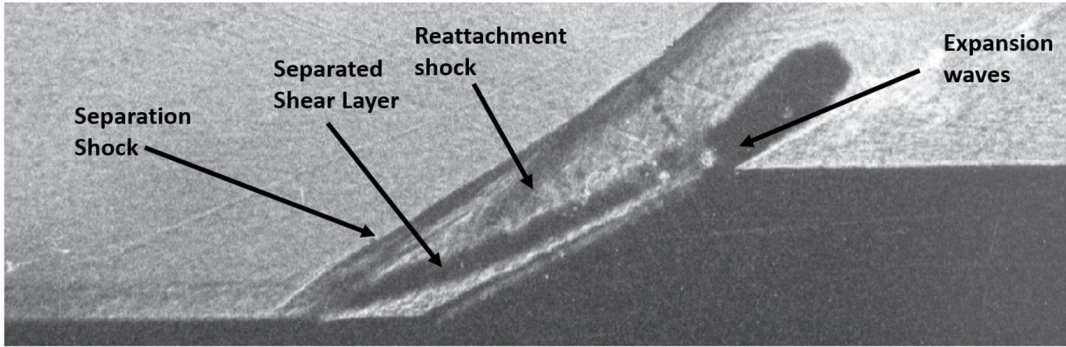


Figure 2.2. Schlieren image from the work of Zheltovodov [49].

Campo and Eaton performed a PIV study on a compression expansion ramp geometry with a ramp angle of 20° , Mach number 2.05 and a Reynolds number based on incoming boundary layer thickness 188000 [9]. Their geometry can be seen in Figure 2.3. The boundary layer was turbulent and the boundary layer thickness was measured to be $\delta_0 = 5.4$ mm at the location $x/\delta_0 = -6.48$ where origin is located at the start of the ramp. They used two ramps with heights $h = 3$ mm ($0.56\delta_0$) and $h = 5$ mm ($0.93\delta_0$), both being smaller than the incoming boundary layer thickness.

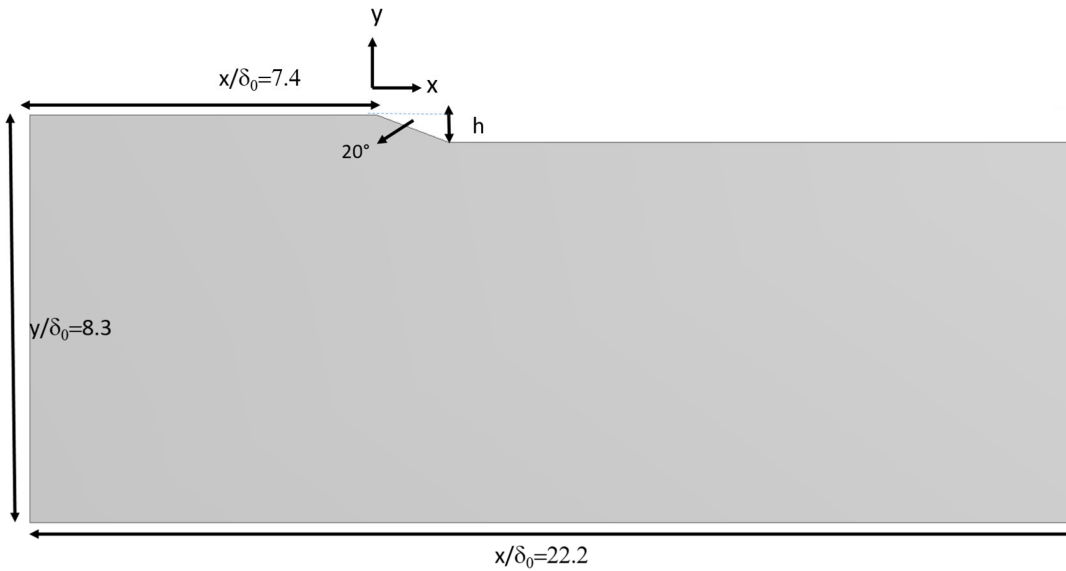


Figure 2.3. Geometry of Campo and Eaton [9]

Campo and Eaton [9] mostly presented their results in the form of contours of variables at different planes in the spanwise direction. Figure 2.4 shows one of the velocity fields they obtained from the middle plane of the test section

Flow separation occurred at the upper and lower walls due to the shocks. They observed that as the ramp height increased, SWBLI become stronger and thus resulting in bigger separation zones and complex flow fields. To the best knowledge of the author, this case was studied experimentally only by Campo and Eaton [9].

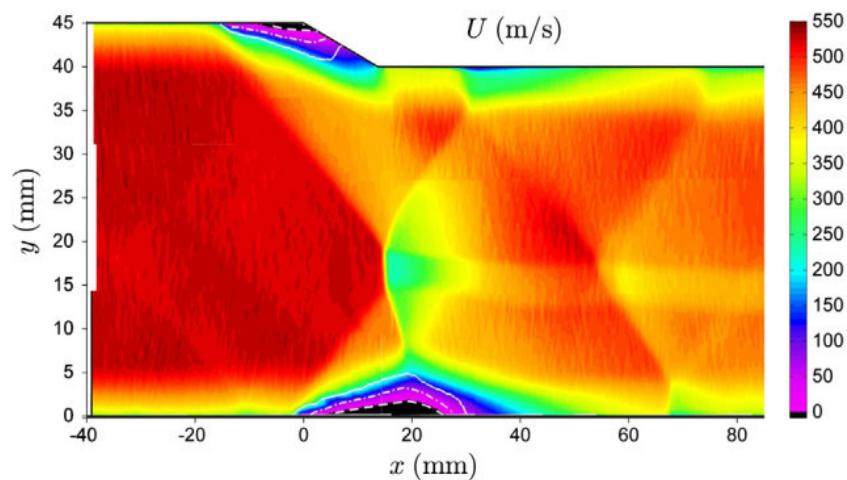


Figure 2.4. PIV work of Campo and Eaton showing the contours of the streamwise velocity component [9]

In the literature, it is possible to find several numerical studies for SWBLI on compression ramp geometries using DNS and wall resolved LES methods. Since these methods require very high resolution grids near walls for high Reynolds numbers, most of them were done using lower Reynolds numbers than the experiments.

Adams [34] performed DNS on the compression ramp geometry given in Figure 2.5, He simulated a case with Mach number 3, Reynolds number 1685 (based on the momentum thickness) and ramp angle 18° . A separate flow over a flat plate simulation was done and the boundary layer information obtained from this simulation was used in the inflow boundary of the actual simulation. He used a grid resolution of $\Delta x^+=6$, $y^+=3.3$ and $\Delta z^+=2.3$ at the inflow boundary. It was stated that the results are

reasonable in terms of flow physics, however, it is not possible to compare them with the experimental results of Zheltovodov [49] because the Reynolds number difference is too high.

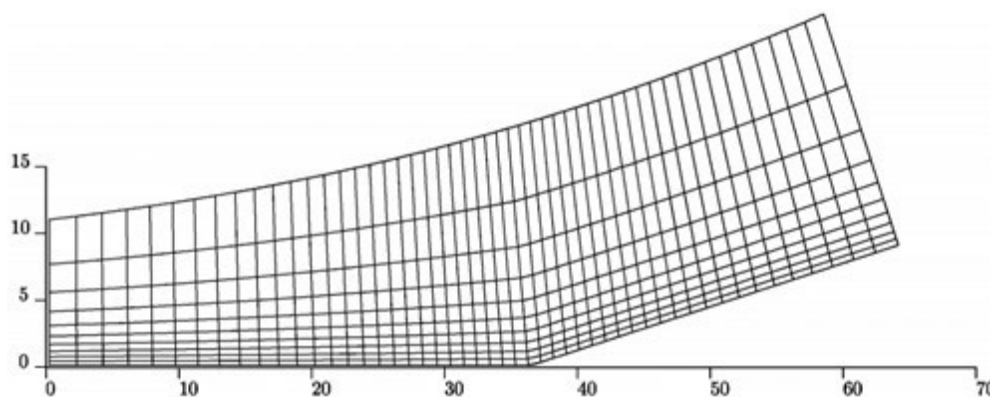


Figure 2.5. Geometry and grid (not every line was shown) for the DNS simulation of Adams [34]

Rizzetta et al. [40] studied the same compression ramp configuration that Adams [32] studied with the same parameters. They used a grid resolution of $\Delta x^+=15.1$, $y^+=1.4$ and $\Delta z^+=8.3$ at the inflow boundary. To match the boundary layer thickness and the velocity profiles to those measured in the experiments [49], they performed extra simulations to gather inflow data. They performed LES solutions using Smagorinsky and dynamic Smagorinsky subgrid stress models. They compared their results with those of Adams' [34]. They expected some discrepancies due to the differences in the incoming flow quantities and the Reynolds numbers, but they stated that their results are satisfactory compared to the experiments and Adams [34].

In another study Rizzetta et al. [41] worked on four different compression ramp geometries with angles of 8, 16, 20 and 24 degrees. For all the geometries free stream Mach number was 3.0. They used LES with dynamic Smagorinsky model and a grid resolution of $\Delta x^+=16.8$, $y^+=1.4$ and $\Delta z^+=8.3$ at the inflow boundary. All the simulations have been done at a lower Reynolds number compared to the experiments of Zheltovodov [49]. The results showed good agreement for the wall pressure distributions but the skin friction coefficients showed discrepancies.

Loginov et al. [48] studied the compression ramp configuration which is the same as the one used by Adams [34], with Mach number of 2.95. Their geometry is shown in Figure 2.6. They performed LES simulations with a Reynolds number of 63560 based on incoming boundary layer thickness using a grid resolution of $\Delta x^+=15.1$, $y^+=1.4$ and $\Delta z^+=8.3$ at the inflow boundary. Similar to the other studies, they also performed extra flat plate simulations to get proper inflow boundary information. The results showed that there are indications of large scale shock motion and amplification on fluctuations across the separation region. Although the Reynolds number used in the simulations was 2 orders of magnitude lower than the experiments, results showed good agreement in terms of mean skin friction coefficient and separation and reattachment lengths. Surface pressure distributions also compared well with the experiment, but not the skin friction distribution or the amplification of the skin friction coefficient which happens just before the flow accelerated by the expansion waves.

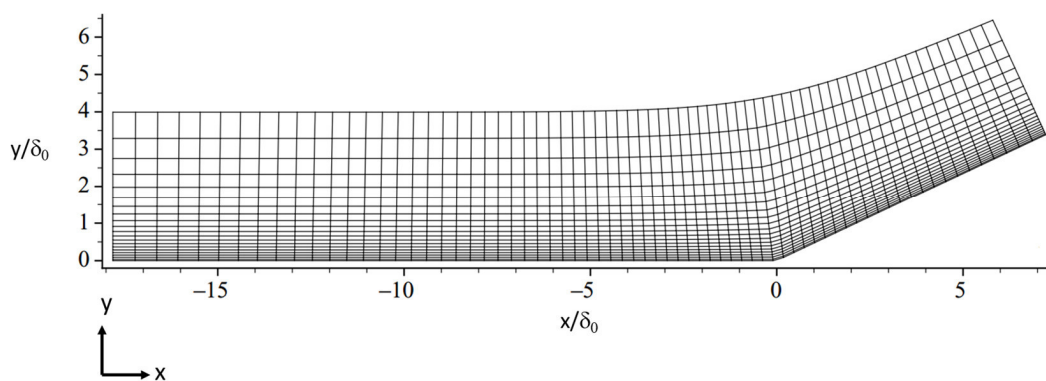


Figure 2.6. Computational domain of Loginov et al. (not every grid line was shown) [48]

Wu and Martin [52] worked on a compression corner having an angle of 24° . They performed a DNS simulation with a freestream Mach number of 2.9 and freestream Reynolds number of 2300 based on the incoming boundary layer momentum thickness. Their wall pressure measurements revealed a low frequency motion of the shock system. They found out that this shock motion takes energy from the mean flow

and pumps it into the turbulent fluctuations thus making them more unstable. They also observed the individual structures of shock system such as separation shock, separated shear layer and reattachment shock.

Tong et al. [75] worked on four different compression corners having angles of 8, 14, 20 and 24 degrees. Their domain and computational grid can be seen in Figure 2.7. All simulations were done with a freestream Mach number of 2.9 using DNS with a dimensional Reynolds number of 5581 m^{-1} . Their computational grid has a near wall resolution of $\Delta x^+ = 4.5$, $y^+ = 0.5$ and $\Delta z^+ = 3.0$. Their values for the incoming boundary layer agreed well with the previous numerical solutions of Wu and Martin [52]. Results in terms of mean pressure distribution and skin friction also compared well. They found out that as the ramp angle increases the strength of the separation shock and the amplification of the turbulent quantities rise. Moreover, the three-dimensionality of the flow also increases with the ramp angle.

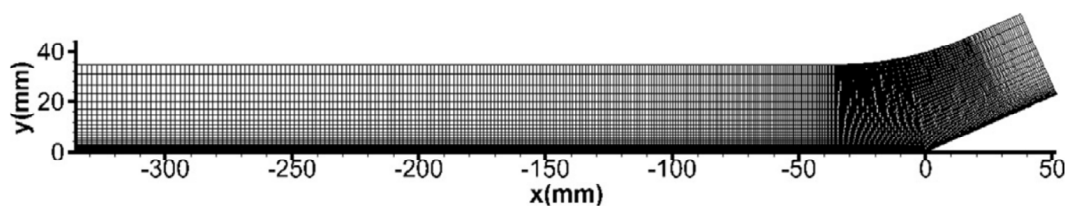


Figure 2.7. Grid used in the DNS work of Tong et al. [75]

The first numerical study that uses the whole compression-expansion ramp geometry is done by Grilli et al. in 2013 [8], in which Zheltovodov's experiment [49] is simulated using LES. This geometry differs from the aforementioned compression ramp geometries, such that the computational domain does not end at the end of the ramp but continues more to capture the expansion process too. The compression ramp angle is 25° . The simulations are done with a Mach number of 2.88 and a Reynolds number of 132840 based on incoming boundary layer thickness. The grid resolution near the wall was $\Delta x^+ = 52.9$, $y^+ = 2.2$ and $\Delta z^+ = 25.7$. The pressure distribution and skin

friction coefficient were calculated and compared with the experimental results. In Figure 2.8 the comparison between LES simulations and the experiment can be seen, with similar flow structure and shock characteristics.

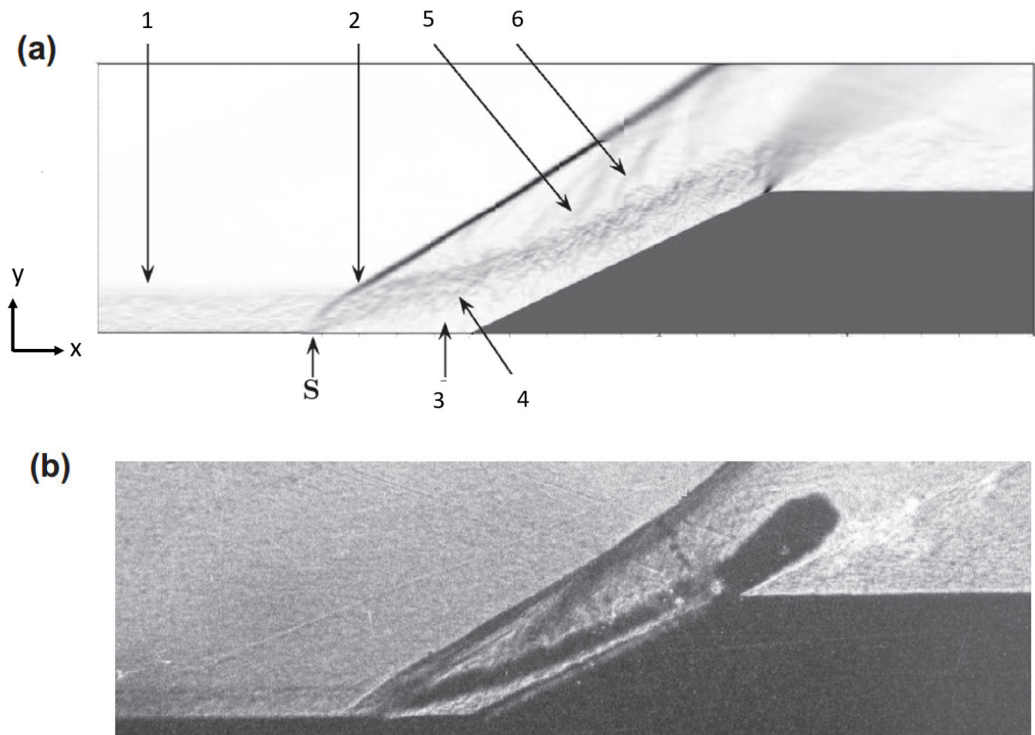


Figure 2.8. a) LES simulations of Grilli et al. [8] b) Experiments of Zheltovodov [49]

Another LES study for the same experiment was performed by Rad and Mousavi in 2015 [70]. They used ANSYS Fluent as the CFD software and utilized the wall-modeled LES technique. They used a hybrid RANS/LES method to simulate the flow field. Other than the Reynolds number used in Zheltovodov's experiments, they investigated three more values. Although they used less number of elements than Grilli et al. [8], they could get similar results to the experiments in terms of pressure distribution. However, there are discrepancies in the velocity profiles.

Fanh and Zheltovodov performed a DNS study on the compression ramp geometry in 2015 [7]. They studied the same geometry as the previous two studies summarized

above. The conditions were again the same as the previous studies, but with lower Reynolds numbers in the range of 20000 - 80000 based on the incoming boundary layer thickness. The results are compared with the experimental results and found to be similar in terms of flow structure and separation and reattachment lengths.

Up until this point, numerical work for the compression ramp geometry is presented. To the best knowledge of the author, there is no numerical based on the experiments of Campo and Eaton [9]. Also, third case of this thesis is not studied experimentally or numerically in the literature.

2.2. Literature Review on Wall Modeled LES (WMLES)

WMLES was utilized in literature for several industrial flows and the results were satisfactory for most of the cases. Piomelli et al. [76] used WMLES for two configurations; flow over a bump and a boundary layer flow with oscillatory pressure gradient. They used several wall models and stated that the equilibrium model gave the most reasonable results. Patil and Tafti [77] solved turbulent channel flow, flow over a backward facing step and a swirl combustor problems using WMLES and showed that meshes with y^+ varying from 30 to 150 give good results. For the turbulent channel flow, they stated that their results in terms of skin friction agrees with a difference of 2% with the experiments. Park and Moin [78] developed a two-layer zonal model. They applied it to several flows including highly turbulent attached flows and detached flows on airfoils and found it to be successful when compared with the results available in the literature. Park et al. [79] studied a separated flow over a bump using wall models. They kept y^+ between 40 and 70 throughout the domain. They used 5.9 million cells for the simulation. Their solution was comparable in terms of velocity profiles with the previous experimental and numerical results.

Breuer et al. [80] developed wall models to be used in practical industrial flows. They tested their implementations on a periodic arrangement of hills. They used three different grids with around 1.5 million cells. y^+ values varied between 3 to 5 for the

wall model they have used. Their results agreed well with the previous experimental and DNS studies in terms of skin friction values and velocity profiles.

One of the examples that WMLES is used to simulate flows with SWBLI is Fukushima and Kawai [81]. They simulated an airfoil at transonic speeds with Reynolds number as high as 3×10^6 based on the chord length of the airfoil. They used an equilibrium wall model which is a wall function. They stated that the pressure distributions agree well with the experimental data and WRLES solutions but the location of the shocks showed some discrepancies. Fu et al. [82] worked on a configuration of impinging shock on a flat plate at hypersonic speed of Mach 6.0. They used an equilibrium wall model and stated that WMLES performed reasonably well for the post shock boundary layer, but results are not in good agreement for separation length, skin friction or aerodynamic heating. Marco [83] studied a swept compression corner to investigate the three dimensional effects of SWBLI. His flow conditions were Mach number 2.0 and Reynolds number 4.75×10^5 based on incoming boundary layer thickness. The grid used is almost uniform throughout the domain, with near wall regions having resolutions of $\Delta x^+ = 50$, $y^+ = 60$ and $\Delta z^+ = 30$. Both equilibrium wall model which is a wall function and non-equilibrium wall models were used. It was stated that the results are in agreement with the experiments, with some differences seen in the skin friction coefficients. The grid Marco [83] used can be seen in Figure 2.9.

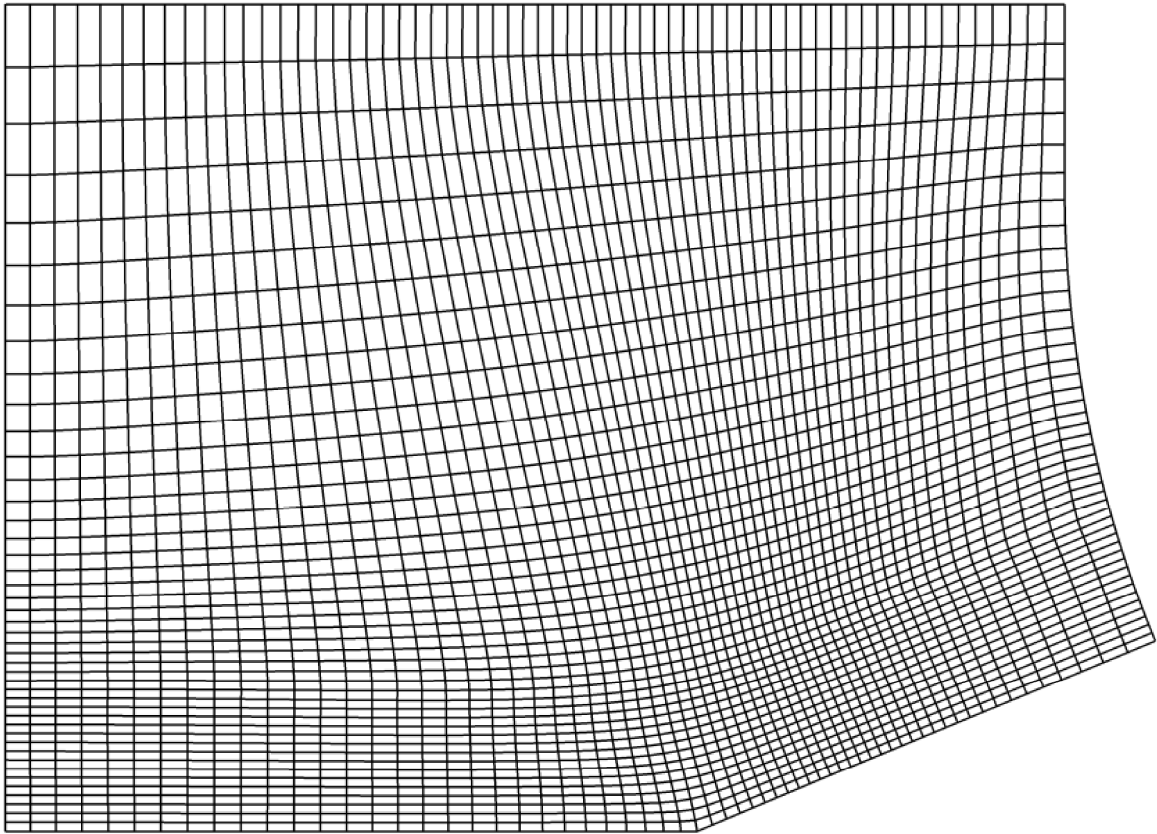


Figure 2.9. Grid used in the WMLLES study of Marco [83]

2.3. Literature Review on the use of OpenFOAM for Supersonic Flows and Compressible LES/DES simulations

In this thesis OpenFOAM is used as the CFD software. Although in the literature, OpenFOAM is mostly used for incompressible flows, there are also studies where it had been used for supersonic flows [84] ,[85] and compressible LES simulations [86], [87]. Modesti and Pirozzoli [84] used OpenFOAM to develop a low diffusive compressible flow solver and tested it with benchmark problems from the literature to get similar results. Shen et al. [85] studied OpenFOAM for all speed ranges with the classical problems of the literature and found that OpenFOAM results are similar to the ones in the literature.

One of the examples where OpenFOAM is used for compressible LES with wall models is the one conducted by Cao et al. [86]. They modeled the combustor of a scramjet engine without combustion. Freestream Mach number and Reynolds number for their simulations were 2.0 and 4.69×10^7 , respectively. They used three different grids with cell numbers of 3.28M, 6.39M and 10.69M.

Makowka et al. [87] conducted a study with OpenFOAM using a hybrid RANS/LES method to simulate the flow in a supersonic combustion chamber. The Mach number at the entrance to the combustion chamber was 2.5. They used 11.2 million cells for the mesh and utilized wall functions. Their results agreed well with the experimental results in terms of wall pressure distributions. They also compared their results with URANS simulations. Instantaneous numerical Schlieren images obtained with URANS and hybrid RANS/LES can be seen in Figure 2.10. They stated that hybrid method can get the flow features such as the shock system and the large scale oscillations better than URANS.

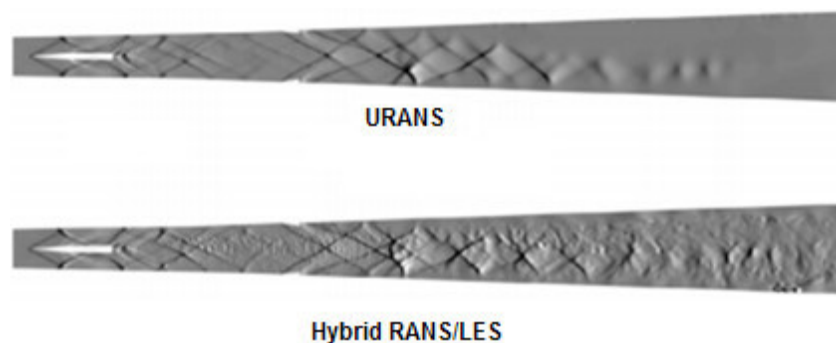


Figure 2.10. Numerical Schlieren images from the study of Makowka et al. [87]

Freitas [88] used OpenFOAM to study a deep cavity flow with transonic freestream conditions. Freestream Mach number and Reynolds number are 0.8 and 915000, respectively. Four different grids were used for the LES simulations with cell numbers ranging between 1.5M and 3.2M. A wall function was used for the near wall regions. The results were compared with the experimental work done before. It was stated that the deviation in momentum thickness is on the level of 4% and computed sound pressure levels are in well agreement with the experiment.

CHAPTER 3

SIMULATIONS OF CASE I: THE COMPRESSION-EXPANSION RAMP

In this chapter, the compression-expansion ramp geometry that was studied before experimentally by Zheltovodov [49] and numerically by Grilli et al. [8] and Rad and Mousavi [70] is considered. The geometry of the problem domain used can be seen in Figure 3.1 and the important parameters used by Zheltovodov [49] are summarized in Table 3.1.

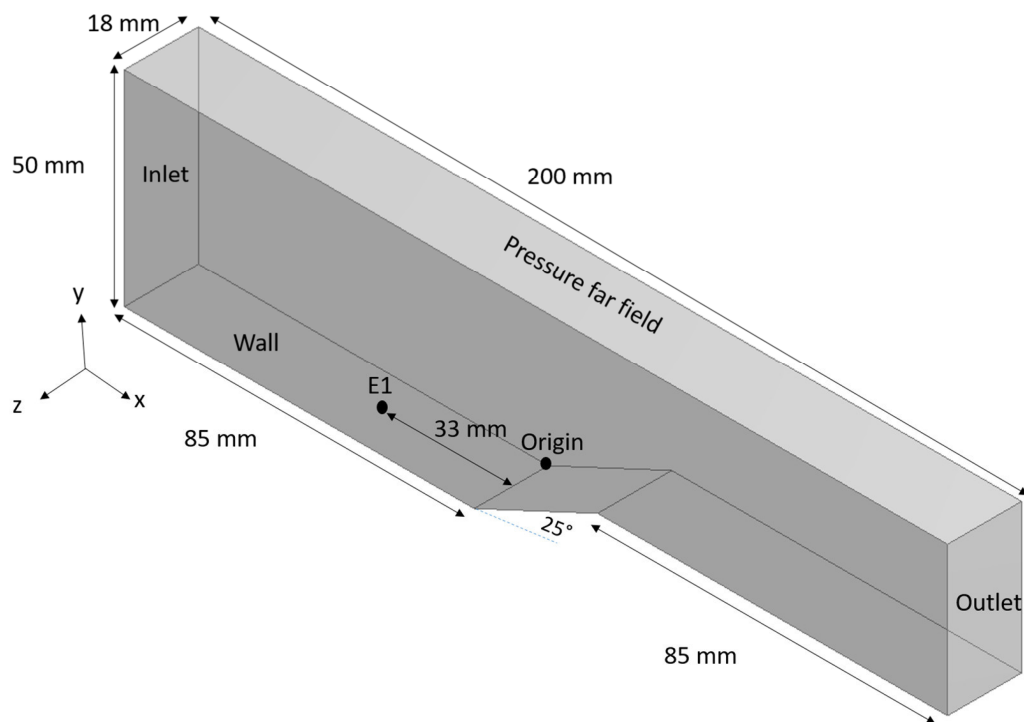


Figure 3.1. Problem geometry and boundary conditions for Case I: Compression-expansion ramp

The ramp has an angle of 25° and the domain has the extents of $12\delta_0 \times 4.4\delta_0 \times 48.8\delta_0$ (or $50 \text{ mm} \times 18 \text{ mm} \times 200 \text{ mm}$) for the height, width and length, where $\delta_0 =$

4.1 mm is the incoming boundary layer thickness measured by Zheltovodov [49] at station E1, which is 33 mm ($8.05\delta_0$) upstream of the start of the ramp (see Figure 3.1 and Table 2.2). There is an inflow boundary 85 mm ($21\delta_0$) upstream of the start of the ramp and an outflow boundary 85 mm ($21\delta_0$) downstream of the end of the ramp. The bottom boundary is a no-slip wall and the upper boundary is considered to be pressure far field. Side walls are treated as symmetry planes. It is important to note that the extents of the geometry used in Zheltovodov’s [49] original experiments is not known because the original paper is not accessible. The computational domain used here is generated by considering earlier numerical studies [8, 70].

Table 3.1. Reference values for the compression decompression ramp [49]

Mach number	2.88
Incoming boundary layer thickness at station E1, δ_0 (mm)	4.1
Reynolds number based on the incoming boundary layer thickness	132000
Free-stream speed (m/s)	618
Free-stream pressure (Pa)	12000
Free-stream temperature (K)	114

In sharing the results, lengths will be normalized with the incoming boundary layer thickness and flow variables will be normalized with the free-stream values, as it was done before in the reference studies.

Wall pressure and velocity profile data are collected from 13 reference stations shown in Figure 2.1 and Table 2.2. Additional data from 12 more stations, which can be seen in Table 3.2, are collected for a better understanding of the flow. New points are named

such that E1-1 is the extra data point that is downstream of station E1 and upstream of station E2. All the data is collected across the spanwise direction (along z) from 30 stations and for each spanwise station 30 points in the wall normal direction is used over a length of $2\delta_0$. Data is collected with a frequency of 10 MHz, i.e. $1e-7$ seconds apart. To compare the results with the references, spanwise and time averages are taken in most of the post-processing.

Table 3.2. Additional data points, in x/δ_0

E1-1	E1-2	E1-3	E1-4	E4-1	E4-2	E6-1	E7-1	E7-2	E8-1	E9-1	E9-2
-7.07	-6.10	-4.63	-3.66	0.24	0.73	3.66	4.63	5.12	6.59	8.54	9.51

3.1. Computational Model

OpenFOAM has compressible flow solvers named as sonicFoam and rhoCentralFoam. Of these, sonicFoam is the recommended one for supersonic flows, and it was the first solver considered in this study. However, results were too different compared to the reference solutions and experiments. It can be said that the recommendation of sonicFoam is for free shear flows or flows without wall boundaries. The results were very diffusive for our case. After that, rhoCentralFoam was used and better results were obtained. rhoCentralFoam is a density-based compressible flow solver using the central-upwind schemes of Kurganov and Tadmor [89], [90]. Details of the solver’s numerical schemes and algorithm can be found in [91] and [92], respectively. Time marching was done using the Crank-Nicolson scheme and all divergence terms were discretized by central differencing. After a number of trial runs it was seen that stability of the solutions requires the Courant number to be kept less than about 0.3 and to achieve this a time step value of 0.25×10^{-7} to 1×10^{-7} seconds is used, which is kept constant for each run. LES with Smagorinsky sub-grid scale model is used for turbulence. Near wall regions are modeled with “nutkWallFunction” option with default constants $C_{\mu}=0.09$, $\kappa=0.41$ and $E=9.8$. Implementation details of this wall function can be found in [93]. It uses turbulent kinetic energy to calculate the turbulence viscosity. It uses the logarithmic law of the

wall and requires the first mesh point near the wall to be in the logarithmic region. This wall function utilizes the y^* instead of y^+ to get better results in the separation and reattachment regions. For the rest of this thesis y^+ will be used as the notation for the reference station values as y^+ and y^* are equal for the undisturbed boundary layer.

Free stream values for velocity, temperature and pressure are specified at the inlet boundary. Walls are treated with no slip and adiabatic conditions. Pressure far field boundary is used with the “freestream” option of OpenFOAM, which behaves as either a zero-gradient boundary or as a fixed value boundary. It calculates the mass flow going out or coming in and automatically switches between a zero-gradient boundary and fixed value boundary. Two sides of the computational domain are taken as symmetry planes. For the side boundaries periodic boundary condition could be used also. Both methods have advantages and disadvantages and researchers used both of them in the literature [8], [70]. For stability reasons, symmetry condition is chosen and further discussion will be given about the consequences of this choice where the three dimensionality of the flow is discussed. The outflow boundary is treated with “waveTransmissive” option of OpenFOAM, which ensures that no information is reflected from the outlet of the domain.

Free stream conditions given in Table 3.1 for velocity, temperature and pressure are used as the initial conditions. Simulations are first run until 10^{-3} seconds, where the start-up transient is finished. After that, Adaptive Mesh Refinement (AMR) is applied and the simulations are continued for another 10^{-3} seconds for the system again to past the transients due to the modified mesh. The simulations are continued for 3×10^{-3} more seconds to gather the data. Figure 3.2 shows the whole simulation process for the wall pressure signal taken from station E2. The simulations were run at TRUBA HPC system of TÜBİTAK ULAKBİM High Performance and Grid Computing Center. A typical 5 ms run described above was generally completed in about 4 clock days using 48 cores.

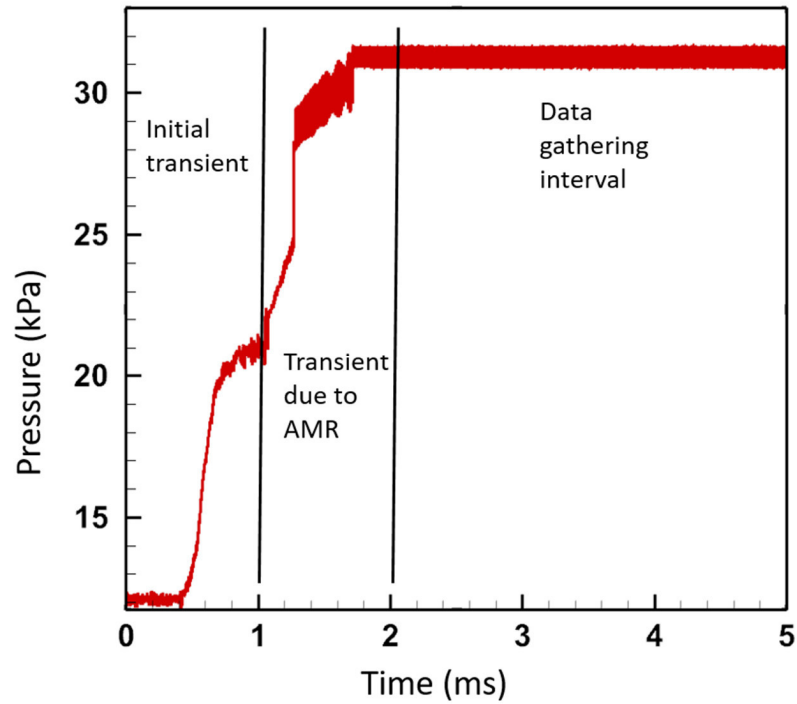


Figure 3.2. Time history of wall pressure at station E2

For the grid independence study, three different grids are constructed with approximate cell numbers of 1M (Coarse), 2.6M (Medium) and 6M (Fine). While constructing these grids, distance of first grid point from the bottom wall is kept constant to keep y^+ values between 30 and 320 [21], [22], [23] at station E1 and the number of elements in the spanwise and the streamwise directions are changed. The number of cells used in each direction for each grid and the corresponding spacings in the wall units are given in Table 3.3. For all grids at least 10 cells are located in the boundary layer.

Table 3.3. Mesh details

Mesh	Number of Elements in x, y and z directions (N_x , N_y , N_z)	Spacings in wall units at E1 (Δx^+ , y^+ , Δz^+)
Coarse	200 x 110 x 36	400, 200, 300
Medium	400 x 110 x 50	200, 200, 200
Fine	800 x 110 x 72	100, 200, 150

The meshes are constructed to have cell aspect ratios close to 1 in all three directions as seen in Figure 3.3. This is done because of the fact that the accuracy of the sub-grid scale model is known to depend on the aspect ratio of the cells [21], [94]. It is known that as the cells stretch, the constants used in the sub-grid scale model become inaccurate.

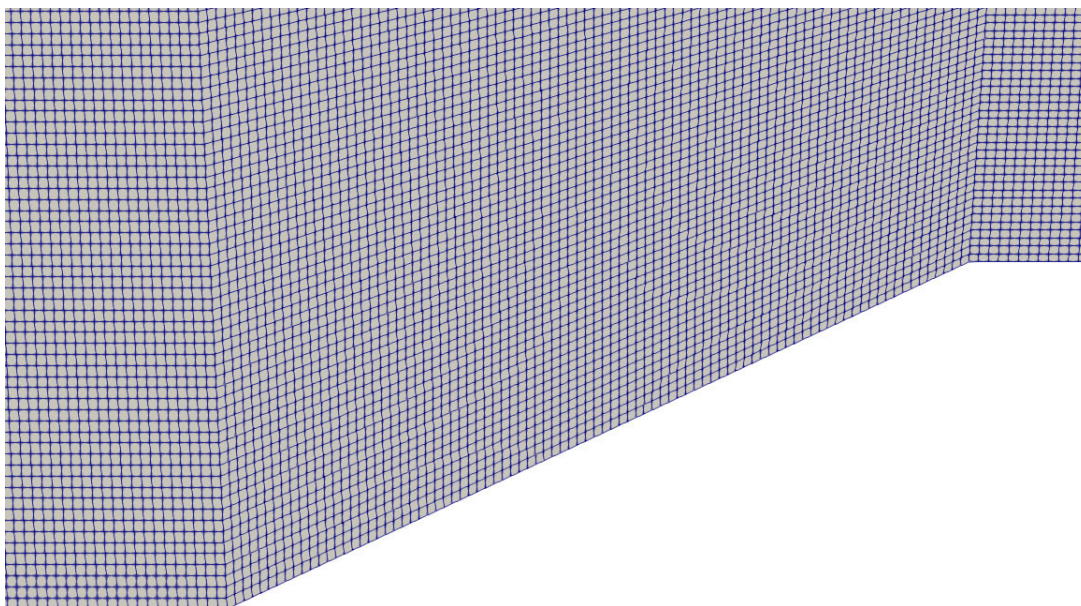


Figure 3.3. Close-up view of the Medium mesh around the ramp

Knowing that the flow domain will have shock waves, it is decided to also make benefit of Adaptive Mesh Refinement (AMR) to capture them better. By considering the performance and computational cost of the three grids given in Table 3.3 and the available resources and time, a fourth grid was constructed by applying AMR to the Medium grid, which is named as “Medium with AMR”. Details of the AMR process will be given later. This fourth grid has the same values of wall units in all directions with the Medium mesh, with a total cell count of 7.3M, more than that of the Fine mesh.

Grid independence is checked by looking at the pressure distribution along the wall and the velocity profiles at four different stations. Figure 3.4 shows the normalized

pressure variation along the wall (averaged in time and in spanwise direction and normalized using the wall pressure at station E1).

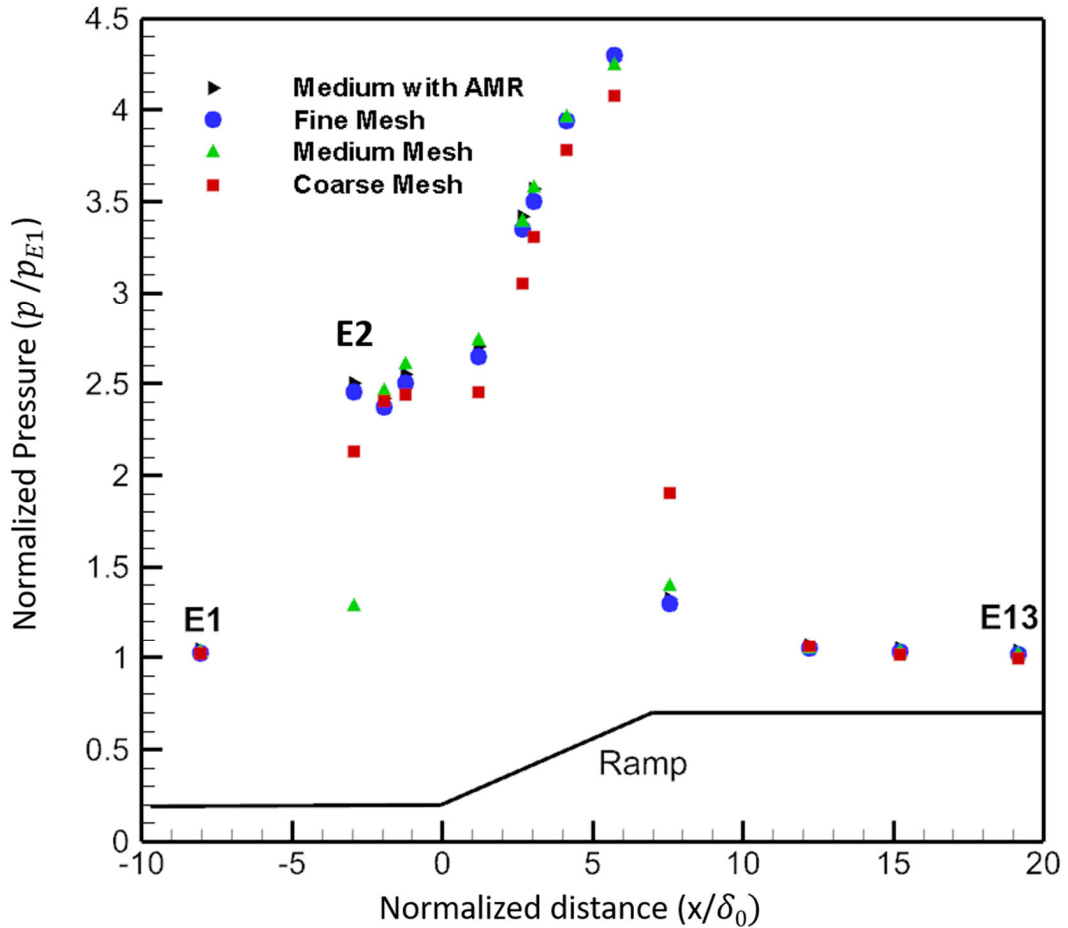


Figure 3.4. Wall pressure distributions obtained with four different grids

As seen, all grids provide the same result after the ramp. But over the ramp the coarse grid results are considerably different than the other three. The Medium and Fine grid results are very close to each other except station E2, which is inside the separation zone, for which we know that the use of wall functions is not recommended because their behavior is kind of unpredictable. After seeing the similarity of Medium and Fine mesh results, we wanted to see what would change if we continue with the Medium mesh and apply AMR to it for better shock capturing. As seen in the figure, Fine grid

and Medium with AMR grid results got even closer, the maximum difference being less than 5 %.

Velocity profiles obtained by using four different grids at four stations are given in Figure 3.5. It can be seen that the profiles for Fine grid and Medium with AMR grid are very close to each other, except station E1, where Medium with AMR result is identical to the Medium grid result because the AMR process does not affect the upstream grid.

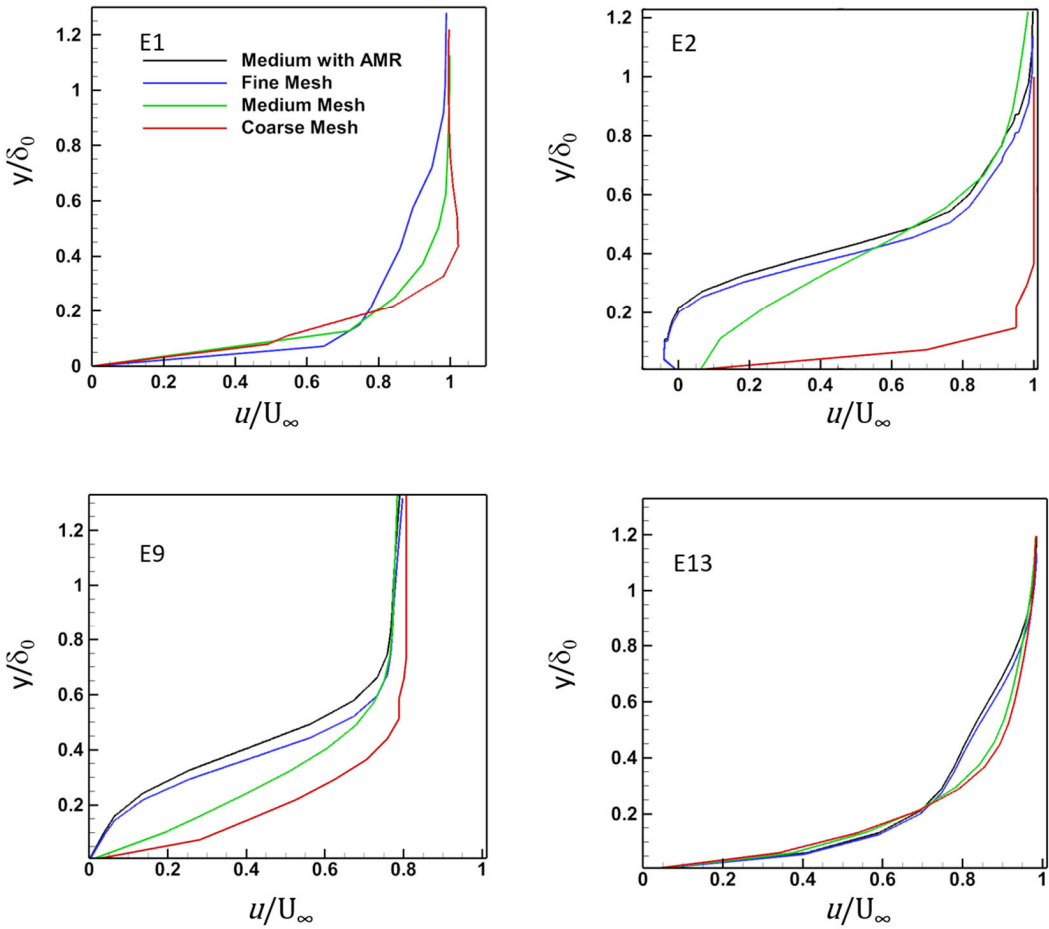


Figure 3.5. Velocity profiles obtained with four different grids at four stations.

The variation of the velocity profiles is the largest at station E2, where Fine and Medium with AMR grids predict flow separation. Although not shown in this figure, separation is also predicted by Coarse and Medium grids, but after station E2. Based

on the results presented in Figures 3.4 and 3.5, it was decided to continue with the Medium with AMR grid because it is capable of producing results similar to the Fine grid near the wall, but can capture shock details better, which is critical as will be demonstrated later.

3.2. Results and Discussion

As discussed above, Medium grid with AMR is used to obtain the results presented in this section. Gradient of the pressure is considered for mesh adaptation. Gradient of density could also be used. Actually both were tried and observed to provide similar results. Since pressure is a primitive variable and easier to work within OpenFOAM it is chosen as the variable that will be used for the AMR process. OpenFOAM does not calculate the gradients of the variables by default, which required a modification in the rhoCentralFoam.C file. 6×10^6 and 70×10^7 Pa/m are used as the upper and lower pressure gradient limits of adaptation. Part of the grid obtained after applying AMR to the Medium mesh can be seen in Figure 3.6. The cells near the shock waves and expansion waves are refined. Here the mesh is refined 2 times with a refinement factor of 2, i.e. each refined cell is divided into 8 pieces. With the use of AMR, the number of cells of the Medium grid rose from 2.6M to 7.3M.

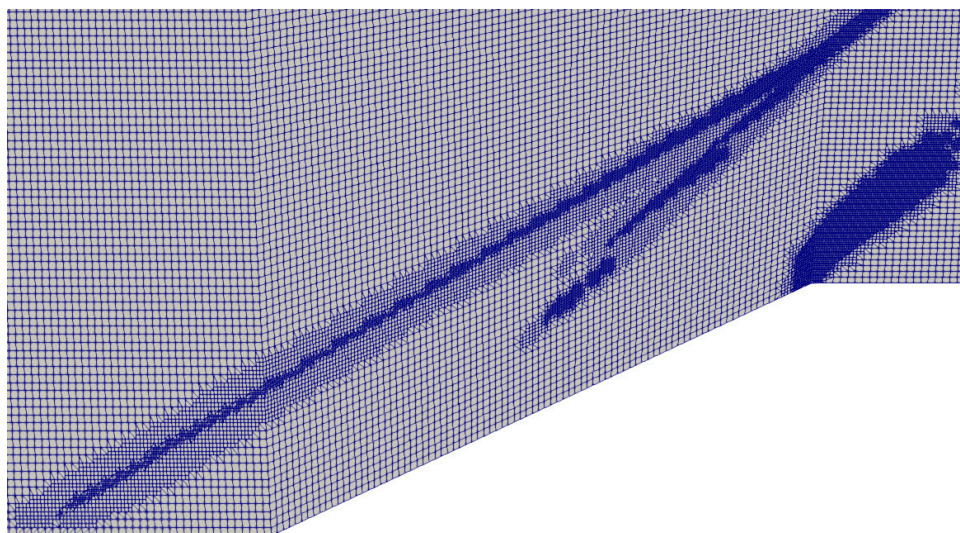


Figure 3.6. Zoomed-in view of the Medium grid after the AMR process

The contours for y^+ for this mesh are given in Figure 3.7. y^+ values are in the correct range ($30 < y^+ < 320$) for the current wall model to work properly for the most of the domain. However, the values get below 30, as low as 2, in the separation zone. This is expected since the velocity and shear stress are lower in the separation zone. As y^* is used by the chosen wall function, the separation zones are handled in a better way than using the standard wall functions that utilizes y^+ . However, discrepancies in shear stress and velocity profiles are still expected since logarithmic profiles are not suitable in such zones. These arguments are valid for Case II and Case III also.

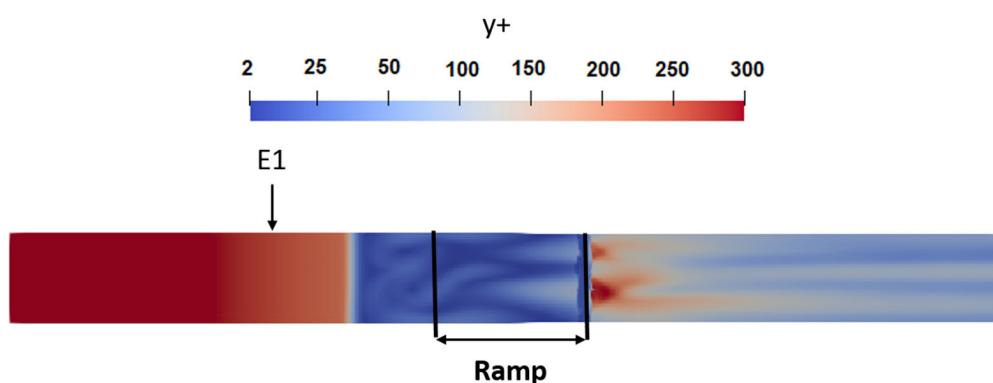


Figure 3.7. y^+ contours obtained with the Medium with AMR grid

The mesh is further checked by two other factors which are called M index and LES IQ. M index is defined as the ratio of the resolved turbulent kinetic energy to the total turbulent kinetic energy [95]. LES IQ is given by Çelik et al. [96] by the following formula

$$LES_{IQ} = \frac{1}{1 + 0.05 \left(\frac{v_{eff}}{v} \right)^{0.53}} \quad (3)$$

The contours of LES IQ and M index are presented in Figure 3.8. For both of the values it is recommended that these values should be higher than 0.8 to have a good quality LES grid [95],[96]. Blue colors represent values below 0.8 and red colors represent above 0.8 for both of the parameters. It can be stated that the values are satisfactory in most of the domain for both of the indexes except the inner zone of the boundary layer and around separation shocks. Inner layers are expected to have low

values since a wall function is used. It is also expected to have low values for these indices around the shock waves despite having those areas refined by using AMR as there is too much turbulent activity over a very small distance. Overall, mesh showed good quality for the most of the domain to do a LES solution.

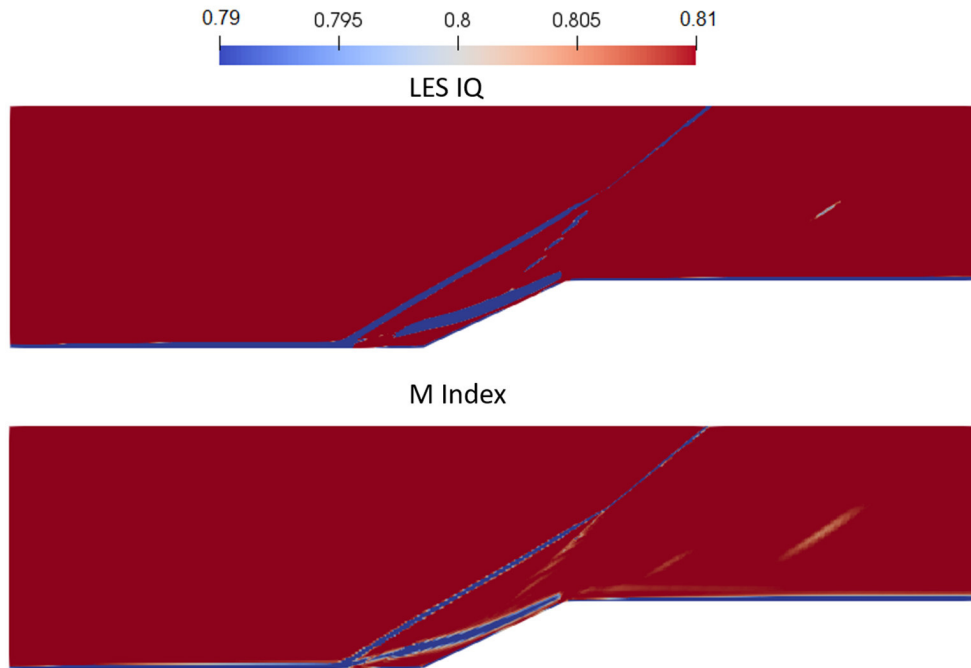


Figure 3.8. LES IQ and M index contours

Comparison of the averaged and normalized wall pressure distribution with the available reference data is given in Figure 3.9. It can be seen that the pressure distribution agrees well with the experimental values except for the separation bubble before the ramp. The trends show the same behavior for both experimental work and the current solution, but the first jump in the pressure is higher than the experimental value. The pressure distribution on the ramp itself showed good agreement except for the expansion point where the current work predicted an early acceleration of the flow, which was also observed by Grilli et al. [8]. For Grilli et al.'s work, the pressure values

are lower than the experimental values after the ramp, which is similar to our results. The deviation of the peak pressure from the experiments is 8%.

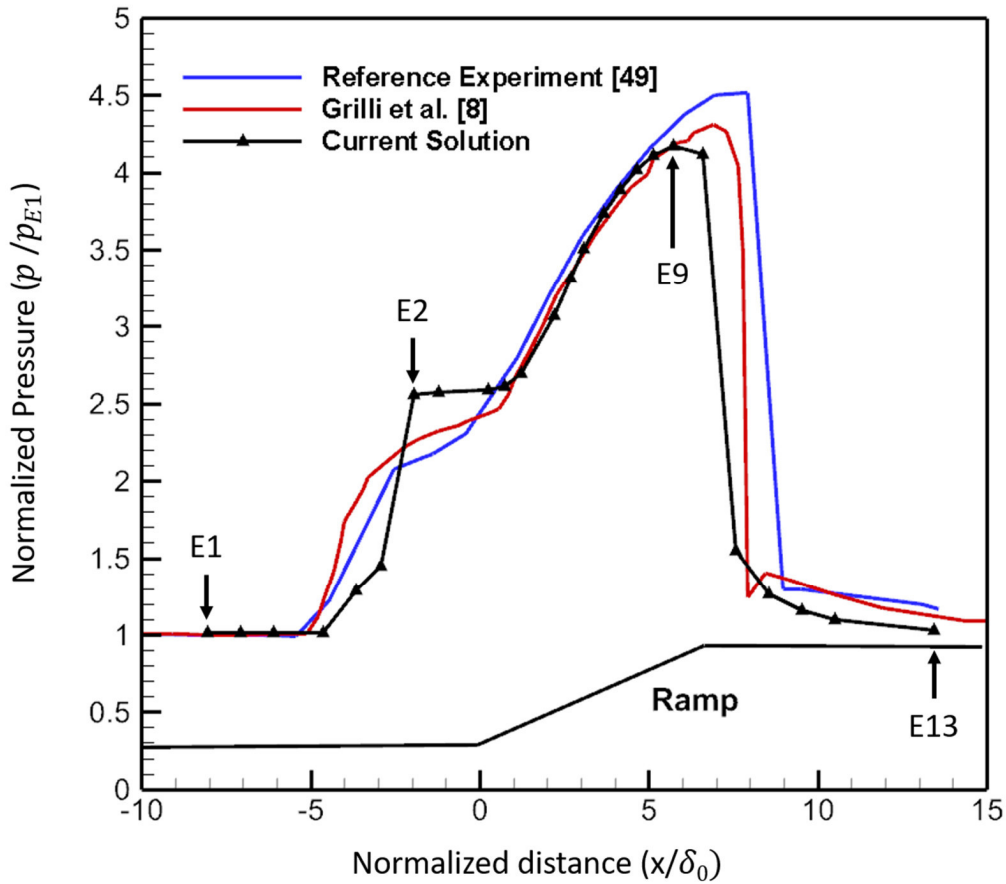


Figure 3.9. Pressure distribution along the wall (averaged in time and spanwise direction)

The velocity profiles (averaged in time and in spanwise direction) at four stations are shown in Figure 3.10, together with the numerical [8], [70] and experimental [49] reference results. The boundary layer thickness at station E1 is calculated as 3.7 mm which is 90% of the measured value. The boundary layer thickness is calculated thinner than the reference experiment which might affect the flow field characteristics, as will be discussed later. At station E1, Grilli et al.’s wall resolved LES result is identical to the experiment because they fine tune their inlet boundary condition to enforce this match. The current result is closer to that of Rad and Mousavi [70], who used a hybrid RANS/LES method to model the walls. As expected, deviations are

stronger in the areas of separation and where the flow has subsonic speeds, as can be seen in stations E2, and E9. Separation starts at station E2, where the current solution predicted a higher backflow than the references. Station E9 is close to the end of the ramp and it seems to be the most problematic region. Other numerical studies also struggle there. Grilli et al.'s wall resolved LES can capture the slope at the wall accurately, but not so much for the rest of the boundary layer. The current prediction is close to reference [70] at station E12, which is at the attached flow region after the ramp. The main problem of the current results is the prediction of a larger separation bubble.

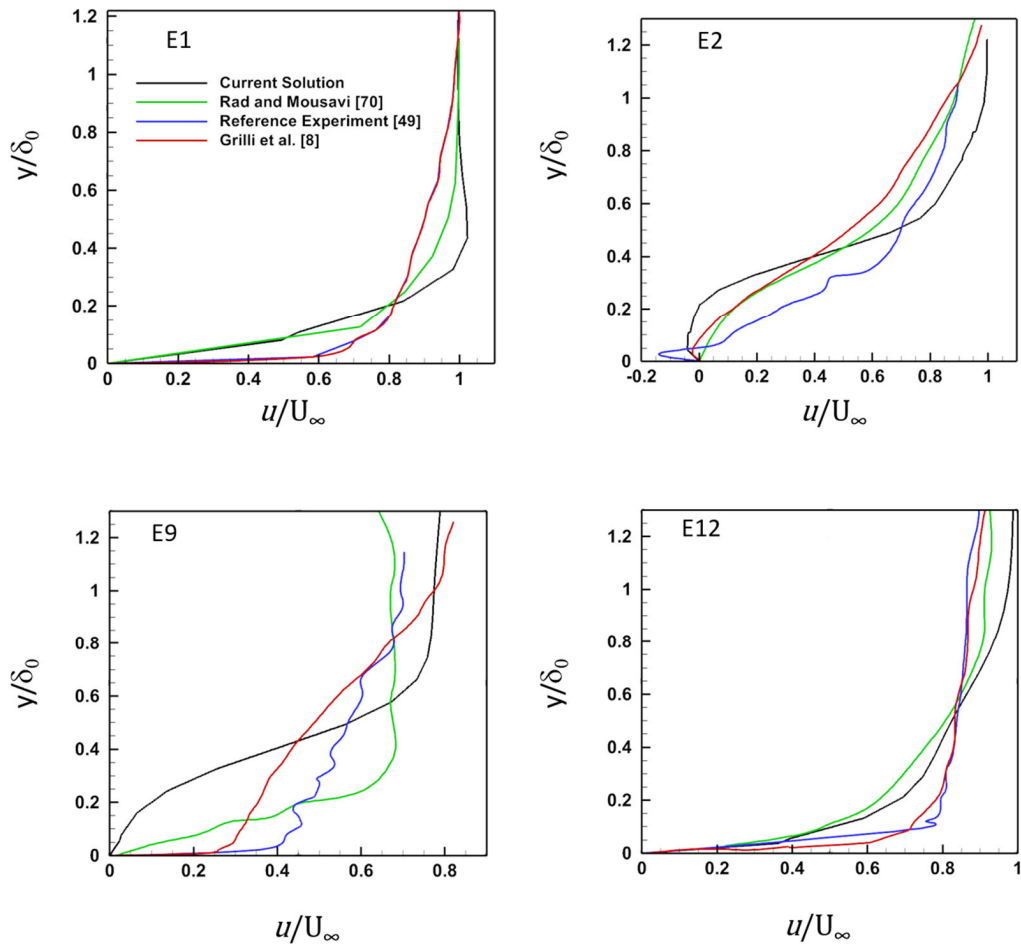


Figure 3.10. Velocity profiles at the different locations (averaged in time and in spanwise direction)

When the boundary layer is calculated thinner, the pressure distribution tends to become steeper at the separation point [40], [41]. This is the case for the current simulation, for example at station E1, resulting in an earlier and steeper pressure rise, as can be seen in Figure 3.9. The reason why the pressure distribution did not agree with the experimental solution before the ramp where the separation started is thought to be the error in predicting the incoming boundary layer thickness.

The spanwise averaged instantaneous Mach contours are shown in Figure 3.11, where the main flow features of the SWBLI can be seen. It can be seen that the separation shock starts the separation of the flow. A shear layer is formed just above the separation zone until the flow is reattached. Reattachment shock can be observed and it interacts with the separation shock upstream of the ramp. Expansion waves are formed at the end of the ramp and the flow becomes supersonic again.

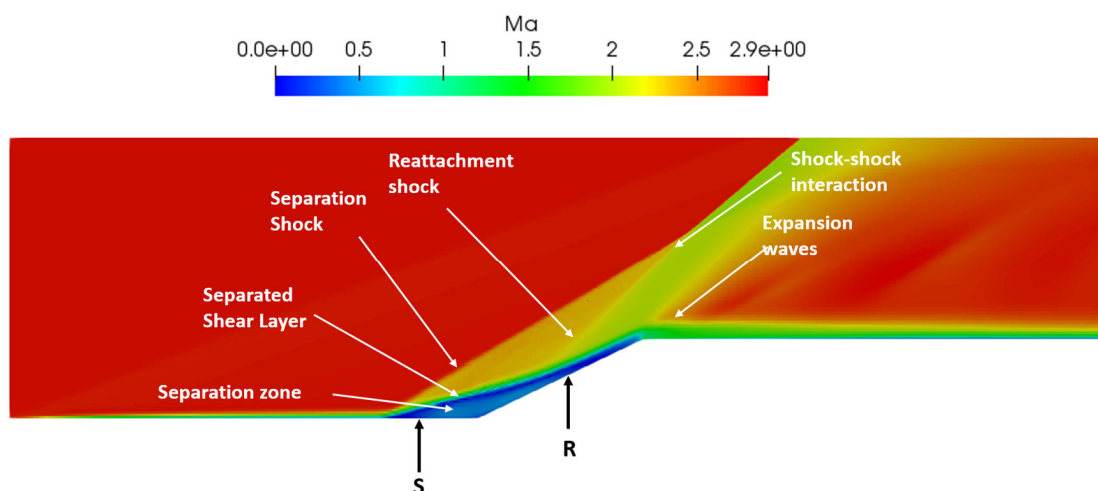


Figure 3.11. The spanwise averaged instantaneous Mach contours (S – separation, R - reattachment)

The spanwise averaged instantaneous Mach number distribution along the $y/\delta_0=5$ horizontal plane is shown in Figure 3.12. It can be seen that separation shock caused a sharp fall of the Mach number. The reattachment shock and shocklets caused a less steep fall as they are series of shockwaves. The expansion process is due to a series of expansion waves.

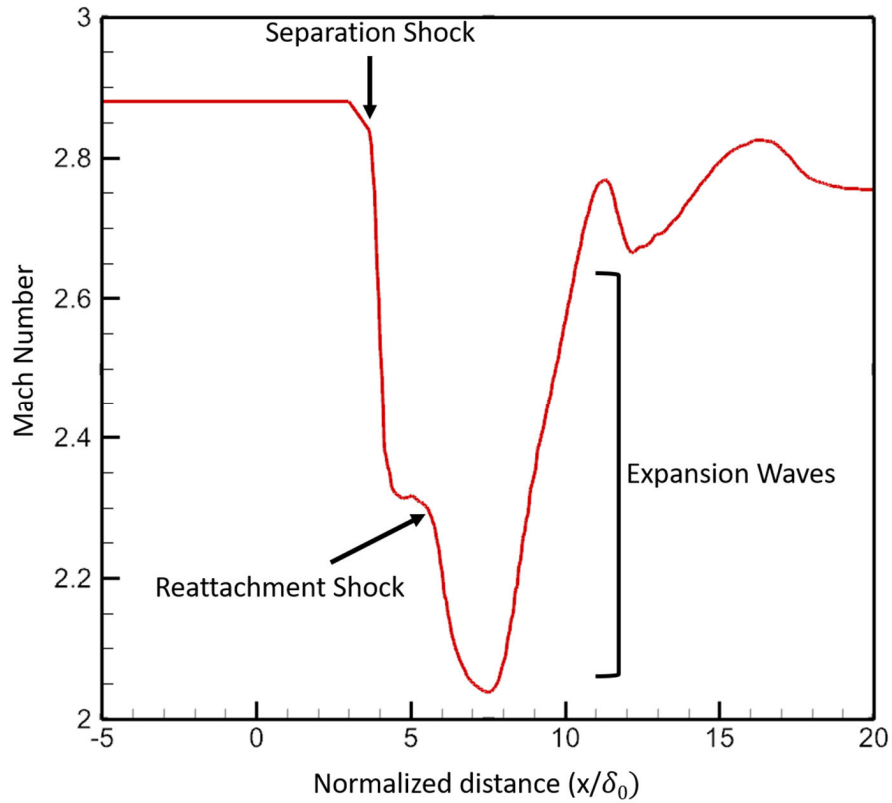
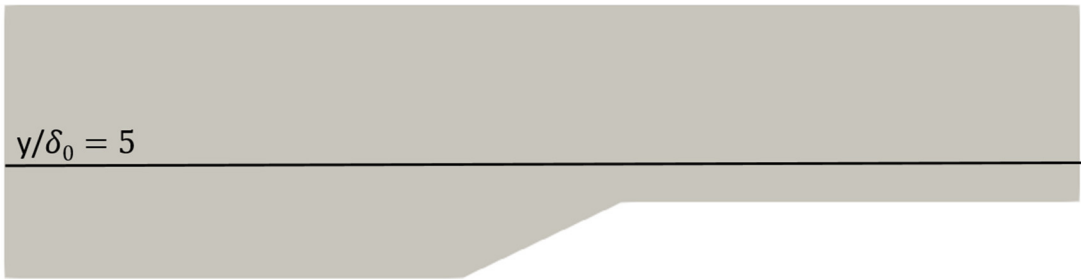


Figure 3.12. The spanwise averaged instantaneous Mach number distribution along the $y/\delta_0=5$ horizontal plane

The numerical Schlieren of the current solution is compared with the experiment of Zheltovodov [49] in Figure 3.13. The location of the separation shock agrees well with the experimental work. Separated shear layer is a bit thinner for the current simulation, which is due to the thinner incoming boundary layer. Reattachment shock position and angle are different than the experiment which implies that the reattachment location deviates from the experimental position. Expansion waves are visible for both pictures

and located at the end of the ramp. Qualitatively speaking the solutions are in agreement with the experimental results.

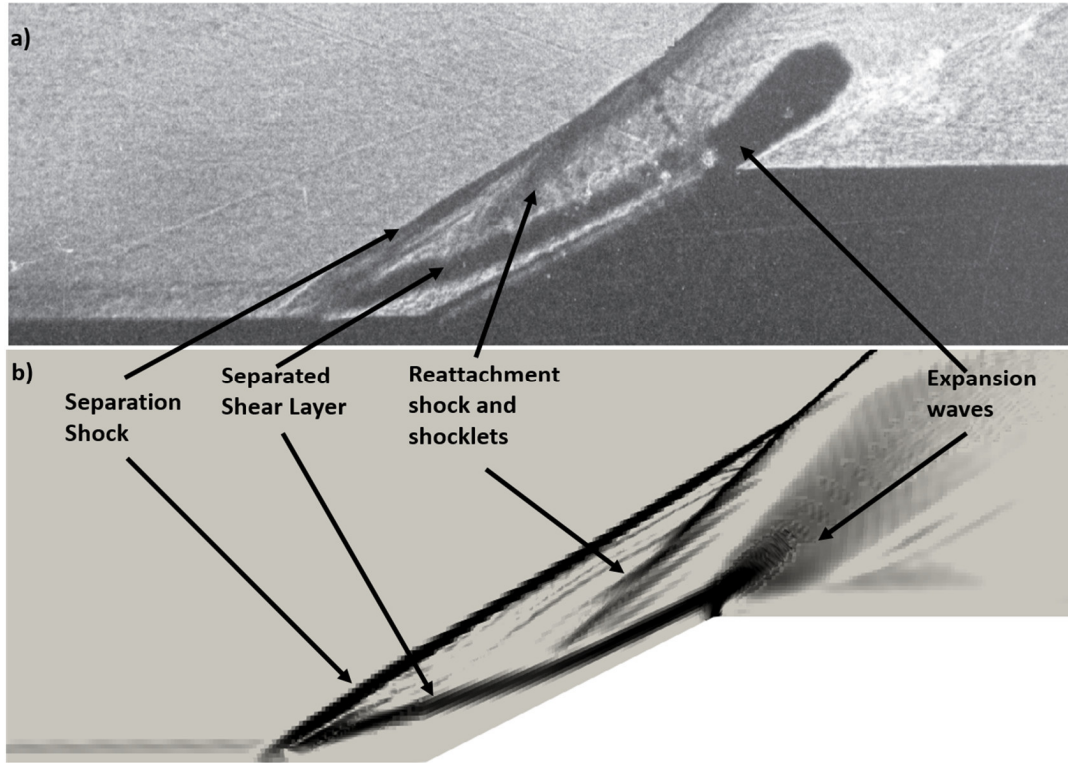


Figure 3.13. Schlieren photograph of Zheltovodov [49] (a) and numerical Schlieren (b) of the current simulation

Instantaneous wall shear stress contours are given in Figure 3.14. Circulation zones due to the Görtler vortices can be seen just after the reattachment region. It can be stated that a pair of counter rotating streamwise vortices are formed. These pair of vortices are observed to be asymmetric in the z direction, which is to be expected. They cause disturbances in the spanwise direction in the form of fluctuations in the flow field features. Taking this into account, it can be stated that the flow is highly three-dimensional over the compression ramp and after the ramp. The widths of the vortices are about $2\delta_0$ in the spanwise direction. It can be stated that the use of symmetry boundary conditions for the sidewalls and the length of the domain in the spanwise direction are adequate considering that each of the vortices in the pair is present as they were in refs. [8], [48], [49]. Although structures that have larger scales

cannot be observed by using this width, there is no indication of such structures in the experimental results [49].

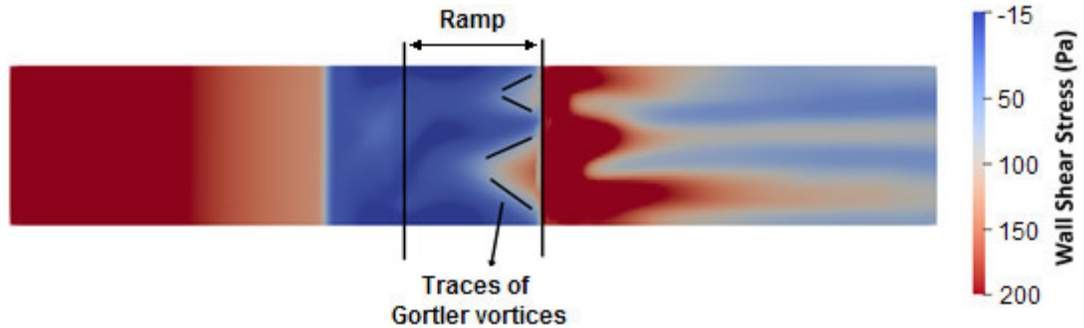


Figure 3.14. Contours of instantaneous wall shear stress in the x direction

Instantaneous streamwise vorticity contours on the wall is given in Figure 3.15(a), where blue color denotes positive rotation and red color denotes negative rotation. The pairs of vortices discussed above are also observable in this figure. It can be seen that they are asymmetric as in the case of Figure 3.14, and two pairs are present. It can also be stated that the vorticity is amplified after the shock. Instantaneous wall shear contours in the z direction is presented in Figure 3.15(b). Again, it can be seen that different zones with sign changes are present. The vortices change size and strength in time and this behavior was also observable from the wall pressure signals that are taken from different locations in the spanwise direction. It can be stated that the peak values of the pressure signals at the two ends of the domain in the spanwise direction have a clear phase shift.. It should be noted that since symmetry boundary condition was used for the side planes the number of pair vortices might be affected because this boundary condition lets no flow to come in or go out. However the number of the vortices were found same as Grilli et al [8], so the downside of using such a boundary condition might be eliminated by choosing a suitable width as it was in our case.

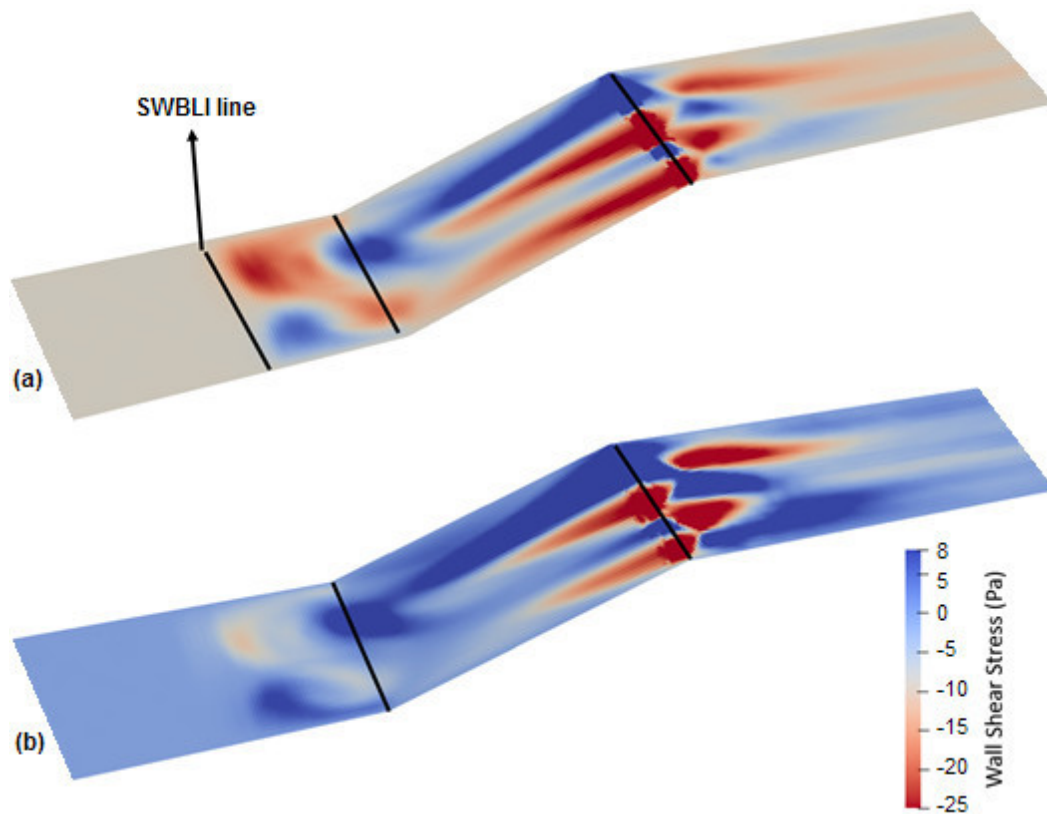


Figure 3.15. Instantaneous contours of streamwise vorticity (a) and wall shear stress in the z direction (b)

Average (in time and in spanwise direction) skin friction coefficient distribution along the wall is given in Figure 3.16. The separation point is in agreement with the experimental values and Grilli et al.'s numerical work. Grilli et al. stated that separation started at $x/\delta_0 = -3.98$, and in this work it is seen at $x/\delta_0 = -3.88$. However, there is a discrepancy for the reattachment point, which was stated by Grilli et al. [8] to be at $x/\delta_0 = 2.00$ and in this study it is found to be $x/\delta_0 = 2.78$. This should be related to the fact that in the separation region wall models experience difficulties predicting the flow correctly. Also, incoming boundary layer was calculated thinner than that given in the references. Although the trends of the skin friction have similarities at the peak and low locations, there are considerable differences in the magnitudes.

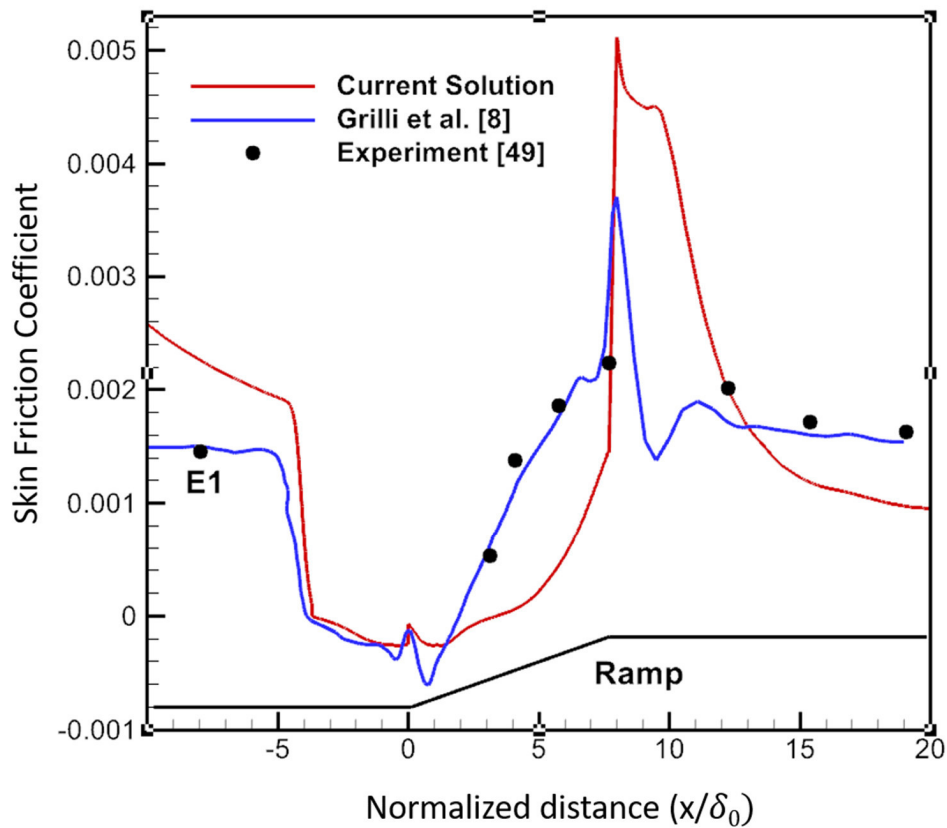


Figure 3.16. Average skin friction coefficient along the wall

The unsteadiness of the system is investigated by taking Fast Fourier Transform (FFT) of wall pressure signals. Figure 3.17 shows the time history of the wall pressures taken at stations E1 and E2 and their frequency content. It is seen that root mean squares of the pressure fluctuations are different at these stations as they are around 15 Pa for station E1 and 770 Pa for station E2. Their frequency contents are also different. It can be seen that at station E1 dominant frequencies (which have highest amplitudes) are on the order of 10^5 to 10^6 whereas at station E2 dominant frequencies are on the order of 10^3 . This behavior was observed also in several previous studies and reported as the low frequency component of the unsteadiness around the shock foot [3], [6], [8], [11]. The low frequency component of the signals were caused by the low frequency motion of the shock system.

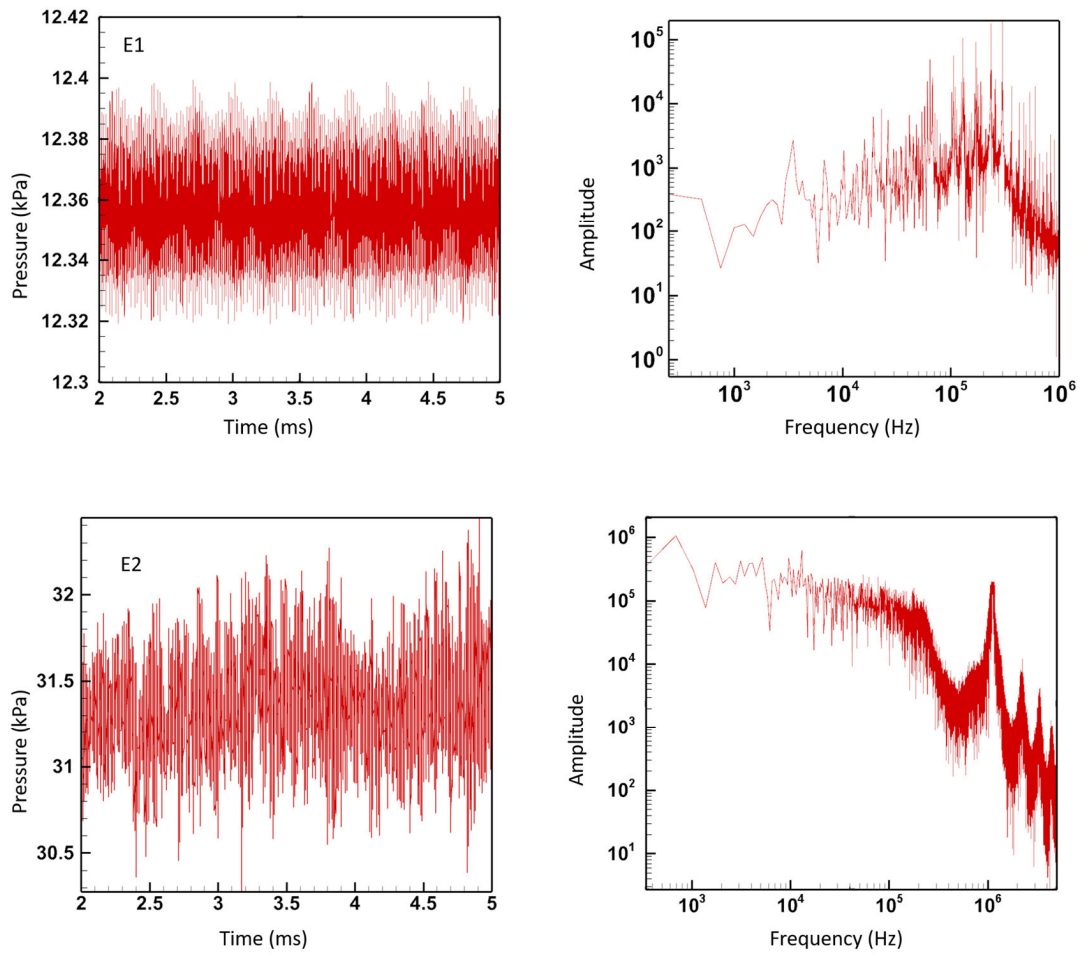


Figure 3.17. Pressure signals and their FFTs for stations E1 (top) and E2 (bottom)

CHAPTER 4

SIMULATIONS OF CASE II: SHOCK IMPINGING ON A WALL

In this chapter, a shock generated by a compression-expansion ramp impinges on a wall, which is a case studied before experimentally by Campo and Eaton [9]. To the best knowledge of the author, this case has not been studied numerically in the literature yet. The geometry of the problem can be seen in Figure 4.1 and the reference values used by Campo and Eaton [9] are summarized in Table 4.1.

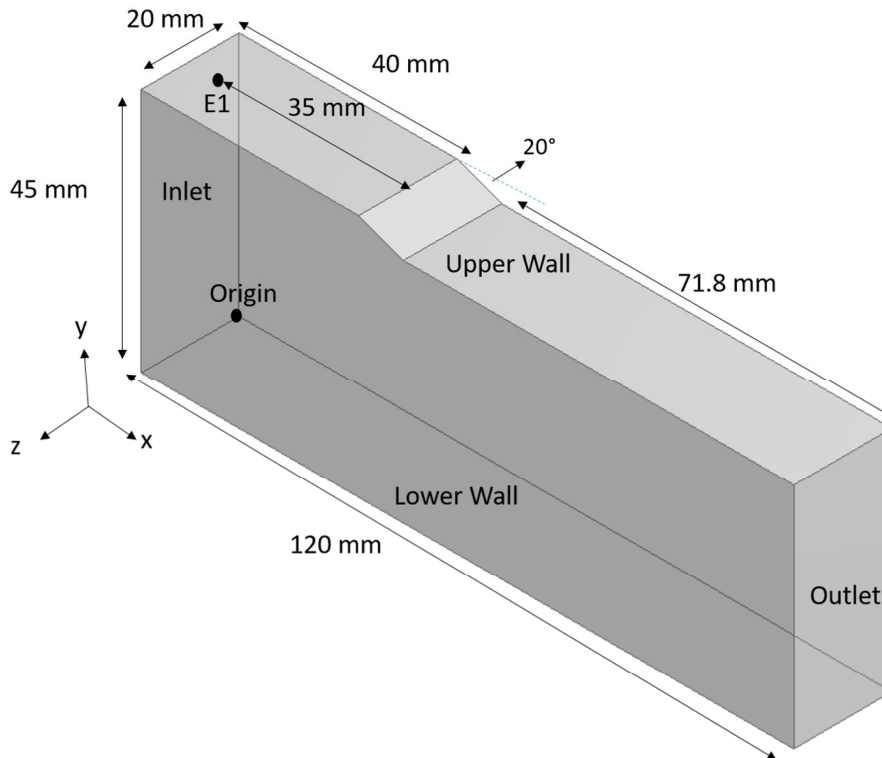


Figure 4.1. Problem geometry and boundary conditions for Case II: Shock impinging on a wall

Origin of the coordinate system is positioned at the lower left corner of the inlet. The ramp has an angle of 20° , height of 3 mm ($0.56\delta_0$) and the domain has the extents of $8.33\delta_0 \times 3.7\delta_0 \times 22.2\delta_0$ (or 45 mm \times 20 mm \times 120 mm) for the height, width and

length, where $\delta_0 = 5.4$ mm is the boundary layer thickness measured by Campo and Eaton [9] at station E1, which is located at 35 mm ($6.5\delta_0$) upstream of the start of the ramp (see Figure 4.1). There is an inflow boundary 40 mm ($7.4\delta_0$) upstream of the start of the ramp and an outflow boundary 71.8 mm ($13.3\delta_0$) downstream of the end of the ramp. The bottom boundary and the upper boundary are no-slip walls. Side walls are treated as symmetry planes. The computational domain explained above differs from the experimental geometry of Campo and Eaton [9], where the width was twice as large (40 mm) with the sidewalls being the walls of the wind tunnel. Also in the experimental geometry there was a longer inlet section, for which details are not available. To overcome this situation, boundary layer thickness and velocity profile that is measured by Campo and Eaton [9] is used as the inlet boundary condition and the inlet section will be shortened. Compared to Case I that was studied in the previous chapter, this case has a ramp height ($0.56\delta_0$) smaller than the incoming boundary layer thickness, which is one of the most important differences between these two cases. The smaller height of the ramp is expected to cause a weaker interaction for the upper wall. Thus, the main characteristics of the SWBLI flow such as three dimensionality and unsteadiness might be affected and might be harder to identify.

Table 4.1. Reference values for Case II [9]

Mach number	2.05
Boundary layer thickness at station E1, δ_0 (mm)	5.4
Reynolds number based on the boundary layer thickness at E1	188000
Free-stream speed (m/s)	530
Free-stream pressure (Pa)	30000
Free-stream temperature (K)	165

Pressure, temperature and velocity data are gathered from 28 stations of which 15 was on the upper wall and 13 was on the lower wall. Stations are named as “E-#” for the upper wall and “L-#” for the lower wall. Locations of these stations are given in Table 4.2.

Table 4.2. Locations of stations where data were taken.

Station(Upper Wall)	Location (x/δ_0)	Station(Lower Wall)	Location(x/δ_0)
E1	1.0	L1	1.0
E2	2.0	L2	2.0
E3	4.0	L3	4.0
E4	4.5	L4	9.0
E5	5.0	L5	9.5
E6	5.5	L6	10.0
E7	6.0	L7	10.5
E8	6.5	L8	11.0
E9	7.0	L9	11.5
E10	7.5	L10	12.0
E11	8.0	L11	16.0
E12	8.5	L12	18.0
E13	9.0	L13	20.0
E14	12.0		
E15	16.0		

4.1. Computational Model

The settings for OpenFOAM are the same as Case I in terms of solver, numerical scheme, LES and wall model preferences, which were described in section 3.1. This case differs from Case I in the following ways:

- Time step is taken as 0.25×10^{-7} s before AMR and 1×10^{-7} s after AMR.
- Both upper and lower boundaries are treated as walls, i.e. no slip boundary condition is applied.
- The velocity profile shown in Figure 4.2 is defined at the inlet boundary by using the “timeVaryingMappedFixedValue” with the off-set option. This off-set option allows user to define a velocity profile from a distance from the

inlet. For this case off-set was set to 5 mm where the velocity profile is measured by Campo and Eaton [9] at the middle plane ($z/\delta_0=3.89$).

- Simulations are done for 1.5×10^{-3} seconds for the first transient to finish and then AMR is applied, after which the simulations are ran for another 1.5×10^{-3} seconds for the second transient to finish. Next, simulations are continued for another 4×10^{-3} seconds to gather data, making the total simulation time 7×10^{-3} seconds. This process takes about 5 clock days by using 60 cores of TRUBA HPC system of TÜBİTAK ULAKBİM High Performance and Grid Computing Center.

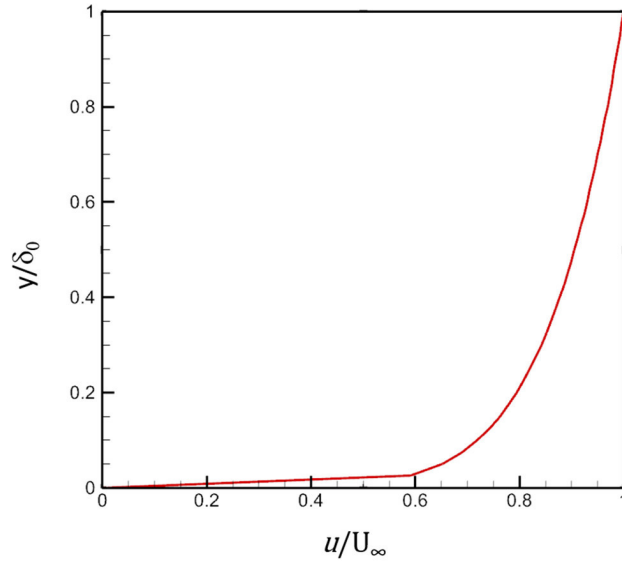


Figure 4.2. Velocity profile specified at the inlet boundary of Case II

Since the Reynolds number based on the reference boundary layer thickness does not have an order of magnitude difference from Case I, mesh settings in terms of Δx^+ , y^+ , Δz^+ are kept similar to the Medium mesh used in Case I. The mesh details (before adaptation) for this case are given in Table 4.3, which corresponds to a mesh of 8.5M cells.

Table 4.3. Mesh details for case II (before adaptation)

Number of elements in x, y and z directions	Spacings in wall units at E1 (Δx^+ , y^+ , Δz^+)
640 x 180 x 72	150, 200, 150

4.2. Results and Discussion

Solutions are started with the 8.5M mesh described above and to capture the shock waves better AMR based on pressure gradient is applied after initial transient is over. The AMR procedure is the same as the one discussed in section 3.2. The grid obtained after the AMR can be seen in Figure 4.3. The cells near the shock waves and expansion waves are refined as can be seen in Figure 4.3. The pressure gradient interval used in the refinement is from 7×10^6 to 2×10^7 Pa/m. Mesh is refined 2 times with a refinement factor of 2, i.e. each refined hexahedral cell is divided into 8 cells. With the use of AMR, the number of cells of the grid rose from 8.5M to 19.8M. This grid is used to obtain all the results of this chapter. Appropriateness of the adapted mesh is checked using the y^+ contours as well as LES IQ and M index measures to get results similar to Case I.

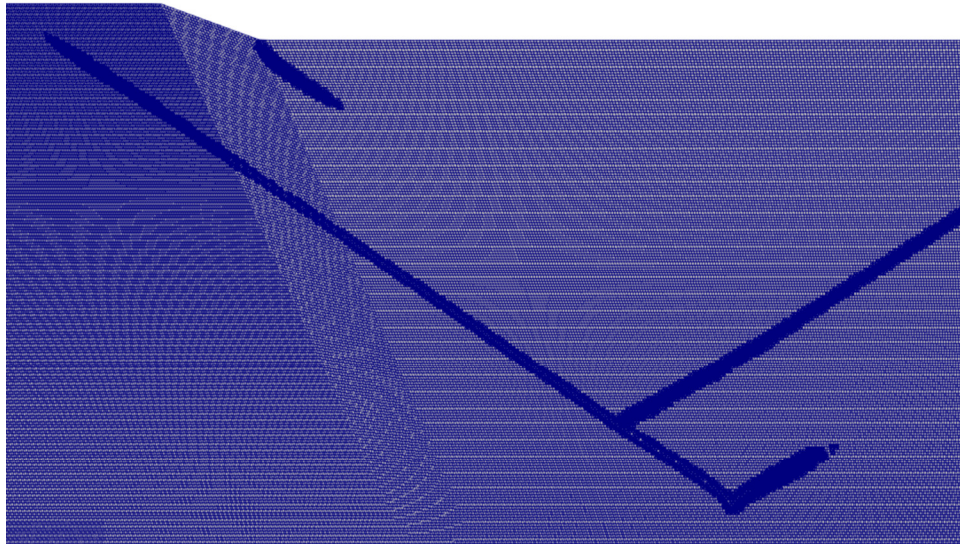


Figure 4.3. Zoomed in view of the grid after the AMR process for Case II

In Figure 4.4, instantaneous contours of the Mach number at the mid-plane in spanwise direction is presented. The flow is separated from both the upper and the lower walls by the effect of the shock waves. For the upper wall, separation shock, which is an impinging shock for the bottom wall, interacted with the boundary layer. A separated shear layer and separation zone can be observed at the upper wall. Unlike case I, the reattachment shock is not observable, due to the lower ramp height. The expansion waves are formed just after the ramp. Separation shock of the ramp impinges the lower wall and disturbs the incoming boundary layer, causing separation. A weaker separation shock is also present for the lower wall where the separation begins, causing further shock-shock interactions. A reflecting shock takes place where the impinging shock and separation shock interacts. Flow then reattaches the bottom wall before reaching the outlet.

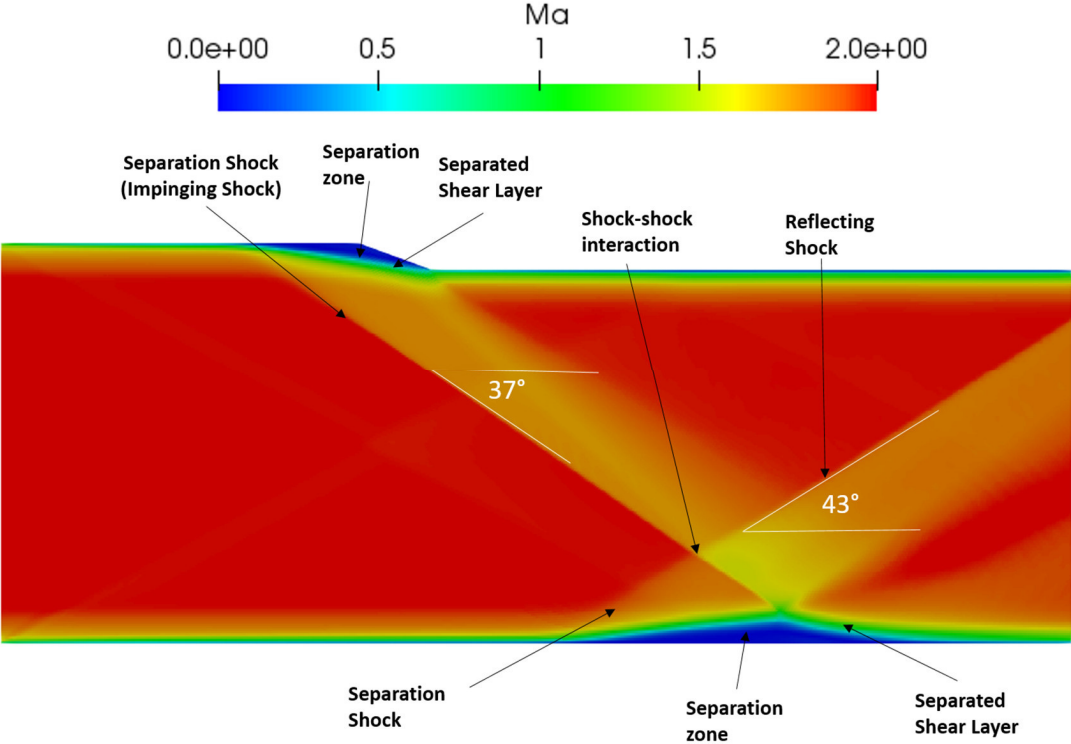


Figure 4.4. Instantaneous contours of the Mach number taken from the mid-plane for Case II

Variation of the instantaneous Mach number at the mid-plane are given in Figure 4.5 along lines $y/\delta_0=1.5$ and $y/\delta_0=7$. The separation shock of the upper wall caused a higher Ma number fall compared to the one for the lower wall. Reattachment shock, which is not very clear in Figure 4.4, is observable here, and it can be stated that it is very weak. It can be seen that Ma number drop due to the impinging shock is captured sharply. For the lower wall, combined effect of impinging shock and separation shock caused a higher drop in Mach number than the upper wall.

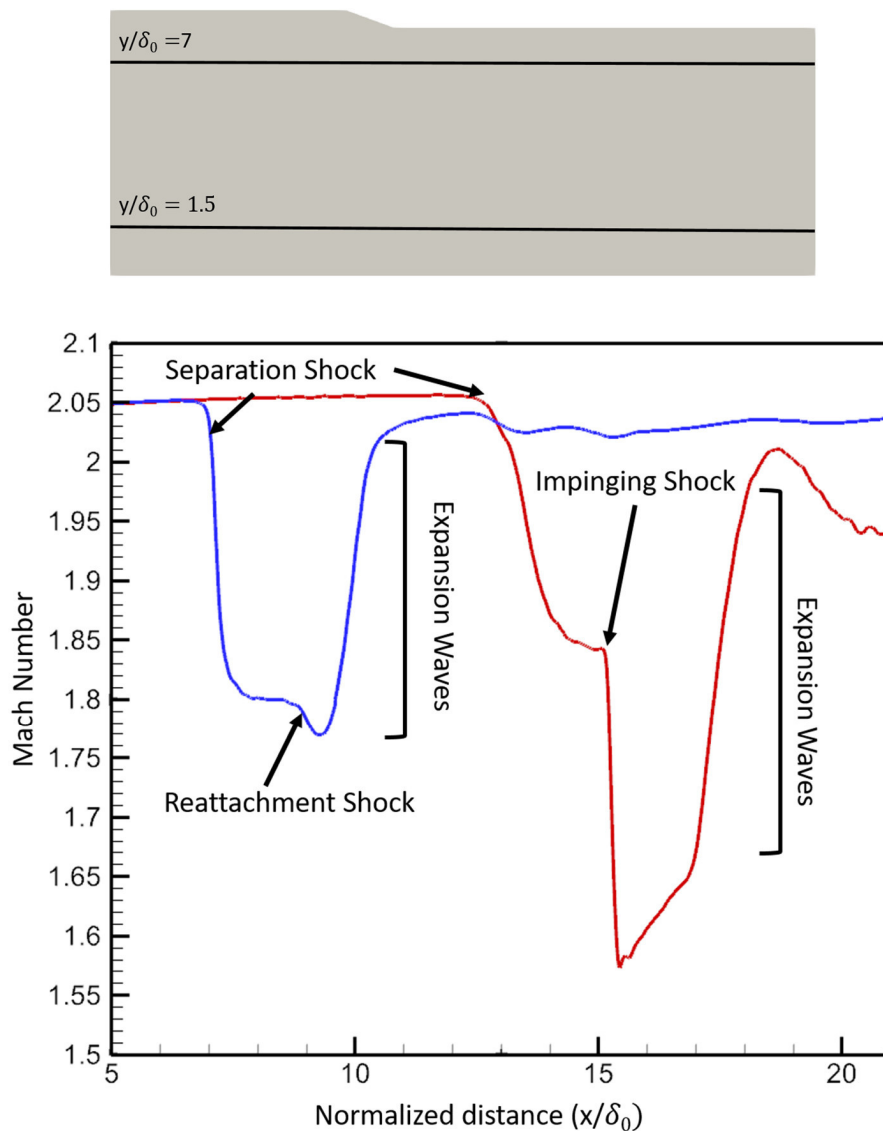


Figure 4.5. Instantaneous Mach number distribution at the mid-plane along lines $y/\delta_0=1.5$ (red), and $y/\delta_0=7.5$ (blue)

Comparison of the flow field with the PIV measurements of Campo and Eaton [9], which are taken from the zones that are highlighted in Figure 4.6 can be seen in Figure 4.7 and in Figure 4.8.

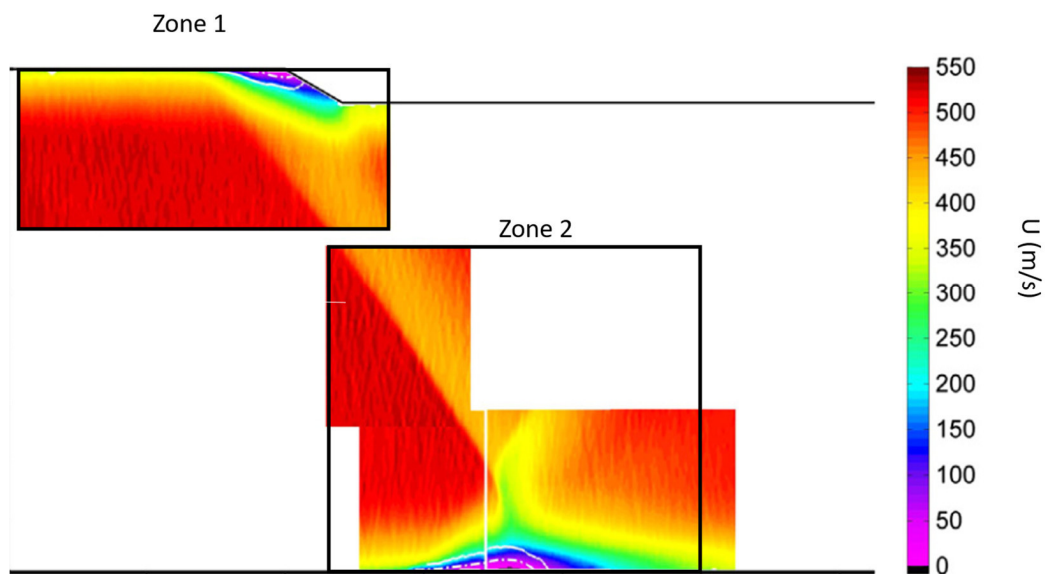


Figure 4.6. The two zones of Campo and Eaton's [9] PIV measurements that will be used for comparison with the current study. This figure shows a plane near the mid-plane in the spanwise direction.

Figure 4.7 shows the interaction zone for the ramp at the upper wall. It can be seen that the separation shock angle is similar with the experiment. In the experiments, it is stated that the separation shock angle is between 38° to 44° , whereas for the current simulation it is calculated to be 37° .

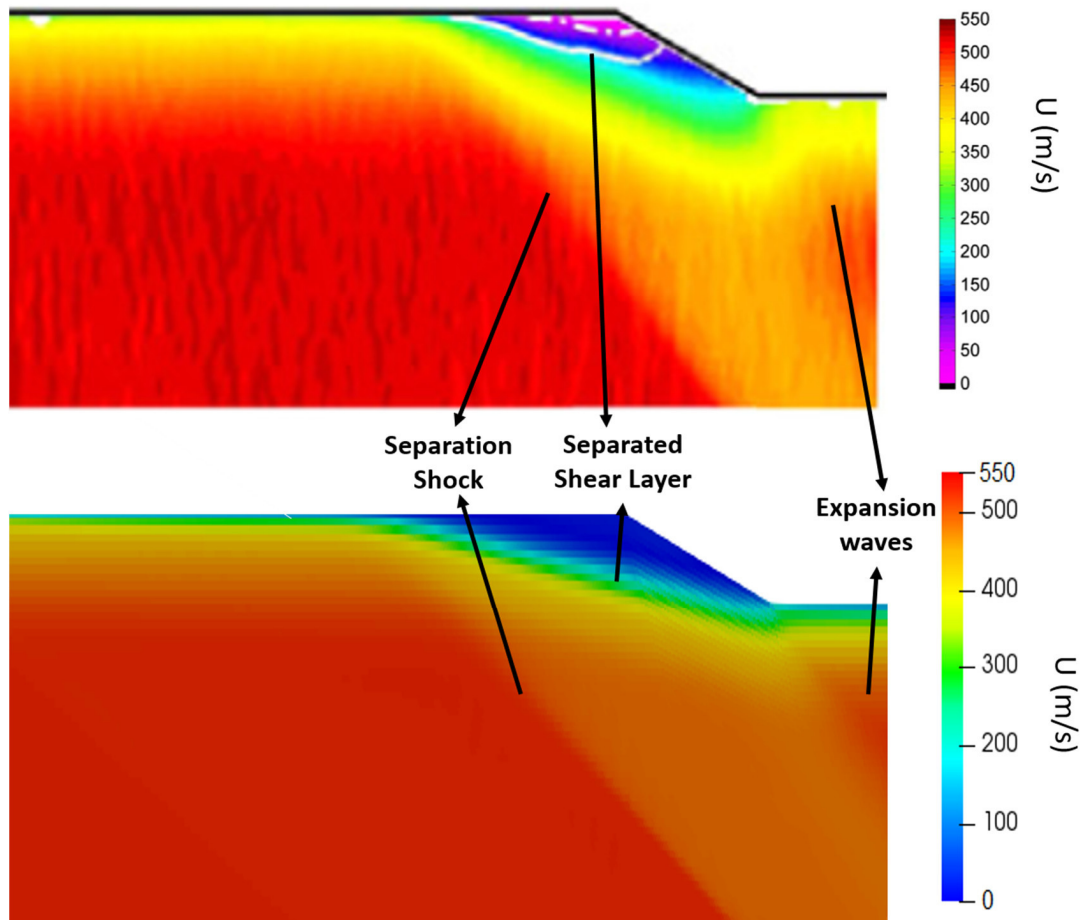


Figure 4.7. Comparison of the streamwise velocity contours near the ramp on the mid-plane of the domain (above Campo and Eaton [9] and below the current study)

Figure 4.8 shows the interaction region for the impinging shock on the incoming boundary layer. It can be stated that separation started around the same location for both cases. The position of the reflection shock took place a little lower in the y direction for the current simulation. The reflected shock angle was calculated for the experiments as 44° [9], whereas for the current simulation it is 43° . The transmitted shock has a different angle and strength from the experimental results. This shock was stronger in the experiments than for the current simulation. This caused the flow field to differ after the shock-shock interaction.

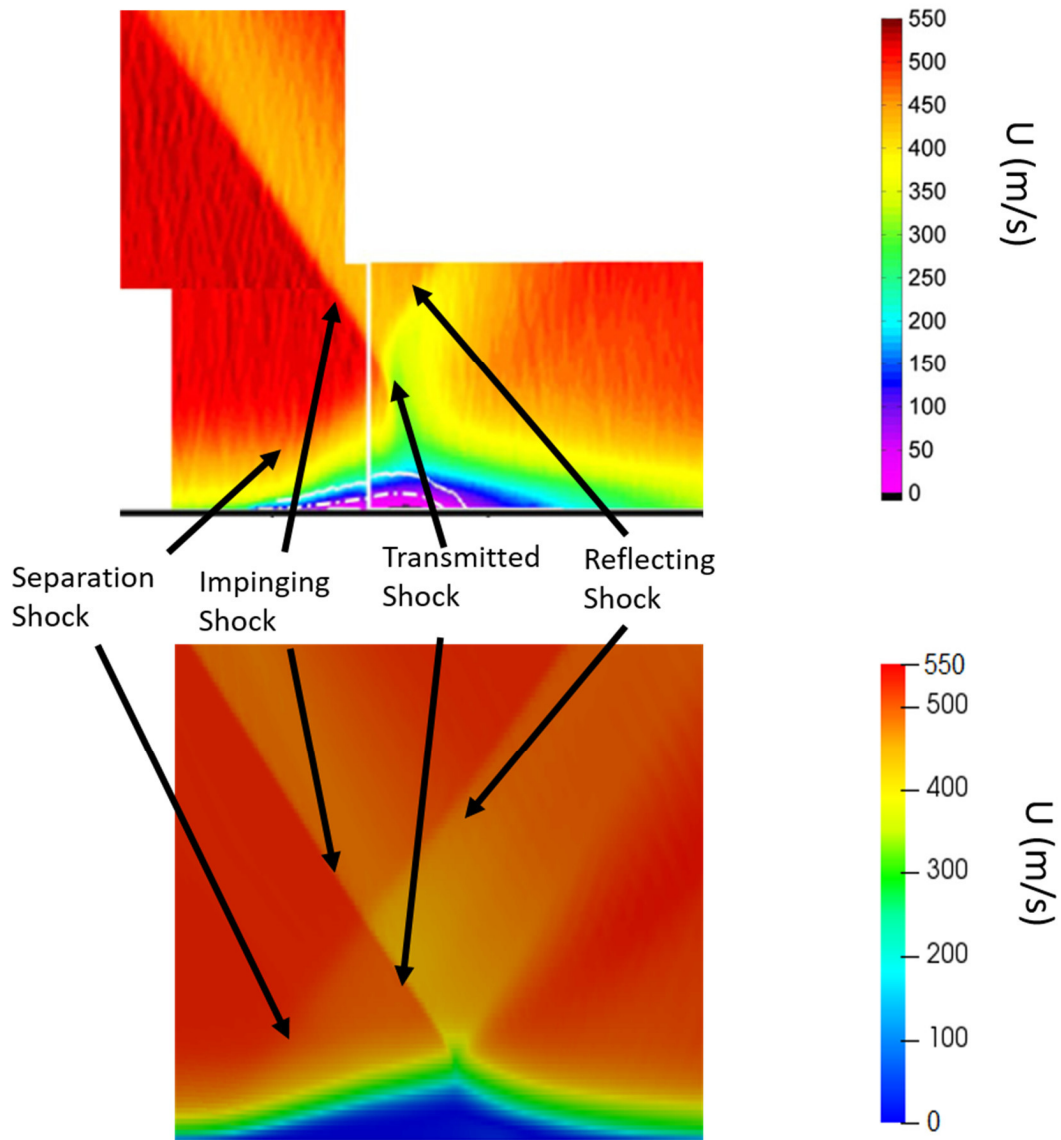


Figure 4.8. Comparison of the flow fields for the impinging shock for mean streamwise velocity at the mid-plane (above Campo and Eaton [9] and below current study)

To understand the three-dimensionality of the flow field, time averaged velocity contours in the y direction near the top and bottom walls are compared with the experimental results in Figure 4.9 and Figure 4.10. Around the top wall shown in Figure 4.9, the overall flow fields are similar. The y velocity component is near zero except inside the zone bounded by the separation shock, expansion waves and

separation zone. Velocity in the y direction increases in the areas where the free-stream velocity is altered by the shock wave and the flow is no longer unidirectional.

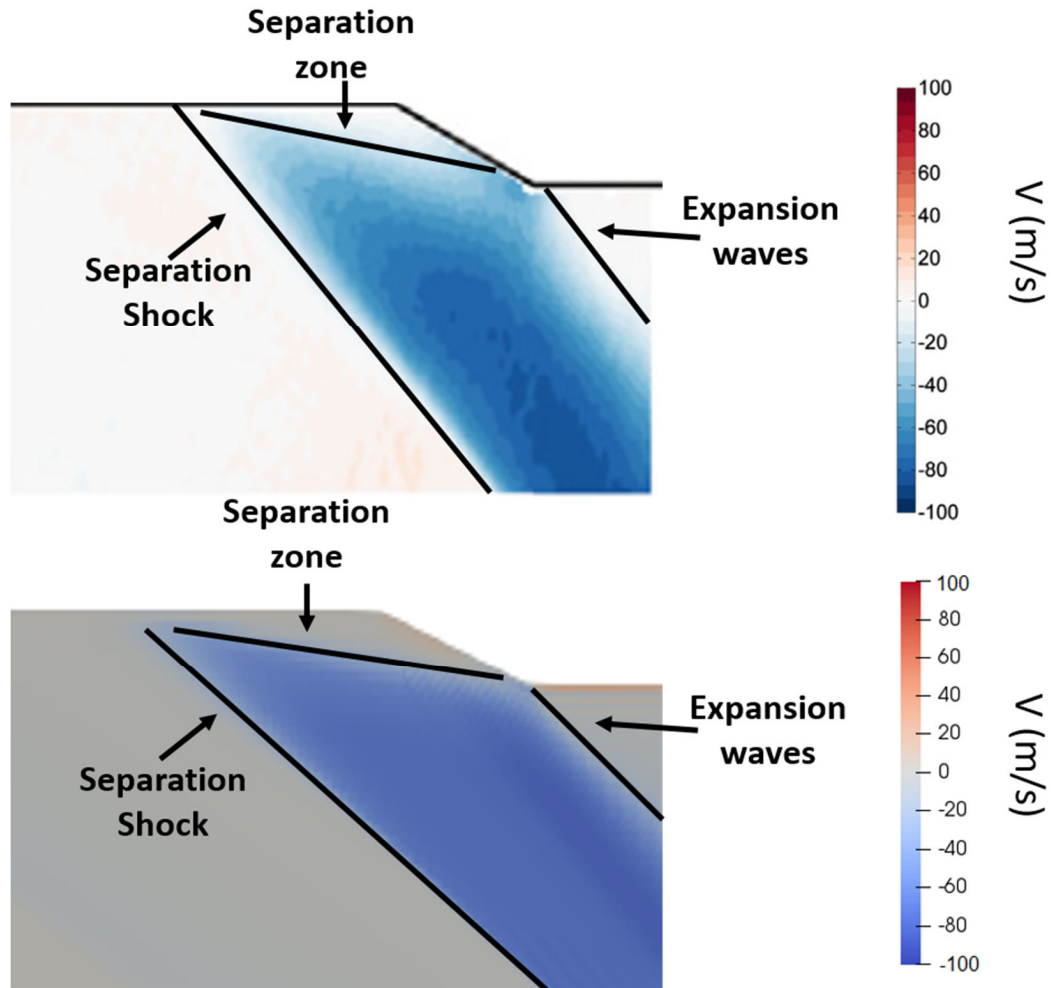


Figure 4.9. Comparison of time-averaged y velocity contours near the upper wall at the mid-plane (above Campo and Eaton [9] and below the current study)

The spanwise velocity contours around the shock impinging on the lower wall can be seen in Figure 4.10. Flow fields are similar to each other except for the zones A and B. These zones are created after the shock-shock interaction. As it is stated for the Figure 4.8, the transmitted shock is predicted weaker. After the interaction, current simulation predicts a larger zone A, and a smaller zone B, which means that the expansion waves are formed more downstream for the current simulations.

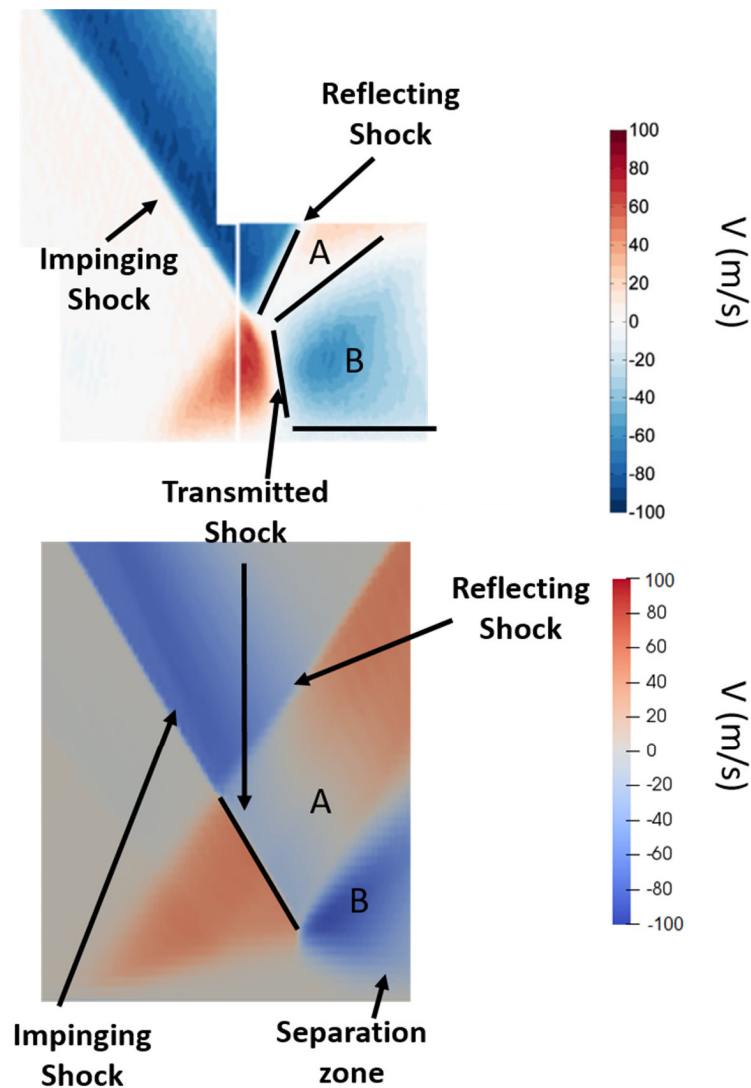


Figure 4.10. Comparison of time-averaged y velocity contours near the lower wall at the mid-plane (above Campo and Eaton [9] and below the current study)

Turbulence intensity contours for streamwise velocity are compared with the experiments in Figure 4.11. For the upper wall, current simulation predicted a higher turbulence intensity for the separation shock. Also there are differences in the separation zone, which is believed to be due to wall function usage. Other than that, the separated shear layer and downstream of the ramp is predicted fairly similar to the

experiment. For the lower wall, over-prediction on the impinging shock, which is the separation shock for the upper wall, is still present.

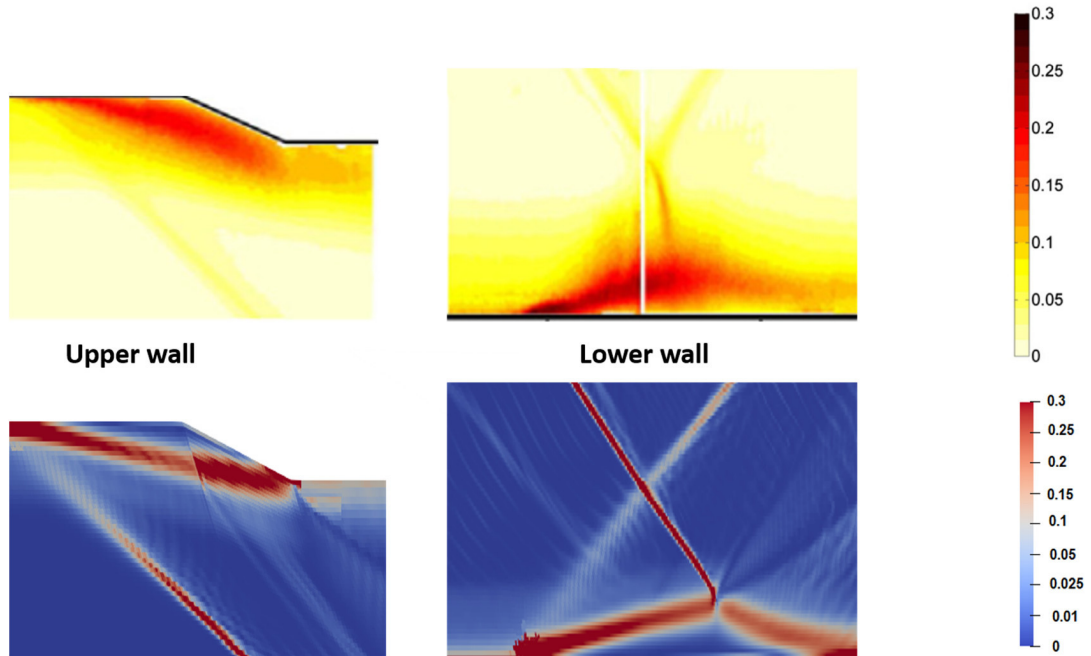


Figure 4.11. Streamwise turbulence intensity contours for both upper and lower walls at the middle plane. (Above the experiment [9], below current simulation)

Wall pressure distributions, averaged both in time and spanwise direction, are given in Figure 4.12. There is no data in reference [9] to compare these. For the upper wall, the pressure started to rise when the separation shock interacted with the boundary layer. The second peak of the pressure distribution on the upper wall corresponds to the ramp itself. For the lower wall, impinging shock caused the separation and the separation shock caused the pressure rise. Since there is no ramp at lower wall, pressure makes a single peak.

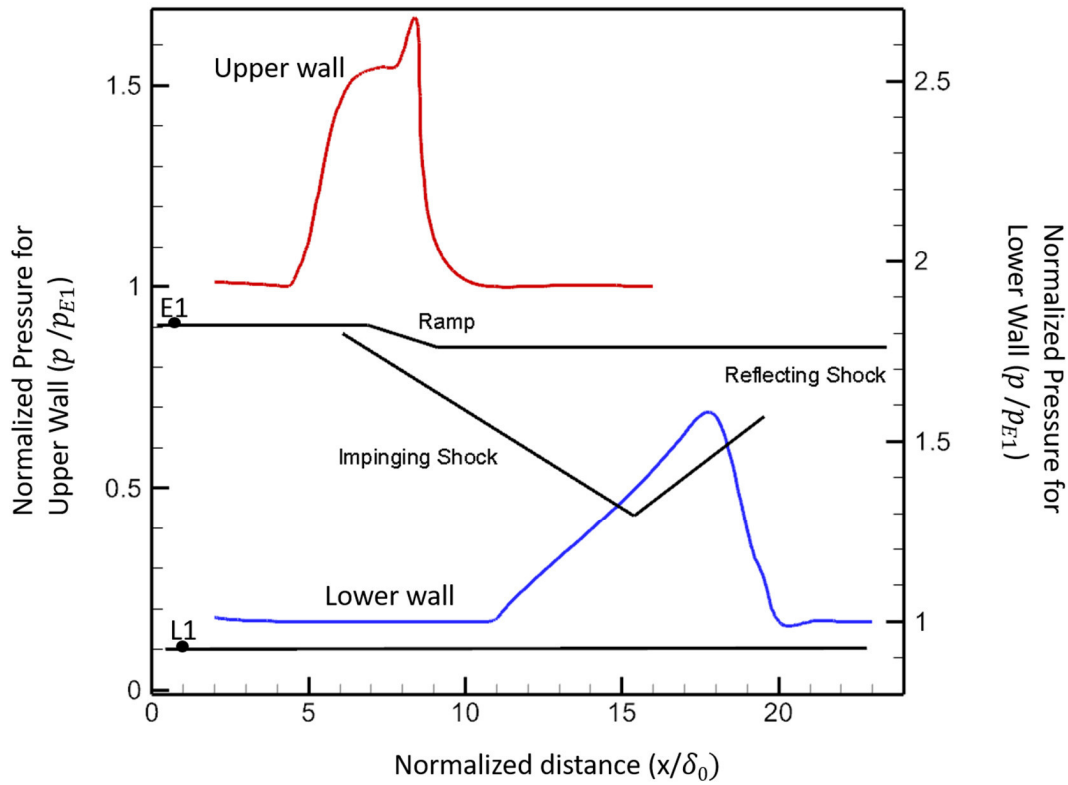


Figure 4.12. Pressure distributions on the upper and lower walls of Case II

Variation of the skin friction coefficient on the upper and lower walls can be seen in Figure 4.13. Again there is no data in the reference experiment for this. The calculated separation and reattachment points for the upper wall are $x/\delta_0=5.79$ and $x/\delta_0=8.25$, respectively, whereas in the experiment they were $x/\delta_0=5.73$ and $x/\delta_0=5.73$ (data is digitized from the x velocity contour plots of [9]). Both separation and reattachment points agreed better with the experiment, compared to Case I. The reason for this is thought to be the fact that the ramp has a smaller height compared to Case I in terms of boundary layer thickness. Because of this the interaction occurred weaker and the wall function approach worked better. For the lower wall, separation and reattachment points are calculated as $x/\delta_0=12.54$ and $x/\delta_0=17.8$, respectively, whereas in the experiment they were $x/\delta_0=11.96$ and $x/\delta_0=15.75$. Separation point location is in better agreement with the experimental data than the reattachment point location, which has 13% deviation. The interaction is more complex on the lower wall as several

shock-shock and shock boundary layer interactions are present. The discrepancies in the separation and reattachment points for the lower wall might be occurred due to this higher complexity of the flow on the lower wall.

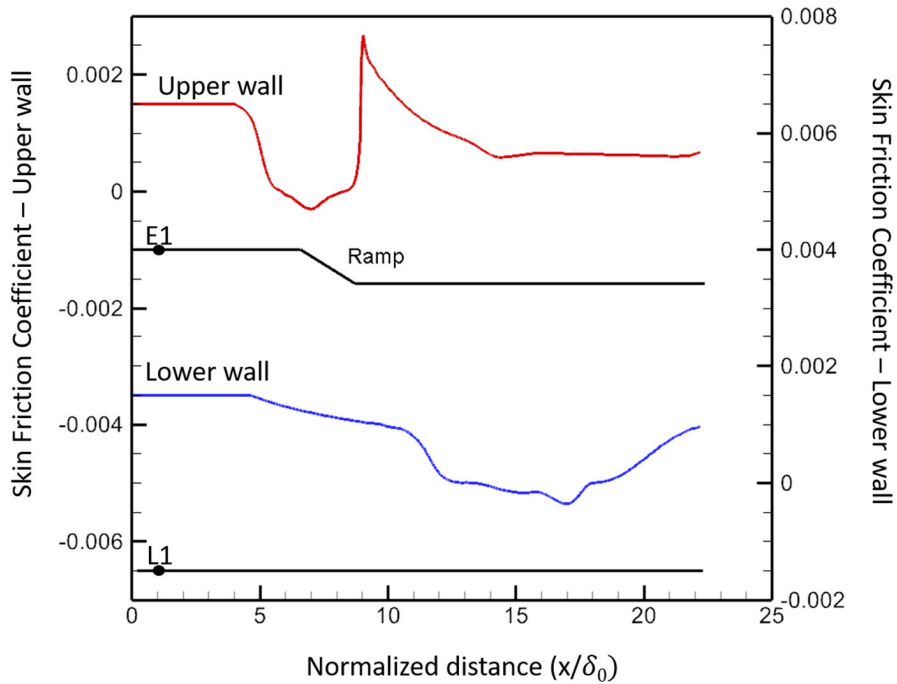


Figure 4.13. Mean skin friction coefficient distribution for upper and lower walls of Case II

The instantaneous wall shear stress contours in the streamwise direction for the upper and lower walls are presented in Figure 4.14. The flow is not disturbed in the spanwise direction on the upper wall. Three-dimensionality effects are weaker for this case when compared to Case I, where Görtler vortices were present and the flow was highly three dimensional over and after the ramp. It is believed that the smaller ramp length of this case limits the growth of the disturbances forcing the flow to remain two-dimensional. The flow is also mainly two-dimensional on the lower wall before the separation shock and becomes mildly three-dimensional after the shock. The spanwise content of the flow is amplified as the flow grows downstream.

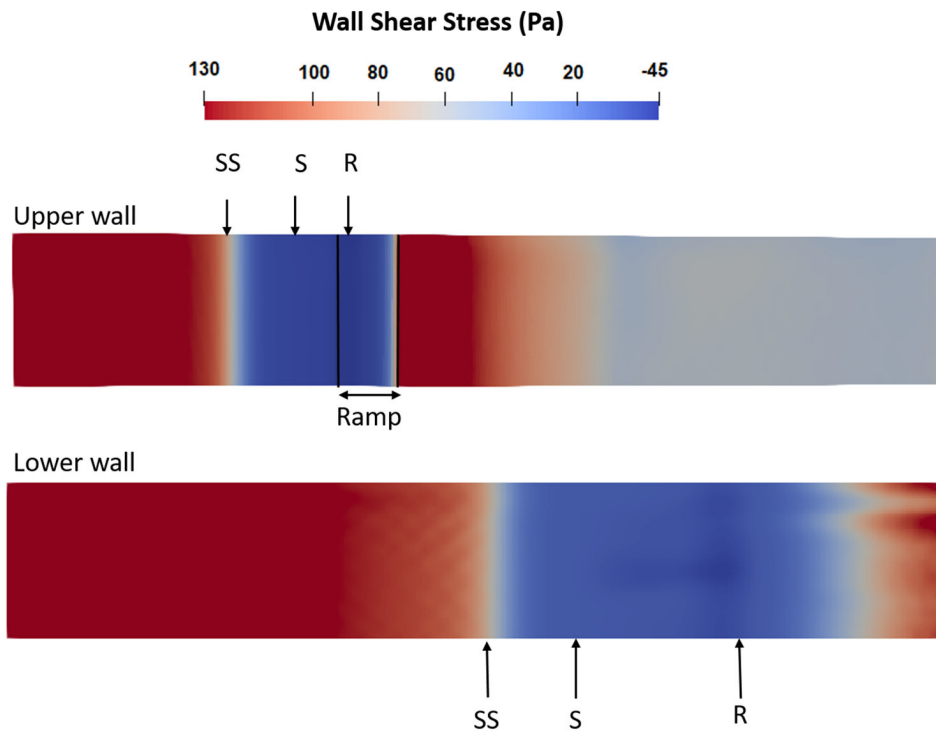


Figure 4.14. Wall shear stress contours in the x direction for Case II (S-Separation line, R-Reattachment line, SS-Separation shock)

Streamwise vorticity contours are given in Figure 4.15 where blue color means negative rotation as red color means positive rotation around x axis. It can be seen that after the shock wave, the vorticity amplitude is amplified. The downstream flow became more fluctuating in the spanwise direction as zones of counter-rotation were more visible. It can be concluded that the three dimensionality effects were present but not as severe as the Case I for both upper and lower walls.

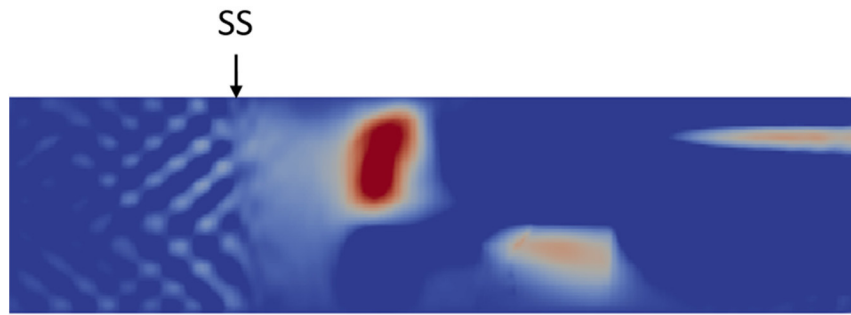


Figure 4.15. Vorticity contours in x direction for the lower wall. (SS – Separation Shock)

Time history and FFTs of pressure can be seen in Figure 4.16 for stations L1 and L10 on the lower wall. L1 is located in the undisturbed boundary layer and L10 is located in the interaction area where the impinging shock reflects from the boundary layer. The time histories showed differences in both fluctuation amplitude and behavior. Root mean squares of fluctuations are around 5 Pa for L1 and 110 Pa for L10. It can be seen that the dominant frequencies are from 10^5 to 10^6 for station L1 whereas the range is 10^4 to 10^5 for station L10. This low frequency unsteadiness is expected, as it was also present for Case I, but for this case the order of difference is lower than Case I. This difference is believed to be because of the weaker interaction strength [5]. As it was stated before, the interaction strength is weaker for this case than Case I.

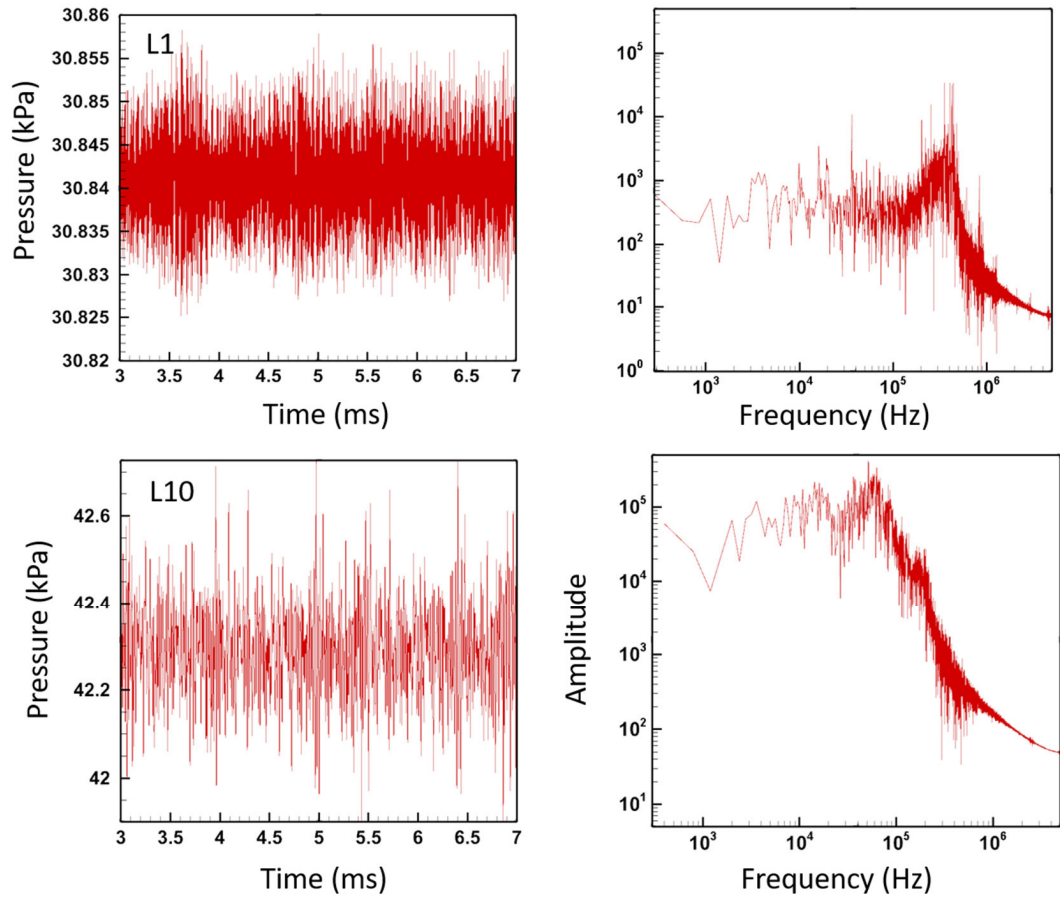


Figure 4.16. Time history of the pressure data and corresponding FFT's for station L1 (above) and L10 (below) of Case II

CHAPTER 5

SIMULATIONS ON CASE III: SHOCK IMPINGING ON A COMPRESSION-EXPANSION RAMP

In this chapter, an impinging shock on a compression-expansion ramp is be considered. The geometry of the problem can be seen in Figure 5.1. This case is derived from Case II and the reference values are kept the same, as summarized in Table 4.1, with the addition of another ramp at the bottom wall. This case is an example of shock waves interacting with concave surfaces and an incoming boundary layer. Air intakes with forebody effects and diffusers of wind tunnels experience such kind of interactions. There is no reference experimental or numerical study in the literature for this case.

Both the upper and lower wall ramps have angles of 20° and heights of 3 mm ($0.56\delta_0$), and the domain has the extents of $8.3\delta_0 \times 3.7\delta_0 \times 22.2\delta_0$ (or 45 mm \times 20 mm \times 120 mm) for the height, width and length, where $\delta_0 = 5.4$ mm is the incoming boundary layer thickness at station E1, which is 35 mm ($6.5\delta_0$) upstream of the start of the upper ramp (see Figure 5.1). There is an inflow boundary 40 mm ($7.4\delta_0$) upstream of the start of the upper ramp and an outflow boundary 71.8 mm ($13.3\delta_0$) downstream of the end of the upper ramp. The lower ramp is located 80 mm ($14.8\delta_0$) downstream of the inlet. The bottom and top boundaries are no-slip walls. Side walls are treated as symmetry planes. The origin of the geometry is taken as the lower left corner of the inlet and can be seen in Figure 5.1.

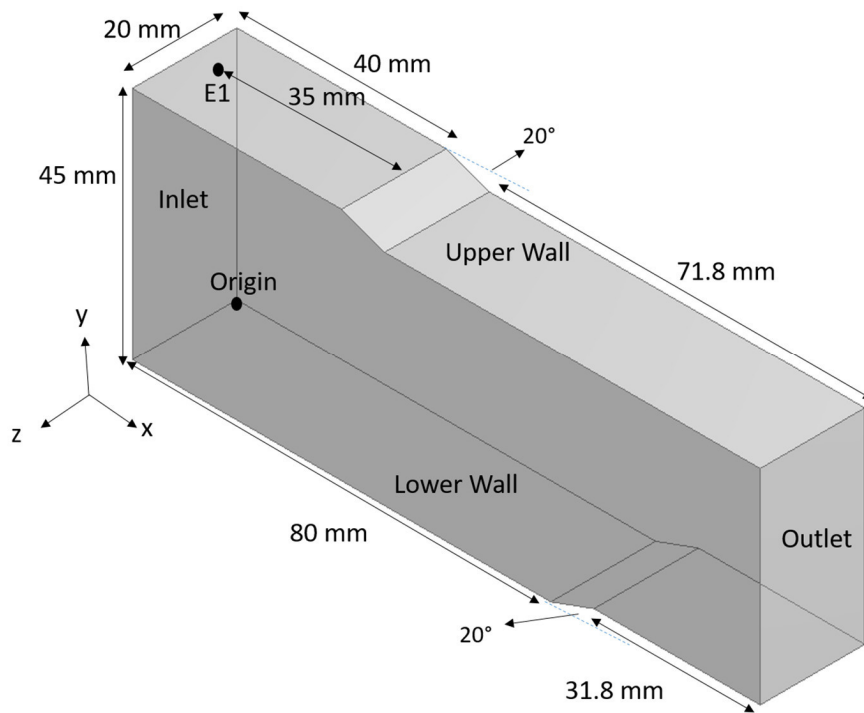


Figure 5.1. Problem geometry and boundary conditions for Case III: Impinging shock on a compression-expansion ramp

Pressure, temperature and velocity data are gathered from 28 stations of which 15 are on the upper wall (same locations as Case II) and 13 are on the lower wall. Stations are named as “E-#” for upper wall and “L-#” for lower wall. Locations of these stations are given in Table 5.1.

Table 5.1. Locations of stations where data are gathered for Case III

Station (Upper Wall)	Location (x/δ_0)	Station (Lower Wall)	Location (x/δ_0)
E1	1.0	L1	1.0
E2	2.0	L2	2.0
E3	4.0	L3	10.0
E4	4.5	L4	11.0
E5	5.0	L5	12.0
E6	5.5	L6	13.0
E7	6.0	L7	14.0
E8	6.5	L8	15.0
E9	7.0	L9	15.5
E10	7.5	L10	16.0
E11	8.0	L11	16.5
E12	8.5	L12	17.0
E13	9.0	L13	20.0
E14	12.0		
E15	16.0		

5.1. Computational Model

For this case the settings for the OpenFOAM are the same as Case II in terms of solver, boundary conditions, numerical scheme, LES and wall model preferences, which were described in Section 4.1. Simulations were done for 2×10^{-3} seconds for the first transient to finish and then AMR is applied. After that the simulations are ran for another 2×10^{-3} seconds for the second transient state to finish. Next, simulations are continued for 4×10^{-3} more seconds to gather data. Mesh details are kept as same as the Case II, as given in Table 4.3. The simulations were run at the cluster of TRUBA HPC system of TÜBİTAK ULAKBİM High Performance and Grid Computing Center. The whole process that is described above was generally completed in about 7 clock days with 60 cores.

5.2. Results and Discussion

8.5M mesh described in Table 4.3 is refined with the AMR process after the initial transient is over to capture the shock waves better. The AMR details are the same as

Case II. The number of cells rose from 8.5M to 25M after the AMR process and the adapted mesh can be seen in Figure 5.2.

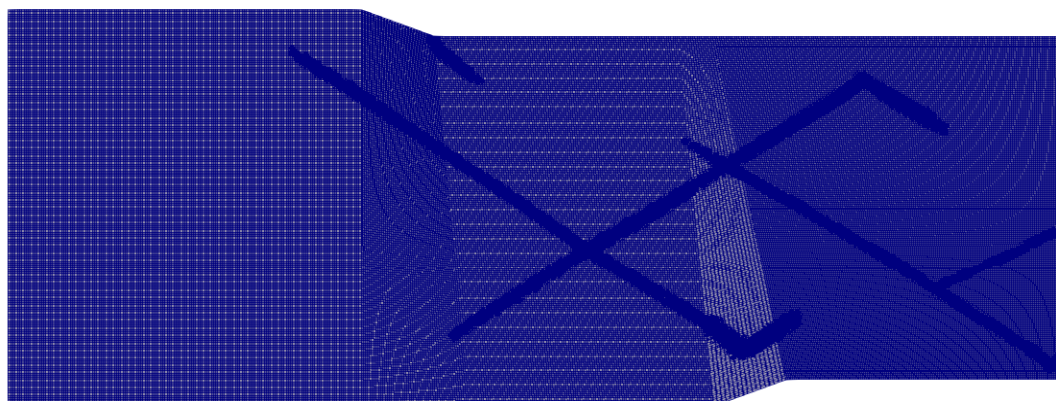


Figure 5.2. Mesh after the AMR process for Case III

In Figure 5.3 instantaneous contours of the Mach number at the mid-plane of the domain can be seen. The flow is separated by the effect of the shock waves at three different locations. The first separation zone is observed at the upper wall before the ramp. This separation zone is very similar to the one that is observed for Case II. Separated shear layer and expansion waves are observable. The separation shock of this zone impinged on the lower wall and together with the ramp caused a second separation zone. This zone is much bigger than the first one due to the presence of both the ramp and the impinging shock. The flow field around this second separation zone is very complex. There are several shock-shock interactions present which highly altered the flow field. A third separation zone is present at the upper wall downstream of the ramp. This zone is created by an impinging shock which is the separation shock for the second separation zone. This separation zone is also bigger than the first one but smaller than second one. The flow is lastly disturbed at the end of the domain at the lower wall by an impinging shock where a pressure rise is observed but flow is yet to be separated. Due to the shock-shock interactions taking place all over the flow field, shock diamonds are formed.

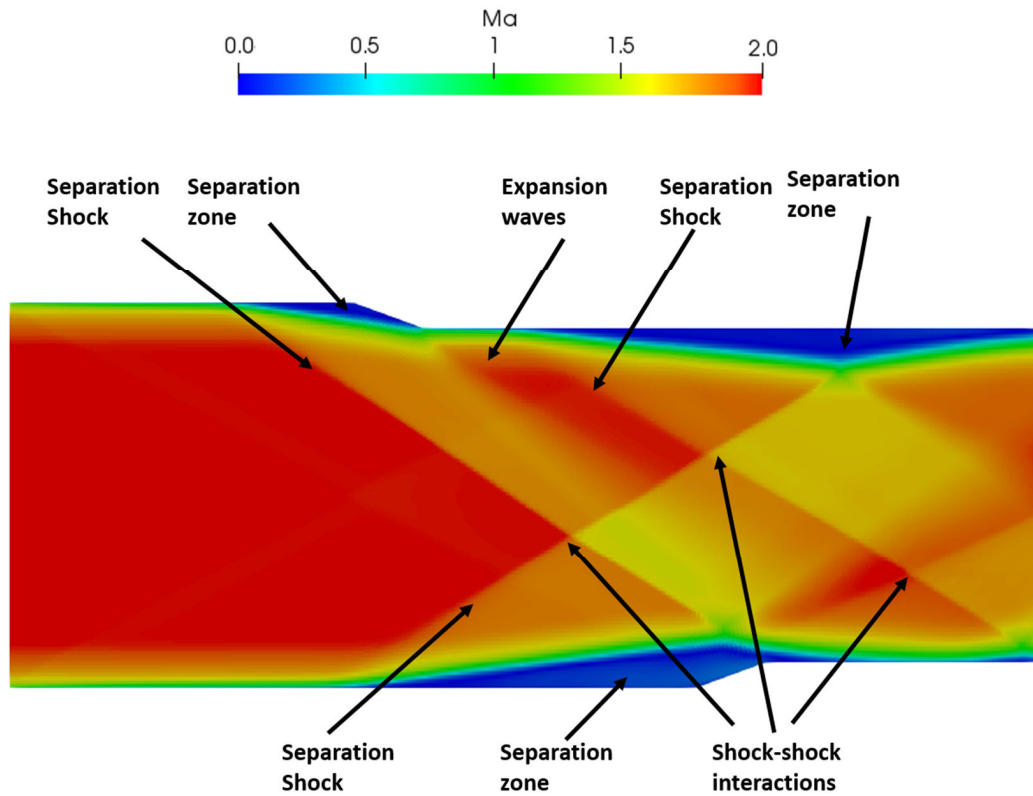


Figure 5.3. Instantaneous contours of the Mach number at the mid-plane of Case III

Instantaneous Mach number distribution at the mid-plane along the $y/\delta_0=2$ and $y/\delta_0=5.5$ lines are given in Figure 5.4. It can be seen that Mach number values are altered several times with different types of shocks such as separation shocks, impinging shocks and reattachment shocks. The values drop sharper for the separation shocks whereas the reattachment shocks are not captured very sharp.

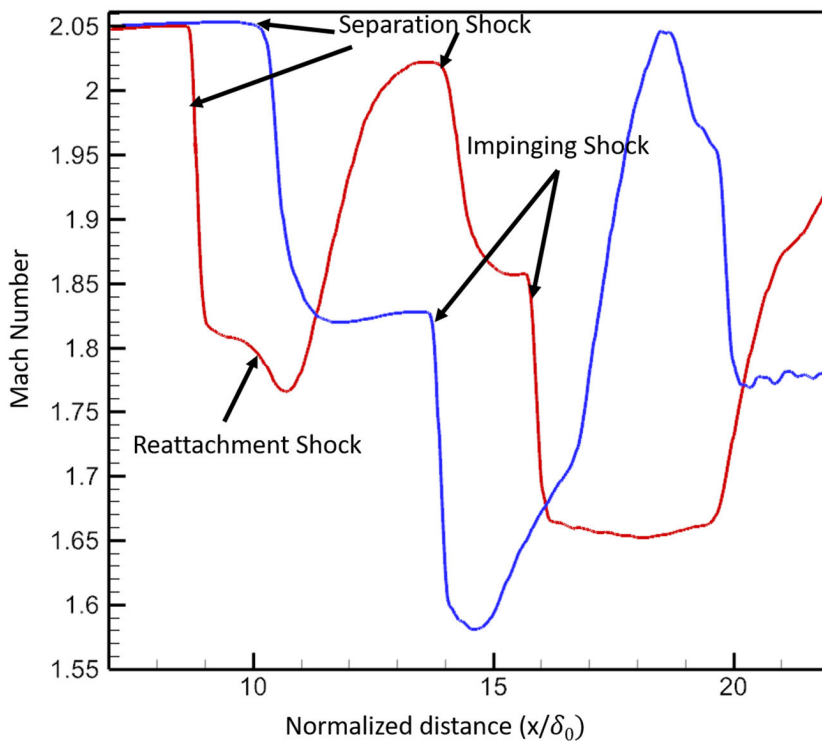
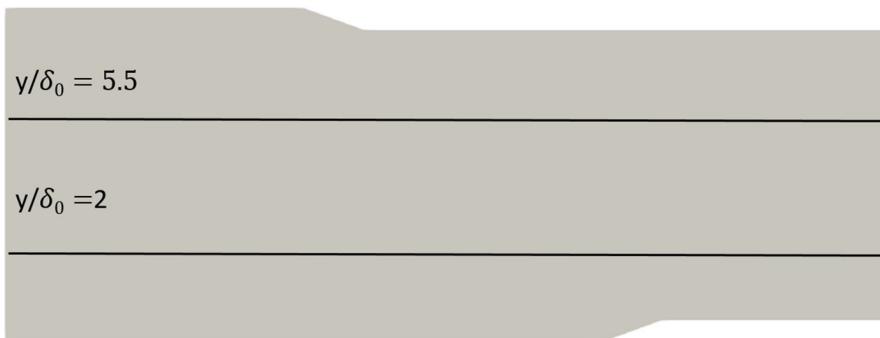


Figure 5.4. Instantaneous Mach number distribution at the mid-plane along $y/\delta_0=2$ (red), and $y/\delta_0=5.5$ (blue) lines

Mean pressure distributions on the walls averaged in both time and spanwise direction can be seen in Figure 5.5. For the upper wall, pressure rise due to the ramp and the separation shock showed the same characteristics as the Case II (see Figure 4.12). However after the ramp, flow separated again, causing a second pressure rise. For the lower wall, pressure began to rise earlier than Case II due to the effect of the

downstream ramp. After the ramp, flow reattached and a pressure rise is observed due to the impinging shock, which was originated from the second separation zone at the upper wall. As observed in the comparison of Case I results with the experiments, the current WMLES approach has difficulties in capturing the separation zone details accurately. Therefore, the results of this Case III, which is a separation dominated case, need to be evaluated with caution.

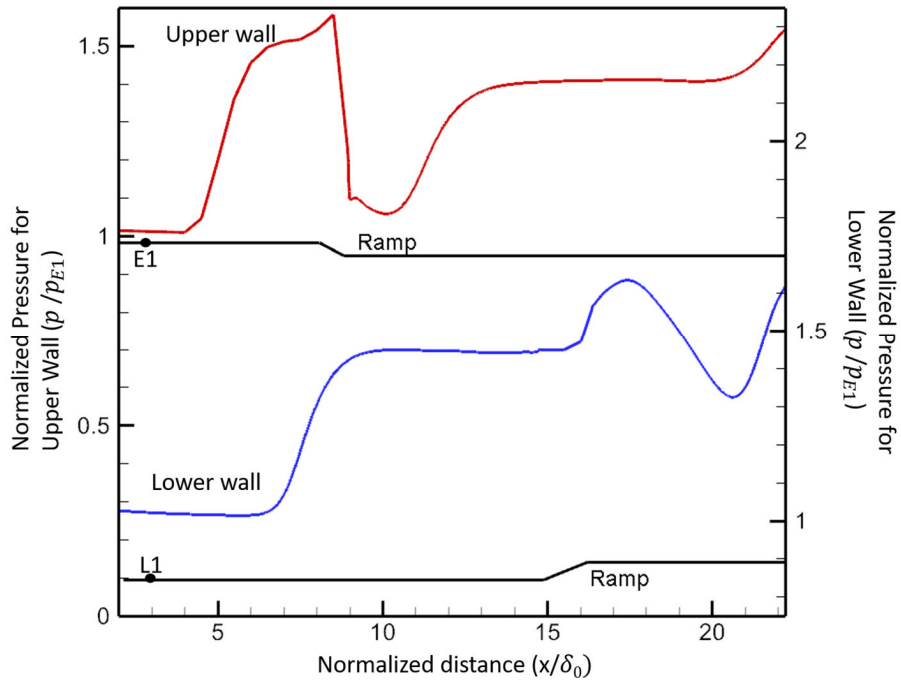


Figure 5.5. Mean pressure distributions for lower and upper walls of Case III

Skin friction coefficients can be seen in Figure 5.6. The calculated separation and reattachment points for the upper wall are $x/\delta_0=5.79$ and $x/\delta_0=8.25$ respectively for the first separation zone, which are the same as Case II. Second separation zone on the upper wall started at $x/\delta_0=13.01$ and reattached at $x/\delta_0=22.2$, which was not present for Case II.

On the lower wall, the flow first separated at $x/\delta_0=8.05$ and reattached at $x/\delta_0=16.7$. Flow reattached just after the ramp and it was disturbed again before leaving the domain by another impinging shock wave.

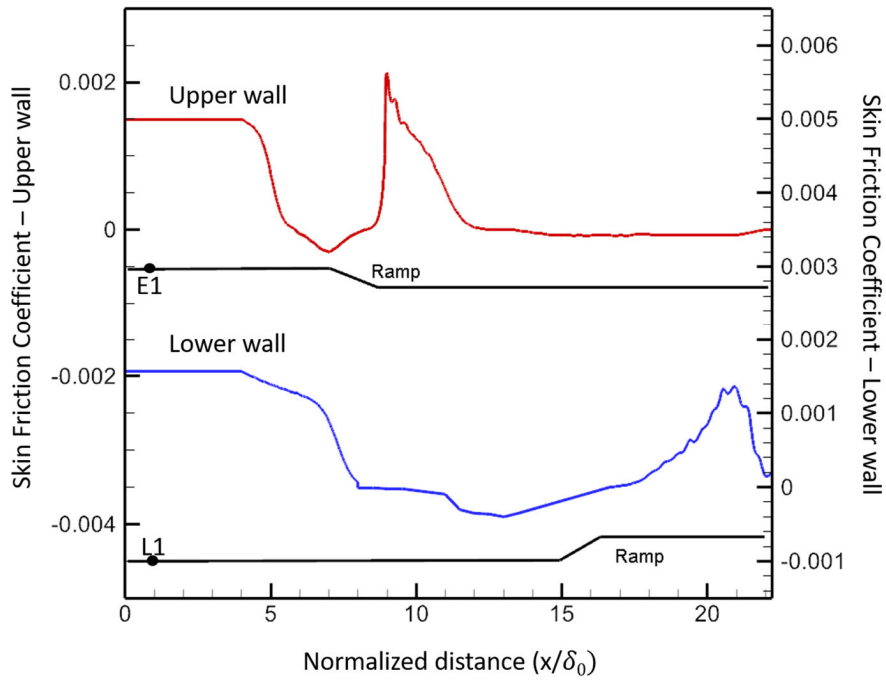


Figure 5.6. Mean skin friction coefficient distribution on the walls of Case III

Wall shear stress contours in the streamwise direction on the walls can be seen in Figure 5.7. On the upper wall the flow is similar to one that is observed for Case II until the ramp. After the ramp, due to the second separation, shear stress values varied. The flow kept its mainly two-dimensional character for the whole upper wall. Different than the upper wall, the flow on the lower wall becomes highly three-dimensional both on the ramp and downstream of the ramp. Since the lower wall has a stronger separation with a longer separation length, the disturbances have more distance to grow, giving the flow a chance to have larger variations of wall shear stress in the spanwise direction.

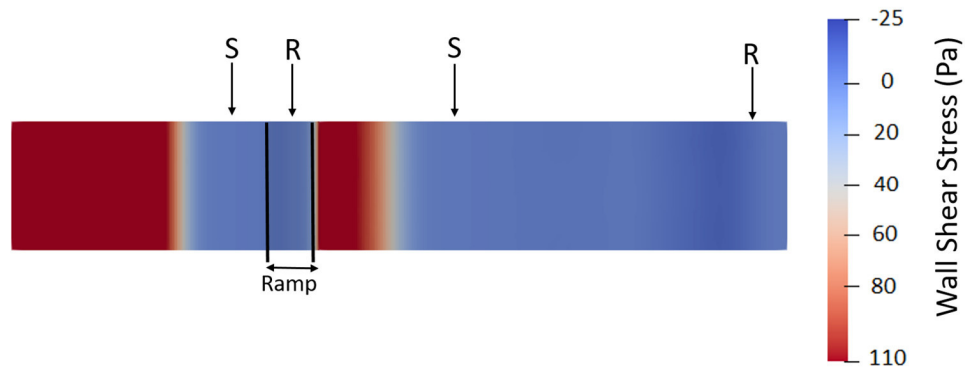


Figure 5.7. Streamwise wall shear stress contours on the upper and lower walls. (S – separation, R – reattachment, SS – Separation shock)

To examine the three-dimensionality of the flow on the lower wall, wall shear stress contours in the spanwise direction is given in Figure 5.8. It was observable that wall shear stress values are near zero before the separation shock. It can also be seen that the shear stress values have opposite signs on the two sides of the middle plane for both the ramp and downstream of the ramp. These opposite signed shear stress values indicate counter rotating vortex pairs. After the flow reattached, the rotating direction of these vortices change sign. Flow was lastly disturbed by the impinging shock just before the end of domain and it can also be seen in Figure 5.8 as the wall shear stress values started to get mixed with each other.

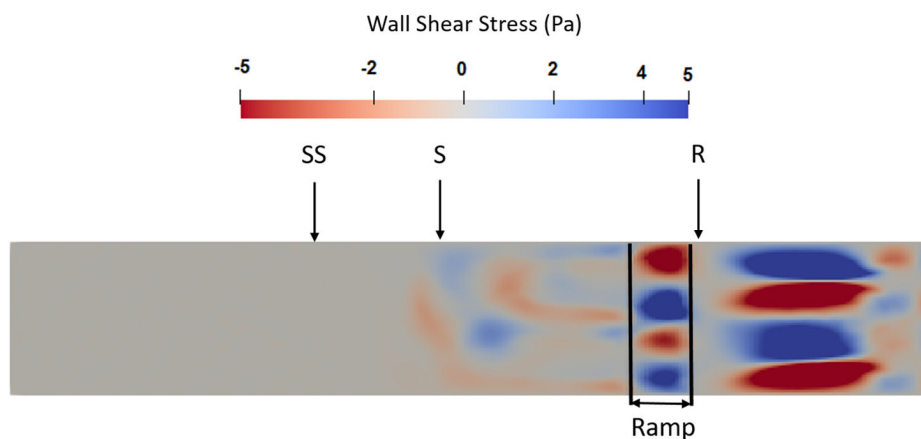


Figure 5.8. Spanwise wall shear stress contours on the lower wall of Case III. (SS – Separation Shock, S – Separation, R – Reattachment)

Streamwise vorticity contours are given in Figure 5.9 where the blue color represents negative rotation and red color represents positive rotation around the x axis. Streamwise vorticity values are amplified after the shock interaction and become even more visible after the separation. Vorticity values start to change sign in the separation zone, which indicates that three-dimensional separation topologies might be present. Two pairs of counter rotating vortices are also present, which change direction after the reattachment and downstream of the ramp. The flow becomes highly three-dimensional after the separation point and this feature is kept until the end of the domain.

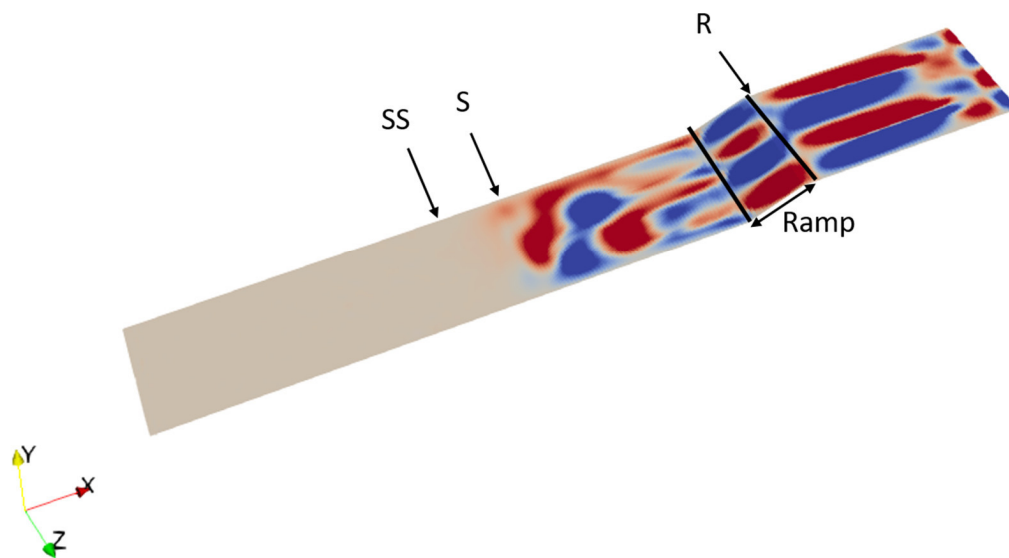


Figure 5.9. Streamwise vorticity contours on the lower wall of Case III. Blue color represents negative rotation, Red color represents positive rotation.(SS – Separation Shock, S – Separation, R – Reattachment)

Time history and Fast Fourier Transform (FFT) of wall pressures corresponding to L1 and L10 stations of the lower wall can be seen in Figure 5.10. L1 is located inside the undisturbed boundary layer close to the inlet, and L10 is located at the interaction area where the impinging shock reflects from the boundary layer. The time histories showed differences in both fluctuation amplitude and behavior. Root mean squares of the fluctuation amplitudes are around 5 Pa for L1 and, 101 Pa for L10. Fluctuations

are much more rapid at the L1 station than L10. It can be seen that the dominant frequencies are between 10^5 and 10^6 for L1, whereas they are between 10^3 and 10^4 for L10.

The dominant frequencies for station L10 are on a lower level for this case than Case II. This level difference is thought to be due to the stronger interaction of this case where both impinging shock and the ramp is present. The longer separation length might have caused the shock system to move at a slower pace.

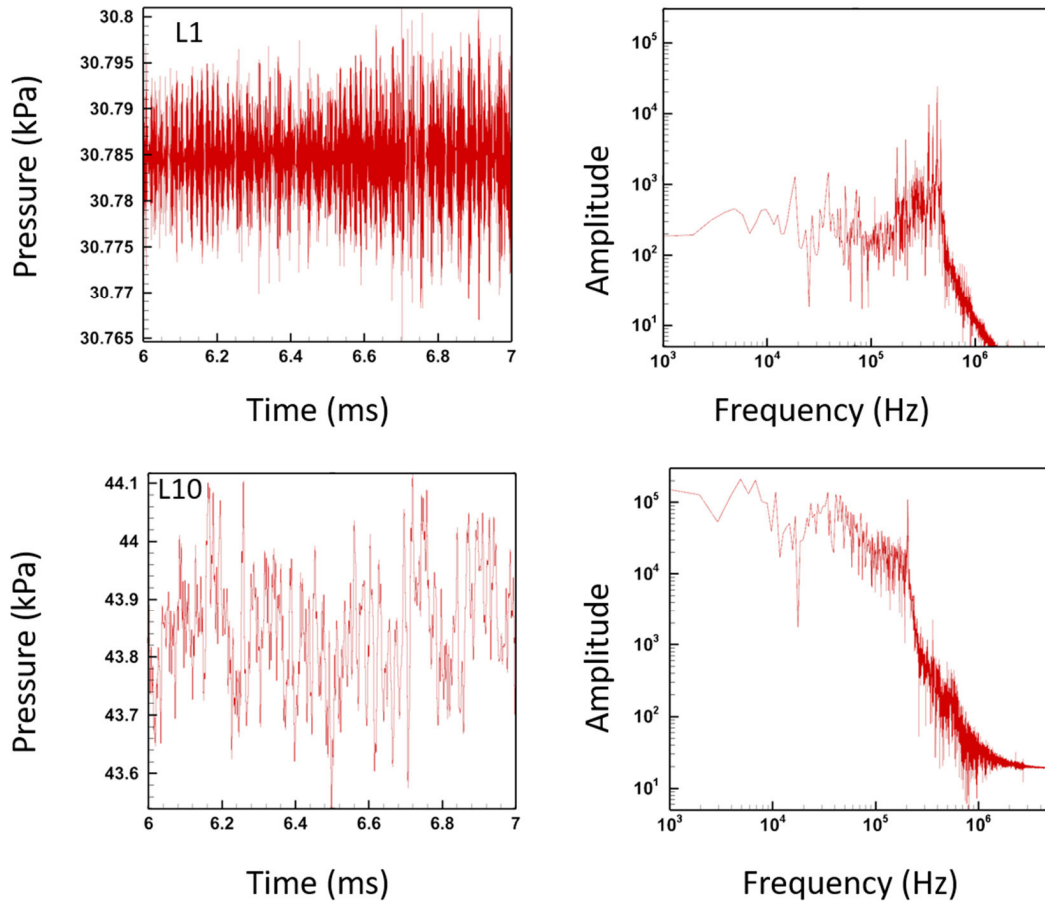


Figure 5.10. Time history of the pressure data and the corresponding FFT's for station L1 (above) and L10 (below) of the lower wall of Case III

CHAPTER 6

CONCLUSIONS

Shock wave boundary layer interactions (SWBLI) take place in several industrial flows including supersonic and hypersonic air crafts and their components and supersonic wind tunnels. SWBLI severely changes the flow behavior and affects the performance of the said components. The prediction of the effects of SWBLI thus becomes a very important issue when designing such air crafts and wind tunnels.

In the current study, following three cases that experience SWBLI phenomena are investigated by using wall modeled LES (WMLES) using wall functions with the open-source CFD software OpenFOAM

- Case I: Compression-expansion ramp
- Case II: Shock impinging on a wall
- Case III: Shock impinging on a compression-expansion ramp

In Case I, the compression ramp has the angle of 25° , inlet Mach number is 2.88 and Reynolds number based on incoming boundary layer thickness is 132000. This case is mainly used to understand the mesh requirements of the WMLES approach and to validate the current numerical approach by comparing the results with the previous experimental and numerical studies. It is shown that the results agreed in general with the experiments in terms of wall pressure distribution, separation point location and low frequency flow unsteadiness. Wall pressure distribution showed discrepancies around the separation shock but in general it was in good agreement with the experiments over the ramp. The differences between the calculated pressures and the experimental ones are on the order of 20% on the separation zone, but lower than 5% for all remaining points. Velocity profiles did not agree well in the separation zone, which is attributed to the use the wall function approach. However, it is observed that

even when the wall resolved approach is used as in the reference studies, these profiles cannot be predicted accurately when compared with the experiments. Compared with the experiments, differences in the skin friction values as high as 40% are observed. The general flow field was in good agreement with the experiment qualitatively. Main features of the flow were observed almost at the same locations with the reference studies. Separation shock, separated shear layer and expansion waves were formed where they are supposed to be whereas the stem and the angle of the reattachment shock was predicted differently than the previous results. Görtler vortices were also present over the ramp and caused the flow to be highly three-dimensional over and after the ramp. This case was mainly used to gather information about how to make OpenFOAM perform the best for the problem at hand. After rigorous trials, best settings for OpenFOAM were determined and used for the next two cases.

For the second case, a shock originating from a compression ramp and impinging on a wall on the opposite side was investigated. The compression ramp has the angle of 20° , with an inlet Mach number of 2.05 and Reynolds number based on the incoming boundary layer thickness of 188000. Other than having a shock impinging on a wall, this case differed from the first case mainly due to the ramp height being smaller than the incoming boundary layer thickness, which affects the flow character. The results were compared with the previous experimental work and observed to be in general agreement. The flow field features were observed similar to the experiment with slight differences in the shock wave angles and locations of shock-shock interactions. Separation points predicted with low errors. However, discrepancies were observed for the reattachment locations compared to the experimental ones. Unlike the first case, the flow field is observed to be mostly two-dimensional around the upper wall. The reason for this is thought to be the small ramp height resulting in a weaker interaction. Flow was more three dimensional after SWBLI on the lower wall, where the shock impinges, than the upper wall. Low frequency unsteadiness was present for the lower wall whereas it was not observed for the upper one.

For the last case, an impinging shock on a compression-expansion ramp geometry was investigated. Here we had two opposite walls both having ramps. This case was studied before neither numerically nor experimentally. The geometry was derived from Case II with an addition of a ramp at the lower wall. Both ramps have the angles of 20° and all other conditions were kept the same as Case II. Separation length of the lower wall is found to be much larger than the one for the Case II. The presence of the ramp on the lower wall caused an early separation. Moreover another separation zone occurred on the upper wall due to an impinging shock originating from the lower wall. The flow field around the upper wall mainly remained two-dimensional, but the one around the lower wall became highly three-dimensional after the SWBLI. The structures resembling Görtler vortices observed on the lower wall ramp. The low frequency component of the flow field unsteadiness was evident.

In this thesis work, it was attempted to investigate the SWBLI phenomena with WMLES using two cases already studied in the literature and a new one that is of practical significance, but have not been considered before. By using a wall model, much coarser meshes could be constructed and solved in reasonable time intervals. The results mostly agree with the available literature, with discrepancies remaining in the weak spots of WMLES and OpenFOAM. For WMLES, the separation zones could not be predicted accurately and OpenFOAM does not have all the tools to calculate flow fields that are the subject of thesis more precisely, such as high order time integration schemes and shock capturing schemes.

Wall Resolved LES Trials

It is known that, wall resolved LES performs better than the wall modelled LES, if one has the necessary computational power. Thus, after the simulations were done for WMLES, it was decided to perform wall resolved LES for the first case. However, this turned out to be a long trial and error process.

First of all, an appropriate mesh had to be constructed, which needs to be fundamentally different than the one used for WMLES. To keep the y^+ values lower than 1, a first cell height on the order of 10^{-6} m was required. The resolution of the mesh near the wall in x and z directions were similar to the WMLES case. The resulting mesh had a total of 25M cells before any adaptation for the shocks. But more importantly, this resulted in a time step of 10^{-9} s to keep the Courant number lower than the suggested value of 0.3. Under these conditions the simulations had to be run for *45 days to get a 2 ms simulation using 200 cores*, making this approach not feasible with the available resources and time. Meanwhile a series of other problems were occurring such as convergence and initialization problems. In the literature, all wall resolved LES and DNS studies used carefully crafted extra simulations to create proper inlet boundary conditions, which needed extra trials and time. Very few runs were completed without giving any errors, but unfortunately, compared with the experiments, the results were not as good as WMLES. It was clear that some other arrangements and choices for the mesh, boundary conditions, LES modeling, and initialization strategy had to be done. At this point this remain to be investigated as future work.

Struggles

The main struggle of this thesis study was trying to work with an open-source CFD code on a problem type where it was not tested enough before, using a remote and shared cluster. First of all, documentation of OpenFOAM for the use of its several features were not easy to find. To begin with, the literature suggests the use of OpenFOAM's sonicFoam solver for the supersonic flows but it turned out that this solver is too diffusive for our case. Of course understanding this required several preliminary runs. Initial information about the whole process and the right settings was little. The meaning of each error had to be learned from scratch as whether it was an error due to a wrong user made selection or due to the cluster. It was not uncommon

to have cases that were failing to run one day, but running without an issue the next day. These issues mostly related to the cluster that is used for the solutions. The same case that works in author's personal computer gives errors when tried to run at the cluster.

As another example, the author had to do a small code modification to calculate the pressure gradients during runtime to be used in AMR, with little to no information available on how to do that. It was hard to determine the source file that needs to be modified and the settings to be changed, as the available tutorial case was for a moving mesh problem. In general, OpenFOAM's documentation for both the available features and the source code to make modifications was found to be inadequate.

Working on a remote and shared cluster caused several practical difficulties, the first one being waiting in queues from time to time. Secondly, the data generated by an unsteady large eddy simulation is huge and processing it on the remote cluster was not possible due to certain technical limitations. But downloading it to a local computer also involved practical difficulties.

Recommendation for Improvement and Future Work

Recommendations for improvement and possible future work are given below:

- Due to the use of a wall function in this study, results showed discrepancies in the separation zones. Hybrid RANS-LES, DES or wall resolved LES approaches should be considered to get better results.
- Use of AMR turned out to be very effective in these flows with shock waves. However, only refinement was performed, but no coarsening. More efficient ways to use AMR could be thought by including coarsening. It was observed that AMR is usually not modifying the first two layers of cells adjacent to the walls. In other words, it is not altering the large y^+ values specially designed to perform WMLES, which is good. Given this, it may be possible to start the

simulation with a desired mesh on the walls, but coarser inside the domain and let AMR craft the inside mesh as required. This way more AMR steps could be used. Also different refinement AMR parameters and limits can be tried.

- Different wall model options are available in OpenFOAM and their performance can be tested by making comparisons with the reference results and the ones presented in the current study. Also different SGS models are available and they can be tested and compared with the one used.
- The domain of Case II was defined as the middle section of the actual experimental setup. The case might be enlarged to have double the size in the spanwise direction to match the experimental width and sidewalls might be considered as walls. By this way, the sidewall effects and corner flows can be studied and the effects of choosing sidewalls as symmetry planes can be observed.
- For this study, walls are considered to be adiabatic. For more realistic cases wall temperature might affect the flow. Thus, new runs considering the heat transfer effects at the wall might be done.
- Only the Reynolds numbers given in the experiments were studied for this thesis work. By using different Reynolds numbers, effect of Reynolds number on the flow field characteristics might be investigated.

REFERENCES

- [1] AGARD-AG-280. 1986. Turbulent Shock-wave/Boundary-Layer Interactions.
- [2] Zheltovodov, A., A.1996. Shock Waves/Turbulent Boundary-Layer Interactions - Fundamental Studies and Applications, AIAA Paper 96-1977.
- [3] Dolling, D., S. 2001. Fifty Years of Shock-Wave/Boundary-Layer Interaction Research: What Next?. AIAA JOURNAL Vol. 39, No. 8, 1517-1531.
- [4] Korkegi, R. H. 1971, Survey of Viscous Interactions Associated with High Mach Number Flight, AIAA Journal, Vol. 9, No.5, 771-784.
- [5] Clemens, N., T., Narayanaswamy, V. 2013. Low-Frequency Unsteadiness of Shock Wave/Turbulent Boundary Layer Interactions, Annual Review of Fluid Mechanics, 46, 469-492.
- [6] Gaitonde, D., V., 2014, Progress in Shock Wave/Boundary Layer Interactions, Progress in Aerospace Sciences, 72, 80-99.
- [7] J. Fang, Y. Yao, A. A. Zheltovodov, et al. 2015, Direct Numerical Simulation of Supersonic Turbulent Flows Around a Tandem Expansion-Compression Corner, Physics of Fluids, 27, 125104.
- [8] Grilli, M., Hickel, S., Adams, N., A. 2013. Large-Eddy Simulation of a Supersonic Turbulent Boundary Layer Over a Compression–Expansion Ramp, International Journal of Heat and Fluid Flow, 42, 79-93.
- [9] Campo, L., M., Eaton, J., K. 2015. Shock Boundary Layer Interactions in a Low Aspect Ratio Duct, International Journal of Heat and Fluid Flow, 51, 353-371.
- [10] Pozefsky, P., Blevins, R. D., and Laganelli, A. L. 1989. Thermo-Vibro Acoustic Loads and Fatigue of Hypersonic Flight Vehicle Structure, Air Force Wright Aeronautical Labs., TR-89-3014.
- [11] Erengil, M. E., Dolling D. S. 1991. Unsteady Wave Structure Near Separation in a Mach 5 Compression Ramp Interaction. AIAA J. 29:728–35.

- [12] Herrmann, D., et al. 2011. Experimental Study of Boundary-Layer Bleed Impact on Ramjet Inlet Performance. *Journal of Propulsion and Power*. Vol. 27, No. 6.
- [13] Ali, M., Alvi, F., Manisankar, C., Verma, S., Venkatakrishnan, L. 2011 Studies on the Control of Shock Wave-Boundary Layer Interaction Using Steady Microactuators, AIAA Paper 2011-3425.
- [14] Zheltovodov, A., A. 2006. Some Advances In Research Of Shock Wave Turbulent Boundary Layer Interactions, 44th AIAA Aerospace Sciences Meeting and Exhibit, Reno, Nevada.
- [15] Knight D., D., Degrez, G. 1998. Shock Wave Boundary Layer Interactions in High Mach Number Flows a Critical Survey of Current Numerical Prediction Capabilities. AGARD ADVISORY REPORT AGARD AR 2, 1-1
- [16] Zhiyin, Y. 2015. Large-eddy simulation: Past, Present and the Future. *Chinese Journal of Aeronautics* 2015.28(1): 11–24.
- [17] Fureby, C. 2008. Towards the Use of Large Eddy Simulation in Engineering. *Progress in Aerospace Sciences* 44, 381–396.
- [18] Piomelli, U. 2008. Wall-Layer Models for Large-Eddy Simulations. *Progress in Aerospace Sciences* 44, 437–446.
- [19] Piomelli, U., Balaras, E. 2002. Wall-Layer Models for Large-Eddy Simulations. *Annu. Rev. Fluid Mech.* 34:349–74.
- [20] Park, G.,I., Moin, P. 2016. Numerical Aspects and Implementation of a Two-Layer Zonal Wall Model for LES of Compressible Turbulent Flows on Unstructured Meshes. *Journal of Computational Physics* 305, 589–603
- [21] Frohlich, J., von Terzi, D. 2008. Hybrid LES/RANS Methods for the Simulation of Turbulent Flows. *Progress in Aerospace Sciences* 44, pp.349–377.
- [22] Breuer, M., et al. 2007. Development of Wall Models for LES of Separated Flows Using Statistical Evaluations. *Computers & Fluids* 36, pp.817–837.

- [23] Argyropoulos, C.D., Markatos, N.C. 2015. Recent Advances on the Numerical Modelling of Turbulent Flows. *Applied Mathematical Modelling* 39, 693–732.
- [24] Gadd, G., E. 1962. Interactions between Normal Shock Waves and Turbulent Boundary Layers. N.P.L. Aerodynamics Division. Reports and Memoranda No. 3262.
- [25] Seddon, J., Murphy, M., T. 1970. Boundary-Layer Interaction Effects in Intakes with Particular Reference to those Designed for Dual Subsonic and Supersonic Performance. Reports and Memoranda No. 3565.
- [26] Dolling, D., S. 1985. Unsteadiness of the Shock Wave Structure in Attached and Separated Compression Ramp Flows. *AIAA Journal* Vol. 21, No. 12.
- [27] Gramann, R., A., Dolling, D., S. 1986. Unsteady Separation in Shock Wave Turbulent Boundary Layer Interaction. *AIAA/ASME 4th Joint Fluid Mechanics, Plasma Dynamics and Lasers Conference*. AIAA 86-1033.
- [28] Alvi, F., S., Settles, G., S. 1992. Physical Model of the Swept Shock Wave/Boundary Layer Interaction Flow field. *AIAA Journal* Vol. 30, No. 9.
- [29] Wideman, J., K. et al. 1995. Skin Friction Measurements in Three Dimensional, Supersonic Shock Wave/Boundary Layer Interaction. *AIAA Journal* Vol. 33, No. 5.
- [30] Grasso, F., Marini, M. 1996. Analysis of Hypersonic Shock Wave Laminar Boundary Layer Interaction Phenomena. *Computers & Fluids*, Vol. 25, No. 6, pp. 561-581.
- [31] Panaras, A., G. 1996. Review of the Physics of Swept Shock/Boundary Layer Interactions. *Progress in Aerospace Sciences* Volume 32, Issues 2–3, 1996, Pages 173-244.
- [32] Gaitonde, D., Edwards, J., R. 1997. Structure of a Supersonic Three Dimensional Cylinder/Offset Flare Turbulent Interaction. *Journal of Spacecraft and Rockets* Vol. 34, No. 3.

- [33] Mohammed, S. 1997. Experimental Investigation of Shock Wave and Boundary Layer Interaction near Convex Corners in Hypersonic Flow. Master's Thesis. University of Toronto.
- [34] Adams, N., A. 1998. Direct Numerical Simulation of Turbulent Compression Ramp Flow, *Theoret. Comput. Fluid Dynamics*. 12: 109–129.
- [35] Schulte, D. et al. 1998. Reduction of Shock Induced Boundary Layer Separation in Hypersonic Inlets Using Bleed. *Aerospace Science and Technology*, no. 4, 231-239.
- [36] Liou, W., et al. 1998. Turbulence Model Assessment for Shock Wave/Turbulent Boundary Layer Interaction in Transonic and Supersonic Flows. *Computers & Fluids* 29, 275–299.
- [37] Coratekin, T., Schubert, A., Ballmann, J. 1999. Assessment of Eddy Viscosity Models in 2D and 3D Shock / Boundary – Layer Interactions. *Engineering Turbulence Modelling and Experiments – 4*.
- [38] Gaitonde, D. 1999. Three Dimensional Turbulent Interactions Caused by Asymmetric Crossing Shock Configurations. *AIAA Journal* Vol. 37, No. 12.
- [39] Déler, J., M., Bur, R. 2000. The Physics Of Shock Wave/Boundary Layer Interaction Control: Last Lessons Learned. *European Congress on Computational Methods in Applied Sciences and Engineering ECCOMAS*.
- [40] Rizzetta et al. 2001. Large-Eddy Simulation of Supersonic Compression-Ramp Flow by High-Order Method, *AIAA JOURNAL* Vol. 39, No. 12.
- [41] Rizzetta et al. 2002. Application of Large-Eddy Simulation to Supersonic Compression Ramps, *AIAA JOURNAL* Vol. 40, No. 8.
- [42] Thivet, F. 2002. Analysis of Observed and Computed Crossing Shock Wave/Turbulent Boundary Layer Interactions. *Aerospace Science and Technology* 6 3–17.
- [43] Knight, D., et al. 2003. Advances in CFD Prediction of Shock Wave Turbulent Boundary Layer Interactions. *Progress in Aerospace Sciences* 39 (2003) 121–184.

- [44] Arnal, D. 2004. Laminar Turbulent Transition and Shock Wave/Boundary Layer Interaction. RTO-EN-AVT-116.
- [45] Teramoto, S. 2005. Large Eddy Simulation of Shock Wave/Boundary Layer Interaction. *Trans. Japan Soc. Aero. Space Sci.* Vol. 47, No. 158, pp. 268–275.
- [46] Dupont, P., et al. 2005. Space and Time Organization of a Shock Wave/Turbulent Boundary Layer Interaction. *Aerospace Science and Technology* 9, 561–572.
- [47] Dussauge, J., P. 2005. Unsteadiness in Shock Wave Boundary Layer Interactions with Separation. *Aerospace Science and Technology* 10, 85–91.
- [48] Loginov, et al., 2006. Large-Eddy Simulation of Shock-Wave/Turbulent-Boundary-Layer Interaction, *J. Fluid Mech.*, vol. 565, pp. 135–169.
- [49] Zheltovodov, A., A. 2006. Some Advances in Research of Shock Wave Turbulent Boundary Layer Interactions. 44th AIAA Aerospace Sciences Meeting and Exhibit, Reno, Nevada.
- [50] Martin, M., P., et al. 2006. The Turbulence Structure of Shock wave and Boundary Layer Interaction in a Compression Corner. 44th AIAA Aerospace Meeting and Exhibit, Reno, Nevada.
- [51] Humble, R., A. 2006. PIV Measurements of a Shock Wave/Turbulent Boundary Layer Interaction. 13th Int. Symp. on Applications of Laser Techniques to Fluid Mechanics Lisbon, Portugal. Paper No. 1033.
- [52] Wu., M., Martin, M.,P. 2007. Direct Numerical Simulation of Supersonic Turbulent Boundary Layer over a Compression Ramp, *AIAA JOURNAL* Vol. 45, No. 4.
- [53] Sharif, M., A., R., Guo, G. 2007. Computational Analysis of Supersonic Turbulent Boundary Layers over Rough Surfaces Using the $k-w$ and the stress- w Models. *Applied Mathematical Modelling* 31, 2655–2667.
- [54] Oliver, A., B., et al. 2007. Assessment of Turbulent Shock Boundary Layer Interaction Computations Using the OVERFLOW Code. 45th AIAA Aerospace Sciences Meeting and Exhibit, Reno, Nevada.

- [55] Dann, A., G., Morgan, R., G. 2007. CFD Designed Experiments for Shock Wave/Boundary Layer Interactions in Hypersonic Ducted Flows. 16th Australasian Fluid Mechanics Conference Crown Plaza, Gold Coast, Australia.
- [56] Edwards, J. 2008. Numerical Simulations of Shock/Boundary Layer Interactions Using Time Dependent Modeling Techniques: A Survey of Recent Results. *Progress in Aerospace Sciences* 44, 447–465.
- [57] Dussauge, J., P., Piponniau, S. 2008. Shock/Boundarylayer Interactions: Possible Sources of Unsteadiness. *Journal of Fluids and Structures* 24, 1166–1175.
- [58] Détery, J. 2009. Some Physical Aspects of Shock Wave/Boundary Layer Interactions. *Shock Waves* 19, 453–468.
- [59] Subramani, B., G., Clemens, N., T., Dolling, D., S. 2009. Low Frequency Dynamics of Shock Induced Separation in a Compression Ramp Interaction. *J. Fluid Mech.*, vol. 636, pp. 397–425.
- [60] Garnier, E. 2009. Stimulated Detached Eddy Simulation of Three Dimensional Shock/Boundary Layer Interaction. *Shock Waves*, 19:479–486.
- [61] Lagha, M., et al. 2009. A Hybrid WENO Scheme for Simulation of Shock Wave Boundary Layer Interaction. 47th AIAA Aerospace Sciences Meeting Including The New Horizons Forum and Aerospace Exposition, Orlando, Florida.
- [62] Pasha, A., A. 2011. Application of Shock Unsteadiness Model to Hypersonic Shock/Turbulent Boundary Layer Interaction. Doctoral Dissertation. Department of Aerospace Engineering Indian Institute of Technology–Bombay.
- [63] Agostini, L., et al. 2012. Zones of Influence and Shock Motion in a Shock/Boundary Layer Interaction. *AIAA Journal* Vol. 50, No. 6.
- [64] Hadjadj, A. 2012. Large Eddy Simulation of Shock/Boundary Layer Interaction. *AIAA Journal* Vol. 50, No. 12.

- [65] Grilli, M., et al. 2012. Analysis of Unsteady Behavior in Shock Wave Turbulent Boundary Layer Interaction. *J. Fluid Mech.*, vol. 700, pp. 16–28.
- [66] John, B., Kulkarni, V. 2013. Numerical Assessment of Correlations for Shock Wave Boundary Layer Interaction. *Computers & Fluids*, 90 42–50.
- [67] Grilli, M., et al. 2013. Large Eddy Simulation of a Supersonic Turbulent Boundary Layer over a Compression–Expansion Ramp. *International Journal of Heat and Fluid Flow*, 42, 79-93.
- [68] Chern, S., Y. 2013. LES for Separated Supersonic Turbulent Boundary Layer and Shock Interaction. Technical Report 2013-07.
- [69] Amaha, A., H. 2014. Numerical Investigation of Shock wave Turbulent Boundary Layer Interaction over a 2D Compression Ramp. *Advances in Aerospace Science and Applications*. ISSN 2277-3223 Volume 4, Number 1, pp. 25-32.
- [70] Rad, E., G., Mousavi, S., M. 2015. Wall Modeled Large Eddy Simulation of Supersonic Flow Physics over Compression–Expansion Ramp. *Acta Astronautica*, 117, 197-208.
- [71] Fang, J., Yao, Y., Zheltovodov, A., A. 2015. Direct Numerical Simulation Of Supersonic Turbulent flows Around A Tandem Expansion-Compression Corner. *Physics of Fluids*, 27, 125104.
- [72] Hadjadj, A. et al. 2015. Numerical Study of Shock/Boundary Layer Interaction in Supersonic Overexpanded Nozzles. *Aerospace Science and Technology* 42, 158–168.
- [73] Lu, F. 2015. New Results on The Incipient Separation of Shock/Boundary Layer Interactions. *Procedia Engineering* 126, 12 – 15.
- [74] Guang, Y., et al. Large eddy Simulation of Shock Wave/Turbulent Boundary Layer Interaction with and without Spark Jet Control. *Chinese Journal of Aeronautics*, 29(3): 617–629.
- [75] Tong, et al. 2017. Numerical Studies of Shock Wave Interactions with a Supersonic Turbulent Boundary Layer in Compression Corner:Turning Angle Effects. *Computers and Fluids* 149, 56–69.

- [76] Piomelli, U., et al. 2007. Wall-Layer Models For Large-Eddy Simulations of High Reynolds Number Non-Equilibrium Flows. *Advances in Turbulence XI. Springer Proceedings Physics*, vol 117. Springer, Berlin, Heidelberg.
- [77] Patil, S., Tafti, D. 2012. Wall Modeled Large Eddy Simulations of Complex High Reynolds Number Flows with Synthetic Inlet Turbulence. *International Journal of Heat and Fluid Flow* 33, 9–21.
- [78] Park, G., Moin, P. 2016. Numerical Aspects and Implementation of a Two-Layer Zonal Wall Model for LES of Compressible Turbulent Flows on Unstructured Meshes. *Journal of Computational Physics* 305, 589–603.
- [79] Park, G.I. 2015. Wall-Modeled Large-Eddy Simulation of a Separated Flow Over the NASA Wall-Mounted Hump. *Center for Turbulence Research Annual Research Briefs*.
- [80] Breuer, M., et al. 2007. Development of Wall Models for LES of Separated Flows Using Statistical Evaluations. *Computers & Fluids* 36, 817–837.
- [81] Fukushima, Y., Kawai, S. 2017. Wall-Modeled Large-Eddy Simulation of Transonic Buffet over a Supercritical Airfoil at High Reynolds Number. *55th AIAA Aerospace Sciences Meeting*. Grapevine, Texas.
- [82] Fu, L., Karp, M., Bose, S., T. 2018. Equilibrium Wall-Modeled LES of Shock-Induced Aerodynamic Heating in Hypersonic Boundary Layers. *Center for Turbulence Research Annual Research Briefs*.
- [83] Marco, N., J. 2018. Wall-Modeled Large Eddy Simulation of a Three-Dimensional Shock-Boundary Layer Interaction. *Master's Thesis*. Department of the Air Force, Air Force Institute Of Technology, Air University.
- [84] Modesti, D., Pirozzoli, S. 2017. A Low-Dissipative Solver for Turbulent Compressible Flows on Unstructured Meshes with OpenFOAM Implementation. *Computers and Fluids*, 152, 14–23.
- [85] Shen, C., Sun, F., Xia, X. 2014. Implementation of Density-Based Solver for All Speeds in the Framework of OpenFOAM. *Computer Physics Communications*, 185, 2730-2741.

- [86] D.Cao, G. He, F. Qin, X. Wei, L. Shi, B. Liu, Z. Huang. 2017. LES Study on Flow Features of the Supersonic Mixing Layer Affected by Shock Waves. *International Communications in Heat and Mass Transfer*, 85, 114-123.
- [87] K. Makowka , N.C. Dröske, J. Wolfersdorf, T. Sattelmayer. 2017. Hybrid RANS/LES of a Supersonic Combustor. *Aerospace Science and Technology*, 69, 563-573.
- [88] Freitas, P., G., F., E. 2014. Numerical Simulation of Compressible Flow Over a Deep Cavity. (Master's Thesis). Retrieved from <https://fenix.tecnico.ulisboa.pt/downloadFile/563345090412638/Thesis.pdf>
- [89] OpenFOAM User Guide version 6. 10th July 2018.
- [90] Kurganov, A., Tadmor, E. 1999. New High-Resolution Central Schemes for Nonlinear Conservation Laws and Convection–Diffusion Equations. *Journal of Computational Physics* 160, 241–282.
- [91] Greenshields, et al. 2009. Implementation of Semi-Discrete, Non-Staggered Central Schemes in a Colocated, Polyhedral, Finite Volume Framework, for High-Speed Viscous Flows. *International Journal for Numerical Methods in Fluids*, 63:1–21.
- [92] Asproulias, I. 2014. RANS Modelling for Compressible Turbulent Flows Involving Shock Wave Boundary Layer Interactions. Doctoral Dissertation. School of Mechanical Aerospace and Civil Engineering, University of Manchester.
- [93] Liu, F. 2016. A Thorough Description of How Wall Functions are Implemented in OpenFOAM. In *Proceedings of CFD with OpenSource Software*. 2016. Edited by Nilsson. H.
- [94] Trias, F., X., et al. 2017. A New Subgrid Characteristic Length for Turbulence Simulations on Anisotropic Grids. *Phys. Fluids* 29, 115109.
- [95] Pope, S. B. 2000. *Turbulent Flows*. Cambridge University Press.

- [96] Çelik, I. B., Çehreli Z. N., and Yavuz, I. 2005. Index of Resolution Quality for Large Eddy Simulations. *Journal of Fluid Engineering*, vol. 127, pp. 949-958.